

Assessment and Monitoring of RF Safety for Ultra-High Field MRI

Matthew Charles Restivo

Assessment and Monitoring of RF Safety for Ultra-High Field MRI
PhD thesis, Utrecht University, The Netherlands
@ M.C. Restivo, 2017

ISBN:
Printed by:

No part of this thesis may be reproduced, stored or transmitted in any form or by any means, without prior permission by the author. The copyright of the articles that have been published or have been accepted for publication has been transferred to the respective journals.

Assessment and Monitoring of RF Safety for Ultra-High Field MRI

Onderzoeken en Beoordelen van RF Veiligheid voor Ultra-Hoog Veld MRI

(met een samenvatting in het Nederlands)

Proefschrift

ter verkrijging van de graad van doctor aan de Universiteit
Utrecht op gezag van de rector magnificus, prof.dr.G.J. van
der Zwaan, ingevolge het besluit van het college voor
promoties in het openbaar te verdedigen op dinsdag 24
januari 2017 des middags te 4.15 uur

door

Matthew Charles Restivo
geboren op 24 maart 1988
te Poughkeepsie, New York, USA

Promotoren: Prof. dr. P.R. Luijten

Copromotoren: Dr. J.M. Hoogduin
Dr. A.J. Raaijmakers

Contents

| | | |
|-----------|---|-----|
| Chapter 1 | Introduction | 7 |
| Chapter 2 | Local Specific Absorption Rate in Brain Tumors at 7T | 21 |
| Chapter 3 | Improving Peak Local SAR Prediction in Parallel Transmit Using In-situ S-matrix Measurements | 43 |
| Chapter 4 | A Novel Approach to Real-time Local SAR Monitoring for Parallel Transmit MRI at 7T using Directional Couplers | 61 |
| Chapter 5 | Advantages of Local Transmit for Prostate Imaging at 3T using an 8-Channel Parallel Transmit Array of Meandering Dipoles Compared to the Conventional Body Coil | 83 |
| Chapter 6 | Summary and Discussion | 103 |
| Chapter 7 | Nederlandse Samenvatting | 109 |
| Chapter 9 | List of Publications Acknowledgements/Dankwoord Biography | 113 |

Chapter 1

Introduction

Purpose

For years, researchers have been showing the potential for 7T MRI to image smaller structures and produce higher signal to noise ratio images in humans. There is potential for 7T MRI to outperform the standard clinical systems (1.5 and 3T) for diagnosing, quantifying progression/severity, or providing new knowledge about many illnesses and health conditions. However, radio frequency (RF) safety remains a major factor limiting the quality and speed of 7T MRI. One major safety concern is that the higher proton resonant frequency results in significantly increased RF power deposition¹, leading to potentially dangerous temperature increases in human tissue. RF power deposition, typically quantified by the specific absorption rate (SAR) in Watts per Kilogram, is a concern at all field strengths but becomes more limiting at 7T, necessitating longer scan times or sacrificing image quality. Thus, it becomes very important to have accurate SAR estimates in order to ensure patient/subject safety while, at the same time, not being overly restrictive. The subject of this thesis is to improve SAR assessment and monitoring for 7T MRI such that better safety decisions can be made.

RF and Parallel RF Transmit Arrays in Ultra-High Field MRI

In ultra-high field MRI (>3T), the wavelength of the RF field becomes on a similar order of magnitude to the width of the human body.² (Fig. 1) This leads to inhomogeneous excitation patterns, causing various flip angles (and thus signal intensity/contrast) over the field of view. One solution is to use a higher number of smaller transmit coils in parallel (known as parallel transmit or pTx).^{3,4} The idea is that each coil has a slightly different transmit sensitivity profile allowing for better coverage similar to MR receive arrays. Additionally, the relative phase and amplitude of the pTx array elements can be adjusted to result in a wide-range of B1+ field interference patterns. Simply adjusting relative amplitude and phase has proven to be an effective strategy to locally shim the B1+ field on certain regions (RF shimming).⁵⁻⁷ Phase-only RF shimming is done in practice by acquiring a series of images with each coil individually transmitting. The relative phase of these images is used to determine the drive phases which will create maximum constructive interference of the B1+ fields in a certain region of interest (ROI). RF shimming can also take into account the B1+ intensity profile of each element, and adjust the drive amplitudes as well to create a more homogenous field in the ROI.

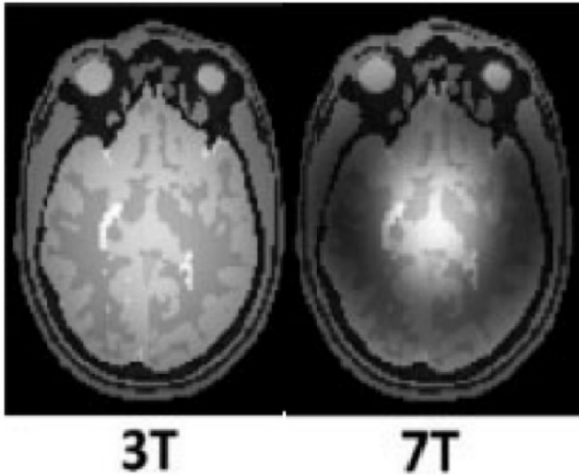


Figure 1: Simulated gradient-echo images as a function of field strength using a birdcage coil with ideal current distributions in the rungs. The signal is calculated as the product of the transmit and receive fields, assuming low-tip angle excitation. (Courtesy: Webb, Collins²)

There are a couple different pTx strategies that use more complex tailored RF waveforms for improved excitation profiles or speed. These methods allow the relative amplitude and phase settings to vary over the duration of the pulse. Fig. 2 shows the benefit of using a tailored spiral non-selective (SPINS⁸) RF pulse for creating a uniform excitation profile in the brain. Similarly, Transmit SENSE (TSENSE⁹) is a popular method for reducing the required duration of an RF pulse to achieve the same flip angle using pTx.

However, driving multiple transmit elements at the same time may come at an increased cost in terms of SAR. In addition to B1+ super-positioning, electric field super-positioning must also be considered. Furthermore, pTx arrays typically consist of smaller elements placed closer to the body, which may also cause SAR to accumulate locally near the elements. Given that at 7T, there is already an increased chance of SAR related tissue heating due to the higher resonant frequency, it is imperative that pTx SAR can be accurately assessed in order for pTx to be considered safe and useful for improving image quality.

Specific Absorption Rate

The application of current to the RF transmit coil gives rise to an electromagnetic field. The magnetic field is necessary for excitation of the spins which is the basis of the MR signal. However, the electric field will lead to the generation of

electric current in parts of the body containing conductive tissue through Ohm's Law.

$$J = \sigma E \quad [1]$$

Where J is the current density, σ is the electrical conductivity, and E is the electric field. Electrical current flowing through lossy dielectric media will always result in power deposition. Power deposited per unit volume is equal to the current density multiplied by the Hermitian conjugate of the electric field. This leads to the simplification that volumetric power density (W/m^3) is equal to the square of the electric field magnitude times the conductivity.

$$P_d = \sigma E^H E = \sigma |E|^2 \quad [2]$$

Power gets dissipated in human tissue as thermal energy. Therefore, excessive RF power deposition in an MR experiment is unsafe due to the fact that it will cause a temperature increase in the body of the subject. The exact temperature rise in a subject is very hard to predict because it depends on many factors, such as heat conduction, metabolic rate, and perfusion, as described by Penne's bioheat equation.¹⁰ However, the temperature rise contributed by the RF energy

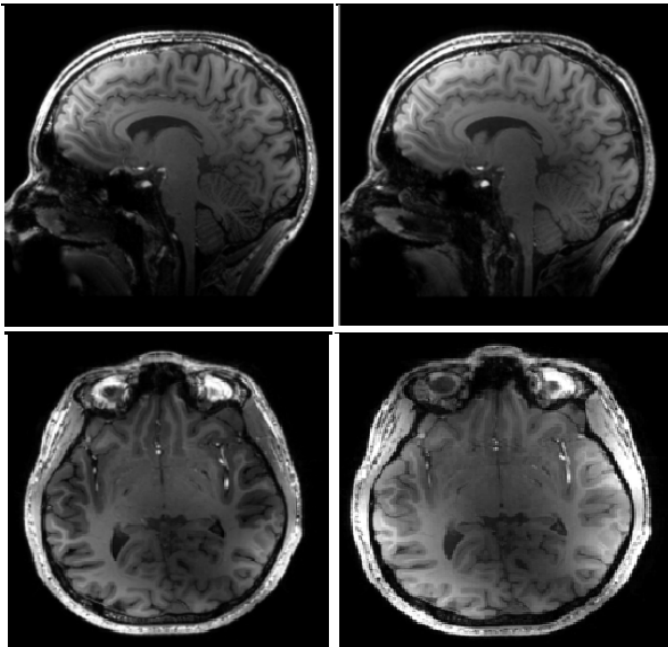


Figure 2: Comparison of MP-RAGE brain images using a quadrature sinc RF excitation (Left Column) and a SPINS excitation (Right Column). There is noticeable improvement in the contrast homogeneity in the images acquired

can be assessed by the relationship between temperature and SAR. SAR is defined as the power deposited per unit tissue mass (units of Watts per kilogram). Per Penne’s bioheat equation, SAR is directly proportional to the slope of the temperature increase over time, in the absence of other factors. Thus SAR has become the standard metric for describing RF safety in MRI and can be thought of as being related to the rate of temperature increase in human tissue.

SAR is characterized as both a global and a local phenomenon. Delivering power to a subject will cause the average temperature over the entire body to increase. However, given that SAR arises from the local electric field, some tissue volumes inside the body will have higher SAR than others, leading to non-homogenous heating. Therefore, SAR metrics for RF safety are described in terms of global (or whole-body) SAR and local SAR, which is the point-wise SAR averaged over small volumes of a certain mass. Point-wise SAR is equal to the power density divided by the mass density (ρ).

$$SAR = \frac{\sigma(r)|E(r)|^2}{\rho(r)} \quad [3]$$

Because of the diffuse character of temperature rise, this point SAR distribution is not representative for the expected temperature rise distribution. Therefore, safety guidelines are expressed as maximum values for the “local SAR”.

Local SAR can be calculated as the average SAR over any small tissue region (ex. 10g):

$$SAR_{10g} = \frac{1}{V} \int_{10g} \frac{\sigma(r)|E(r)|^2}{\rho(r)} \quad [4]$$

In the case of global SAR, the tissue containing region expands to the size of the subject, and the equation can be reduced to being equal to the total deposited power (P) over the mass of the subject (m).

$$SAR_{wb} = \frac{P}{m} \quad [5]$$

Two governing agencies, the International Electrotechnical Commission (IEC¹¹) in Europe and the Food and Drug Administration (FDA¹²) in North America, have set guidelines for global and local SAR restrictions in an MR experiment. Given that this work was done in Europe, we adhere to the IEC guidelines. The IEC guidelines define local SAR on 10g tissue containing cubes. (Fig. 3) The guidelines say that volume coils (such as body coils used in clinical 1.5T and 3T MR systems) should be restricted to the global SAR limit, while surface coils should be restricted to the local 10g SAR limit. These guidelines are valid for field strengths up to 3T. There currently exist no guidelines for the SAR limits for ultra-high field MRI, and it is up to each institution to ensure RF safety. However, Collins et. al. have shown that at field strengths greater than 3T, the local SAR limit is almost always reached before the whole body SAR limit for a birdcage head coil.¹³ This can be explained by the shortened RF wavelength at high field which results in more severe electric field inhomogeneity. At 7T, the peak local 10g SAR often can exceed the average SAR by an order of magnitude. Thus, the general agreement among 7T sites is that the SAR restrictions should be determined by the local SAR for any RF coil type.

Solutions for Estimating SAR

Global SAR resulting from a RF pulse is relatively straightforward to determine. Typically, the relationship between delivered power and achieved flip angle is known (provided by the coil manufacturer) for a single channel quadrature volume coil. The global SAR is computed by multiplying the requested B1+ by a scale factor to determine the delivered power and then divided by the total patient mass. A more accurate measurement of global SAR can be achieved using directional couplers – a hardware component that can be installed in the transmission lines between the RF amplifiers and the RF coil to measure forward

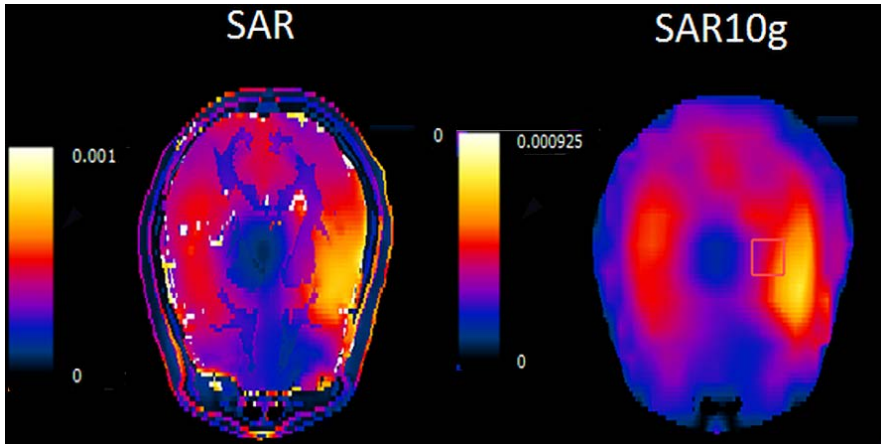


Figure 3: Example of local SAR and 10g averaged SAR shown for a single axial slice through the head from a quadrature birdcage head coil at 7T delivering 1 W power.

and reflected power levels.¹⁴ Directional couplers provide an easy global SAR monitoring solution for parallel transmit where the coil can be driven in various drive configurations and thus it would be difficult to relate B_1+ to delivered power.¹⁵

Local SAR, in comparison to global SAR, is much more difficult to determine. Local SAR depends heavily on the electric field distribution, which unlike the magnetic field distribution, is not possible to probe using only the MR scanner. There have been some investigations into trying to determine the electric field distribution from the B_1+ field distribution for determining local SAR in-vivo;¹⁶ however, this method is not very robust mostly due to the fact that anatomical variations affect the B_1+ and the electric field pattern differently, as shown by Alon et al.¹⁷ In addition, any imaging related methods are further limited by the fact that the local SAR hotspot may likely occur outside the imaging field of view.

The most common way to perform local SAR analysis is to simulate the MRI system using a computer model and compute the RF field distributions by numerically solving Maxwell's equation. Modern simulation packages (eg. Sim4Life (Zurich, ZMT AG) and CST Microwave Studio (Farmingham, MA, CST AG)) use the Finite-Difference-Time-Domain (FDTD) method of simulating RF fields. FDTD splits up the simulation domain into small cubes (called cells). The FDTD software alternates between numerically computing the electric field on the edges of the cubes and the magnetic field at the center of the cubes over sufficiently small time increments in response to an excitation source located somewhere in the domain, until the simulation converges to a steady-state (i.e. the field values are unchanging with increasing simulation time).

Very accurate body models are required to determine local SAR given that the electric field is heavily influenced by dielectric tissue properties and the geometries of anatomical features. There are currently a wide range of computational body models available for the purpose of local SAR analysis. For example, the virtual population¹⁸, provided by the IT'IS foundation, includes highly accurate models for men, women, and children of various ages and body composition. Ideally, the body model used for numerical local SAR analysis should be identical to the real subject used in the MR experiment. The current most common practice is to only simulate one of these body models and then include a very conservative safety tolerance factor (~100%) to account for subject variability. In the future, one can imagine that simulations will be performed using a variety of body models, and then the MR user can select the model which most accurately matches the patient.¹⁹ Another idea is that a quick reference scan can provide a body model of the subject in the scanner and the numerical simulations can be computed on an accurate subject-subject model immediately prior to scanning.²⁰ However, this technique would require significantly faster simulation times than are currently achievable.

Simulations for Parallel Transmit RF Arrays

Parallel transmit presents a challenge for simulating RF arrays. Assuming each channel is controlled by a different feeding source (amplifier) the various channels can be driven with different relative amplitude and phase to produce an infinite range of field patterns. This problem can be solved in the simulation environment by considering that the total EM field pattern is the linear sum of the fields produced by the individual elements. Thus an infinite range of field patterns can be predicted from simulations of individual transmit channels.

In pTx, the electric field term in the SAR equation (Eq. 3) becomes the vector product of the excitation vector ($\mathbf{I}(t)$ in Eq. 6) and a vector of electric field contribution from each array element. Since conductivity and density distributions are always the same, the quadratic excitation vector multiplication can be pulled away from the electric field vector and done as the last step. This gives rise to the Q-matrix formulism for pTx SAR computation as shown below.²¹

$$\begin{aligned} SAR(r, t) &= \frac{\sigma(r)|\mathbf{E}(r)\mathbf{I}(t)|^2}{\rho(r)} = \mathbf{I}(t)^* \frac{\sigma(r)\mathbf{E}(r)^*\mathbf{E}(r)}{\rho(r)} \mathbf{I}(t) \\ &= \mathbf{I}(t)^* \mathbf{Q}(r) \mathbf{I}(t) \quad [6] \end{aligned}$$

What is defined here as the Q-matrix ($Q(r)$) does not depend on the excitation and can be computed from the simulation results. This allows the pTx SAR distribution to be computed quickly for any excitation vector $I(t)$. The Q-matrix formalism can also be extended exactly the same way to the mass-averaged SAR (Eq. 4) resulting in a set of 10g mass averaged Q-matrices.

There are some additional benefits to the Q-matrix formalism in terms of SAR analysis. For example, the drive settings resulting in the worst case SAR for every voxel in the simulation domain is equal to the maximum eigenvector of each Q-matrix.²² The largest eigenvalue is the absolute worst case peak local SAR (usually in terms of delivered power) which is typically used as a conservative approximation of the peak local SAR on which safety decisions are made.²³

Peak local SAR determination is computationally intensive for very large simulation sizes because it involves iterating over the entire set of Q-matrices. By doing some mathematical analysis, the domain can be drastically reduced to only the points which are capable of becoming the peak local SAR value for every possible excitation vector. In order to ensure that the peak local SAR is never underestimated, a small tolerance is added to the largest valued Q-matrices, creating a set of virtual observation points (VOPs).²⁴ The number of VOPs is inversely related to the amount of over-estimation in peak local SAR that is allowable. However, this technique typically reduces the simulation domain from millions of Q-matrices to a set of tens or hundreds.

Using RF Simulations for Practical Local SAR Determination

In practice, it is difficult to use the Q-matrix approach to accurate local SAR prediction because the exact amplitude and relative phase of the signals at the input of the RF array are generally unknown. The drive amplitudes and phases are set on the scanner, however the signals feeding the array can be very different due to attenuation over the transmission line, reflections from non-ideal impedance matching, and signal coupling with the other active channels.

This issue has been addressed in the past by including additional hardware in the RF transmit path (see fig. 4 for an example) to attempt to measure the relative signal levels on the individual channels. Pick up probes²⁵ and directional couplers are two hardware solutions for measuring the signal levels feeding each transmit channel. Both methods have advantages and disadvantages which are discussed in detail in later chapters.

Outline of Thesis

In chapter 1, we investigate the effects of unexpected subject specific anatomical variations on local SAR calculation. Most SAR analysis is done using normal, healthy body models. We looked specifically into the effect of brain tumors on local SAR predictions using the standard birdcage head coil at 7T. This study allows for a better understanding of the factors which affect local SAR. It also answers the question of whether or not certain pathologies should be scanned with extra power restrictions.

Chapter 2 & 3 both address the issue of local SAR determination for pTx experiments. The RF field distribution resulting from a pTx array can be difficult to predict. The distribution depends on the exact phase and amplitude of the signal driving each individual transmit element, which is affected heavily by the inter-element coupling. In Chapter 2, we attempt to improve local SAR predictions by incorporating realistically measured coupling levels into the simulation results. In Chapter 3, we offer an alternative solution to the same problem by using directional coupler measurements to predict the precise current amplitude and relative phase present on the transmit elements during the RF pulse.

In Chapter 4, we use the aforementioned local SAR assessment strategies and apply them to 3T pTx with a local transmit array. Typically, 3T MRI is limited by the global SAR. However, when local transmit arrays are used, the peak local SAR becomes the limiting factor. We developed an eight channel dipole array for 3T prostate imaging based on similar designs for 7T MRI. We then compare it to the standard 3T body coil through both simulation and in-vivo imaging experiments.

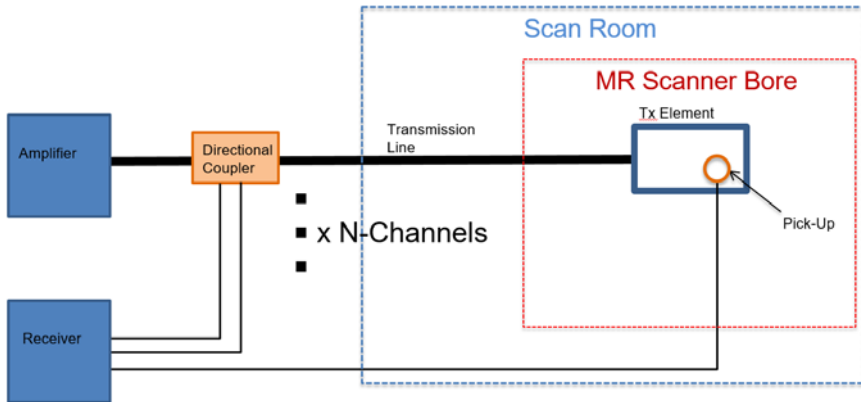


Figure 4: An illustration of the transmit path for a parallel transmit setup using directional coupler and pick-up probe monitoring. The directional couplers are installed in the transmission line path and are outside of the scan room. The pick-up probes must be right next to the transmit coil elements inside of the scanner bore. There are separate amplifiers, transmit paths, and transmit elements for every channel in the pTx setup. However, all the directional coupler and pick-up probe signals can be fed into one receiver.

References

1. Bottomley PA, Andrew ER. RF magnetic field penetration, phase shift and power dissipation in biological tissue: implications for NMR imaging. *Physics in medicine and biology*. 1978;23:630–643.
2. Webb AG, Collins CM. Parallel transmit and receive technology in high-field magnetic resonance neuroimaging. *International Journal of Imaging Systems and Technology*. 2010;20(1):2–13.
3. Padormo F, Beqiri A, Hajnal J V, Malik SJ. Parallel transmission for ultrahigh-field imaging. *NMR in biomedicine*. 2015 May 19.
4. Vernickel P, Röschmann P, Findekle C, Lüdeke K-M, Leussler C, Overweg J, Katscher U, Grässlin I, Schünemann K. Eight-channel transmit/receive body MRI coil at 3T. *Magnetic Resonance in Medicine*. 2007;58(2):381–389.
5. Metzger GJ, Snyder C, Akgun C, Vaughan T, Ugurbil K, Van de Moortele P-F. Local B1+ shimming for prostate imaging with transceiver arrays at 7T based on subject-dependent transmit phase measurements. *Magnetic resonance in medicine*. 2008;59(2):396–409.
6. Van De Moortele PF, Akgun C, Adriany G, Moeller S, Ritter J, Collins CM, Smith MB, Vaughan JT, Ugurbil K. B1 destructive interferences and spatial phase patterns at 7 T with a head transceiver array coil. *Magnetic Resonance in Medicine*. 2005;54(6):1503–1518.
7. Mueller A, Kouwenhoven M, Naehle CP, Gieseke J, Strach K, Willinek WA, Schild HH, Thomas D. Dual-source radiofrequency transmission with patient-adaptive local radiofrequency shimming for 3.0-T cardiac MR imaging: initial experience. *Radiology*. 2012;263(1):77–85.
8. Malik SJ, Keihaninejad S, Hammers A, Hajnal J V. Tailored excitation in 3D with spiral nonselective (SPINS) RF pulses. *Magnetic resonance in medicine*. 2012;67(5):1303–15.
9. Katscher U, Börnert P, Leussler C, van den Brink JS. Transmit SENSE. *Magnetic resonance in medicine*. 2004;49(1):144–50.
10. Pennes HH. Analysis of Tissue and Arterial Blood Temperatures in the Resting Human Forearm. *Journal of Applied Physiology*. 1948;1(2).
11. International T, Commission E, Iec T. IEC 60601-2-33 Safety Standard for MR Systems : Third Edition Hans Engels Philips Medical Systems , The Netherlands.
12. Center for Devices and Radiologic Health. Guidance for the submission of premarket notifications for magnetic resonance diagnostic devices. Rockville: Food and Drug Administration; 1988
13. Collins CM, Liu W, Wang J, Gruetter R, Vaughan JT, Ugurbil K, Smith MB. Temperature and SAR calculations for a human head within volume and surface coils at 64 and 300 MHz. *Journal of Magnetic Resonance Imaging*. 2004;19(5):650–656.
14. Padormo F, Beqiri A, Malik SJ, Hajnal J V. RF system calibration for global Q matrix determination. *Magnetic Resonance Imaging*. 2016;34(5):690–693.
15. Zhu Y, Alon L, Deniz CM, Brown R, Sodickson DK. System and SAR characterization in parallel RF transmission. *Magnetic resonance in medicine : official journal of the Society*

- of Magnetic Resonance in Medicine / Society of Magnetic Resonance in Medicine. 2012;67(5):1367–78.
16. Katscher U, Voigt T, Findekle C, Vernickel P, Nehrke K, Dössel O. Determination of electric conductivity and local SAR via B1 mapping. *IEEE transactions on medical imaging*. 2009;28(9):1365–1374.
 17. Alon L, Deniz CM, Carluccio G, Brown R, Sodickson DK, Collins CM. Effects of Anatomical Differences on Electromagnetic Fields, SAR, and Temperature Change. *Concepts in magnetic resonance. Part B, Magnetic resonance engineering*. 2016;46(1):8–18.
 18. Christ A, Kainz W, Hahn EG, Honegger K, Zefferer M, Neufeld E, Rascher W, Janka R, Bautz W, Chen J, et al. The Virtual Family--development of surface-based anatomical models of two adults and two children for dosimetric simulations. *Physics in medicine and biology*. 2010;55(2):N23-38.
 19. Meliado, Ettore Flavio, Raaijmakers Alexander, Restivo M, Mateo M, Luijten P, van den Berg C. Database Construction for Local SAR Prediction: Preliminary Assessment of the Intra and Inter Subject Variability in Pelvic Region. In: *Proc. Intl. Soc. Mag. Reson. Med*. 24. 2016. p. 3660.
 20. Homann H, Börnert P, Eggers H, Nehrke K, Dössel O, Graesslin I. Toward individualized SAR models and in vivo validation. *Magnetic resonance in medicine*. 2011 [accessed 2015 Aug 4];66(6):1767–76.
 21. Graesslin I, Homann H, Biederer S, Börnert P, Nehrke K, Vernickel P, Mens G, Harvey P, Katscher U. A specific absorption rate prediction concept for parallel transmission MR. *Magnetic resonance in medicine*. 2012;68(5):1664–74.
 22. Sbrizzi A, Hoogduin H, Lagendijk JJ, Luijten P, Sleijpen GLG, van den Berg CAT. Time efficient design of multi dimensional RF pulses: application of a multi shift CGLS algorithm. *Magnetic resonance in medicine*. 2011;66(3):879–85.
 23. Kraff O, Bitz AK, Kruszona S, Orzada S, Schaefer LC, Theysohn JM, Maderwald S, Ladd ME, Quick HH. An eight-channel phased array RF coil for spine MR imaging at 7 T. *Investigative radiology*. 2009;44(11):734–40.
 24. Eichfelder G, Gebhardt M. Local specific absorption rate control for parallel transmission by virtual observation points. *Magnetic Resonance in Medicine*. 2011;66(5):1468–1476.
 25. Graesslin I, Vernickel P, Börnert P, Nehrke K, Mens G, Harvey P, Katscher U. Comprehensive RF safety concept for parallel transmission MR. *Magnetic resonance in medicine*. 2015;74(2):589–98.
 26. Hoogduin JM, Mooiweer R, Mens G, Hajnal J V., Malik SJ. Initial Experience with SPIral Non Selective (SPINS) RF Pulses for Homogenous Excitation at 7T. 2014;1315(2012):7190.

Chapter 2

Local Specific Absorption Rate in Brain Tumors at 7T

Matthew C. Restivo, Cornelis A.T. van den Berg, Astrid L.H.M.W van Lier, Daniël L. Polders, Alexander J. E. Raaijmakers, Peter R. Luijten, and Hans Hoogduin

Abstract

Purpose: MR safety at 7T relies on accurate numerical simulations of transmit electromagnetic fields in order to fully assess local specific absorption rate (SAR) safety. Numerical simulations for SAR safety are currently performed using models of healthy patients. These simulations might not be useful for estimating SAR in patients who have large lesions with potentially abnormal dielectric properties, e.g. brain tumors.

Methods: In this study, brain tumor patient models are constructed based on scans of four patients with high grade brain tumors. Dielectric properties for the modeled tumors are assigned based on electrical properties tomography data for the same patients. Simulations were performed to determine SAR.

Results: Local SAR increases in the tumors by as much as 30%. However, the location of the maximum 10-gram averaged SAR typically occurs outside of the tumor, and thus does not increase. In the worst case, if the tumor model is moved to the location of maximum electric field intensity, then we do observe an increase in the estimated peak 10-gram SAR directly related to the tumor.

Conclusion: Peak local SAR estimation made on the results of a healthy patient model simulation may under-estimate the true peak local SAR in a brain tumor patient.

Introduction

Magnetic resonance (MR) at 7T magnetic field strength is desirable for a variety of imaging and spectroscopy applications typically due to the increase in signal-to-noise ratio (SNR)¹. However, ultra-high field strength MR also comes with many challenges. One specific challenge is ensuring subject safety by limiting tissue heating caused by the radio frequency (RF) excitation². While tissue heating is a potential concern at all field strengths, the danger becomes exacerbated for ultra-high field MR. Specific absorption rate (SAR), which is a measure of the energy deposited by the RF fields in tissue mass over time, is known to increase approximately quadratically with field strength³.

SAR restrictions for the safe scanning of human subjects are set by the FDA and IEC for both global average and peak spatial local SAR^{4,5}. It is necessary to estimate the SAR level prior to scanning to ensure these restrictions are met. Currently, safety decisions rely on numerical simulations for SAR estimation since it is difficult to measure SAR in-vivo^{6,7}. For global SAR, there are techniques to restrict unreasonably high exposure with the use of power monitoring units. Global SAR can also be reasonably estimated during an excitation by computing coil loading factors⁸. There are even emerging techniques to measure global SAR in parallel transmit systems with the use of power balance monitoring hardware⁹. Still, there exists no reliable technique for monitoring or measuring local SAR in-vivo during a scan. Previous research has shown that peak local SAR limits are reached before global SAR limits for most common transmit coils at normal excitation frequencies, highlighting that global SAR monitoring alone is not sufficient for patient safety assessment¹⁰.

Local SAR patterns depend heavily on the electromagnetic interaction of the RF fields with dielectrically heterogeneous human body¹¹. For accuracy, simulations must contain realistic representations of both the RF transmit system and the complex patient anatomy¹². There has been significant progress made over the last few years to define a larger population of highly detailed human models^{13,14}. This has helped to assess the effect of inter-subject variability on local SAR values^{15,16}. However, peak spatial local SAR decisions on the scanner are based on the simulation of only one generic patient most of the time. Inter-subject variability and position dependency on peak local SAR values are accounted for by multiplying the result with a conservative safety tolerance factor.

Up until now, all available patient models have been made to represent the normal, healthy human subjects. This is of concern because in real scan

environments patients have pathological conditions that can significantly alter their anatomy. Large volume pathologies with altered dielectric properties compared to normal tissue will likely affect local SAR behavior. The effect of such pathologies on local SAR is generally unknown, and is the subject of this work. Tumors are a prime example because they are known to exhibit elevated electrical conductivity, which can lead to an increase in local SAR¹⁷. This study is specifically concerned with the risk RF heating of brain tumors, since 7T imaging at this time is mostly focused on the brain. While the heating of cancerous tissue might not be seen as a risk, it is better at this time to adhere to IEC and FDA guidelines regarding SAR for all tissue types. Significant heating near the boundaries of tumors would also pose a risk to nearby healthy tissue. In this study, realistic tumor patient models are generated using anatomical data combined with in-vivo electrical conductivity scans acquired from real patients with high grade brain tumors. Electromagnetic simulations are performed using these models to examine the effect of a brain tumor on the 10g averaged local SAR (SAR_{10g}) distribution as well as the determination of the peak spatial 10g averaged SAR (SAR_{P,S}).

Theory

Tumors could pose a significant SAR risk based on literature which suggests that high grade brain tumors have higher electrical conductivity than normal brain tissue. Several studies in particular have used electrical properties tomography (EPT) to non-invasively measure conductivity in brain tumors in-vivo^{18,19}. EPT is a technique that uses MR imaging to compute dielectric properties of human tissue by analyzing the complex B1 fields²⁰.

Conductivity is directly related to the calculation of local SAR based on the following equation:

$$SAR(r) = \frac{\sigma(r)|E(r)|^2}{2\rho(r)} \quad [1]$$

Eq. 1 shows the calculation of local SAR where r represents a location within the subject with conductivity σ , density ρ , and total electric field amplitude $|E|$.

The guidelines for SAR_{P,S} are based on RF induced heating. Thermal effects, like heat conduction, are dependent on density and volume. Therefore, the safety limits for peak local SAR are placed on average SAR over an n-gram mass tissue region. We adhere to the IEC definitions which define SAR_{P,S} as the local SAR averaged over 10-gram cubes (SAR_{10g}). SAR_{10g} is calculated from a numerical

simulation by averaging the SAR per voxel over a cubic region containing 10g of total tissue mass centered at location r , as described by Caputa, et al²¹.

Methods

Generating the Tumor Patient Models

As part of a previous brain tumor study²², seven patients with brain tumors were scanned at 3T, generating contrast enhanced T1-weighted anatomical images. This data set was registered to 7T EPT scans acquired just previously to the 3T scans of the same seven patients to non-invasively measure tumor conductivity¹⁷. For the EPT measurements, the conductivity is determined from the complex B1+ field. The B1+ magnitude was measured based on the Bloch-Siegert shift method²³. The transceive phase was measured using an interleaved measurement with two TEs (TE1 = 1.94 ms and TE2 = 2.94 ms). The phase measurement was repeated with opposed gradients to correct for eddy currents. To obtain the B1+ phase, it was assumed that the transceive phase is twice the B1+ phase²⁴. Both 7T EPT and 3T anatomical data sets were acquired on the same day to ensure proper registration of conductivity value to tissue type.

The largest increase in tissue conductivity compared to normal brain tissue was observed in high grade tumors (grade IV) which were present in four of the seven patients. High grade tumors appear to have two distinct regions in both the EPT and contrast enhanced T1-weighted images: 1) a region that is enhanced by contrast with slightly higher conductivity values versus normal brain tissue on EPT scans and 2) a region that is not enhanced by contrast with significantly higher conductivity values on EPT versus normal brain tissue¹⁷. It is believed that the non-enhancing region is a necrotic, fluid filled region which is non-perfused and thus not enhanced by the contrast agent. In this study, we investigate the impact of increased tumor conductivity on local SAR in the tumor. For this purpose we construct dielectric models of the four brains with high grade tumors. Tumors are modeled using a two-compartment model with each compartment having different electrical properties in order to reflect the noticeable conductivity difference between contrast enhanced and non-contrast enhanced tumor tissue.

The 3T anatomical images were segmented into different human tissue types used to generate 3D brain models for each patient. To mitigate the challenges associated with segmentation, it was decided to limit the segmentation to five tissue types to have a reasonable compromise between completeness and model

integrity. Healthy brain tissue was segmented into three regions of distinct conductivities: grey matter, white matter, and cerebrospinal fluid (CSF). Additionally, the tumor was segmented into two regions: contrast enhancing and non-enhancing tumor. Slicer3D segmentation software was used for segmentation of healthy brain tissue using an atlas based automatic segmentation method²⁵. The tumors were manually segmented separately using iSeg segmentation software.

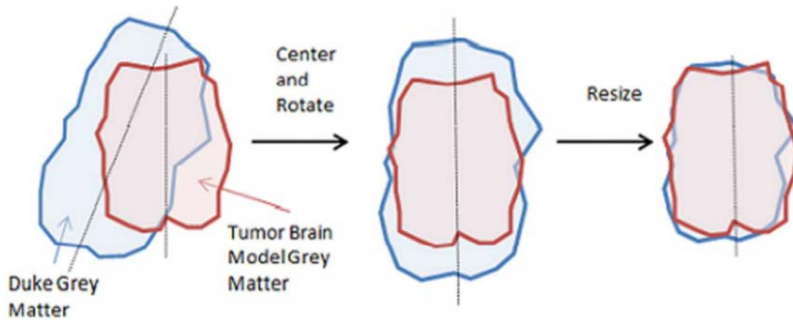


Figure 1: 2D (axial) Illustration of the registration process based on grey matter boundaries and center lines. Registration is performed so that the body model is proportional in size, position, and orientation to the brain model. Black dotted lines represent the center lines of the grey matter.

The brain models were imported into SEMCAD X (Speag AG, Zurich, Switzerland), which was used for volume rendering of the model and electromagnetic solver (FDTD) in this study. The brain models were then merged with the body of the “Duke” model, a standard male human model from the Virtual Family¹³. This was necessary because the models constructed from the tumor patient scans only consisted of the brain. A more complete model of the human body is necessary for an accurate simulation. The Duke model was modified appropriately so that Duke’s skull fit realistically around the tumor patient’s brain. This was done through a strict, repeatable process.

The registration process was performed using the boundaries of the grey matter. The grey matter defines the perimeter of the brain’s solid tissues. The manipulation of the entire Duke model was performed in such a way that the overlaid grey matter structures produce a decent fit between the skull of Duke and the tumor patient’s brain (Fig. 1). The patient’s brain was centered at the origin of the coordinate system defined by the modeler. The patient’s brain was also rotated so that the center line was on the y-axis. For registration, the Duke model was similarly centered and rotated. The entire Duke model was then

scaled simultaneously in such a way that the x, y, and z boundaries of Duke's grey matter were the same as the patient's. The Duke model is scaled instead of the patient's brain so that the accurate geometry of the tumor is maintained through this process. This method does not achieve complete overlap, which is very difficult due to variance in the shape of a brain from one subject to the next. However, it is a simple process that places the tumor in the correct location within the skull based on visual inspection and comparison with the original anatomical images.

During voxelization, in areas where Duke's brain and the patient's brain overlap, the patient's brain is given priority. However, due to imperfect fitting, some voxels from the Duke's brain also end up in the model. In the final models, on average 95% of the brain volume comes from the patient and 5% comes from the Duke model. In some locations the registration overlap improves the model. For example, the automatic segmentation of the CSF in the patient images misses a lot of the fluid surrounding the brain. In these areas, voxels are assigned based on the CSF from the Duke model. This eliminates any spurious voids where the shape of the skull does not perfectly match the brain.

An additional version of each patient model was made with the tumor absent. The tumor tissue in the model was deleted and replaced with the tissue type determined by the automatic, atlas-based segmentation of the tumor site - either grey or white matter depending on the location. This was done so that the effect of the tumor could be directly observed. The alternative way would be to compare each tumor patient with the Duke model. However, this would add additional SAR variance due to inter-subject variability instead of just the effect of the tumor.

Assigning dielectric properties is a critical component leading to the eventual SAR values. All normal healthy tissue properties were assigned based on literature values for the electrical conductivity, relative permittivity, and density at 298 MHz²⁶. Tumor properties are assigned based on the EPT scans of the four tumor patients at 7T. In the study by van Lier et. al. the conductivity was averaged over the regions correlating to the contrast enhancing part of the tumor and the non-enhancing part of the tumor separately. The resulted in an average measured conductivity of 0.92 S/m and 1.40 S/m in the contrast enhanced and the non-enhancing tumor regions respectively.

Permittivity has a significant effect on local electric fields, thus the local SAR might also be affected. While EPT can be used to also determine permittivity, the

study from van Lier et. al. examined only conductivity of brain tumors. In this study, permittivity of the tumor regions was assigned based on the apparent similarity to other brain tissue. Permittivity and density of the enhancing region of the tumor is assumed to be similar to grey matter given the tumor originates from brain tissue (primary tumors, no metastases) and the fact that the conductivity of the contrast enhanced region is more similar to grey matter than white matter. The non-enhancing section of the tumor is thought to be necrotic or fluid filled. Fluids generally have higher permittivity ($\epsilon_r = 80$ for distilled water), therefore the non-enhancing tumor is assumed to be similar to CSF. This validity of the assumptions for permittivity is validated by conducting a study where the permittivity of the tumor regions are varied. A full table of dielectric properties used can be found in Table 1.

| Table 1 | σ (s/m) | ϵ_r | ρ (g/m ³) |
|-----------------------|----------------|--------------|----------------------------|
| Grey Matter | 0.69 | 60 | 1044 |
| White Matter | 0.41 | 44 | 1041 |
| CSF | 2.22 | 73 | 1007 |
| Tumor (enhancing) | 0.92 | 60 | 1044 |
| Tumor (non-enhancing) | 1.40 | 73 | 1007 |

Table 1: Dielectric properties of simulated brain tumor tissue types

Simulation Parameters

Simulations were performed using a 298 MHz excitation with a simulation time consisting of 50 excitation wavelengths. The results were always checked for numerical convergence and to verify that the simulation reached a steady state. The voxelization grid was designed to include close to 10 million cells as a tradeoff between resolution and simulation time. Typical voxel sizes in the brain are around 10 mm³, with much larger voxels for volumes outside of the head.

The transmit coil was modeled after a two-channel, 16 rung, 7T head birdcage coil (NOVA Medical, Wilmington, MA, USA). This coil has a radius of 15 cm and a length of 17.3 cm. It is surrounded by a copper shield with a radius of 18.5 cm and length of 17.5 cm. The coil is tuned for resonance at 298 MHz using capacitors on the top and bottom end rings. The setup used with this coil at our site allows for each channel to operate independently, however all simulations in this study are with this coil driven in quadrature (90° relative phase shift between ports) - except for one study where it is explicitly stated that different drive configurations are used in order to determine the effect on peak tumor SAR.

Additional Studies

Further simulations were performed using a range of tumor conductivity values in order to determine how much effect conductivity has on the resulting SAR calculations. For these simulations, the tumor was modeled as a single tissue compartment for simplicity. The conductivity of the single compartment model can be compared to the average of the conductivities in the two compartment model, since 10g regions of tissue within the tumor generally contain more than one type of tissue. Conductivity sweep simulations were performed over a range from 0.5 to 3.0 S/m in increments of 0.5 S/m. This range represents the range similar to that seen in the human body at 298 MHz, ranging from normal brain conductivity (0.42 S/m in white matter) to slightly above the maximum conductivity seen over the entire human head (2.2 S/m in CSF)¹⁸.

A similar sweep was done of the tumor permittivity values. It is possible that the permittivity will also differ in a brain tumor compared to normal brain tissue. The simulations of the realistic models assume that the permittivity is slightly elevated compared to normal brain tissue. However, for completeness, additional simulations were performed where relative permittivity was varied through a wide range for conductive tissues at 7T (30-90).

It is also important to try to estimate the peak local SAR in a worst case experiment as opposed to a single generic simulation. In theory, the worst case SAR will occur when the electric field amplitude in the tumor is maximized. Therefore, we take two different approaches to estimating worst case SAR: (1) by changing the amplitude and phase of the ports on the two channel coil to achieve maximum constructive interference of the E field in the tumor and (2) by moving the location of the tumor in the model to the location of the hot spot observed in quadrature drive. This study accounts for the variability of the location of potential brain tumors for hypothetical subjects as well as variance in transmit coils that lead to different E field patterns.

Peak Local SAR Computation

Local SAR maps are generated from the results of the simulations. The solver also allows us to display results in terms of SAR_{10g} maps and automatically calculates the SAR_{p,s} value.

SAR can be related to power through the square of the B1+ field, thus it is helpful for comparison to normalize SAR values to B1+ squared. For this study, the B1+ field was computed as a result of the simulation. The mean B1+ squared was determined based on the axial isocenter slice. This value was used to normalize SAR to units of W/kg per μT^2 .

Results

Tumor Simulation Study

Local SAR is computed from electric field amplitude, conductivity, and density as described in Eq. 1. Fig. 2 compares electric field, conductivity, SAR, and SAR10g distributions for the patient 1 model with and without a tumor. Electric field decreases slightly in the tumor while conductivity increases resulting in a net increase in local SAR. This is easiest to see in the 10g averaged SAR maps showing that SAR10g is increased in the tumor compared to the same region in the model without the tumor.

The other patients showed similar trends. The results of the four patient simulations using tumor conductivity values estimated by EPT, shown in Fig. 3A-D and Fig. 4, reveal that local SAR does in fact increase in the tumor compared to the same region with the tumor absent. However, these results also reveal that the peak simulated SAR over the whole head does not occur in or in the vicinity of the tumor. Instead the peak local SAR, for all patients, occurs near the top of the head (Fig 3A-D, right column).

Global head SAR was calculated for comparison with the peak local SAR value. Global head SAR was not affected very much by the tumor, seen by the fact that global SAR values in the simulations of the models with tumors were very similar to the values for the same patient without the tumor; the average global SAR for the four patients with the tumor was $0.77 \text{ W/kg}/\mu\text{T}^2$ compared to $0.79 \text{ W/kg}/\mu\text{T}^2$ without the tumor present. The SAR limits are defined by the IEC as 10 W/kg for peak local SAR10g and 3.2 W/kg for global average head SAR. Because these numbers both scale proportionally with the square of B1 or the RF pulse duty cycle, the ratio of simulated peak local SAR to global head SAR dictates which factor will be limiting. Fig. 5. shows the calculated ratio for these four patients simulated with and without the tumor. Also shown in the figure is the IEC limit ratio as a dotted line at the value of 3.13. It is typically expected that the local SAR will be limiting for patients at 7T. This is the case for patients 2-4, as seen by their ratios exceeding 3.13. However, for patient 1, the global

SAR is actually the limiting factor over the peak local SAR for this particular simulation.

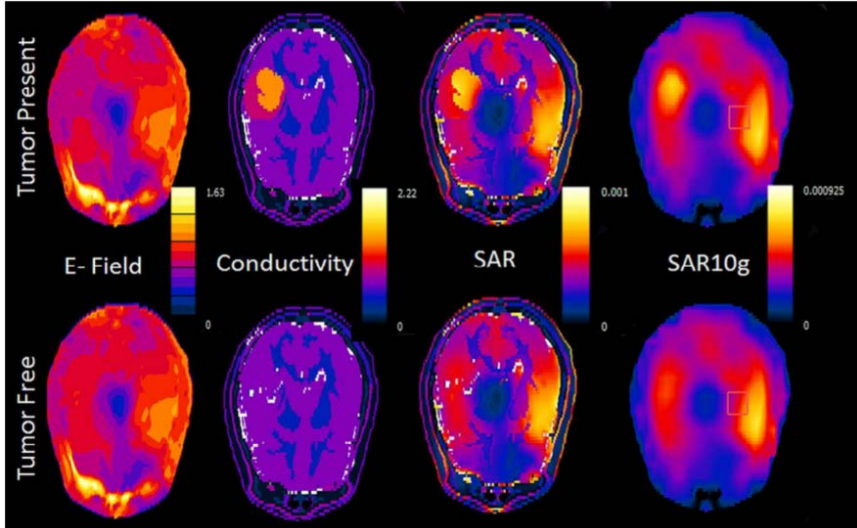


Figure 2: Comparing the E-field, conductivity, SAR, and SAR10g distributions for the tumor (top row) and non-tumor (bottom row) model of patient 1. The E-field is slightly lower in the tumor while the conductivity is considerably higher. The net result is a modest increase in local SAR. This is easiest to see in the 10g averaged SAR maps. The same slice is shown in Fig. 3a.

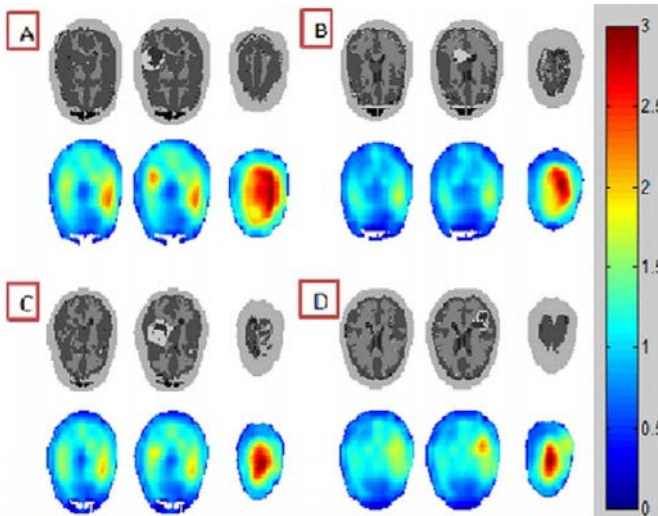


Figure 3: Patients 1-4 are represented by figs. A-D. For each fig., the top row shows an axial slice of the voxelized patient model and the bottom row shows the 10g averaged local SAR maps that correspond to the slice above it. SAR maps have units Watts per kg per microtesla squared. For the columns in A-D: (left) slice through the tumor absent model, (center) equivalent slice through the

tumor model, (right) slice through the point containing the peak local SAR – note that it is same for both tumor present and tumor absent cases so only one is displayed.

Conductivity Simulation Study

Fig. 6A shows that sweeping conductivity has a significant effect on electric field strength. There is a clear decaying trend of the local electric field within the tumor associated with an increase in conductivity. Fig. 6B shows the effect of the diminished electric field on the resulting SAR calculation. While the SAR still increases with conductivity, the effect is clearly not linear.

Permittivity Simulation Study

The results show that permittivity does have an effect on average electric field in the tumor, but the effect is less significant than conductivity. The average of the squared electric field amplitude decreases by about 13% due to sweeping relative permittivity values from 30 to 90. Unlike conductivity, permittivity changes appear to affect the electric field in all four tumors similarly regardless of size or position. Fig. 7 shows that all four tumors experience about the same percentage change in squared electric field when the permittivity is changed. While this amount of variance might seem significant, the value chosen for the realistic model is in the middle of this range, so that maximum deviation from the assumed to be realistic case is only ~7%. This effect is relatively small compared to the conductivity sweep, which shows that increasing conductivity over a reasonable range for brain tumors can cause a 100% or greater increase in average local SAR. Therefore, we base our discussion on simulations that assume a reasonable value for brain tumor permittivity and acknowledge that small deviations from the estimated local SAR are possible.

Worst Case Simulation Study

Two approaches were taken to estimate worst case tumor SAR. The first approach is to assume that the transmit coil drive settings are variable and find the drive setting which causes peak local SAR in the tumor. The second approach is to move the tumor position in the model to the observed hot spot for quadrature drive.

Using the first approach $SAR_{p,s}$, was calculated for each possible parallel transmit drive configuration of the two-channel transmit coil using the patient 1 model, both with and without the tumor. The relative change in $SAR_{p,s}$ value

relative to the tumor-free model for each drive setting is shown in Fig. 8. For most drive settings, including quadrature, $SAR_{P,S}$ is the same because the location of the hotspot is unchanged. However, for some drive configurations, the $SAR_{P,S}$ is increased in the tumor model because the tumor becomes the hotspot location. The worst case drive configuration leads to approximately 19% higher $SAR_{P,S}$ compared to the tumor absent model.

Another way of simulating worst case tumor SAR is restricting the coil to quadrature drive and move the location of the tumor in the head of the model. The tumor was positioned in these simulations based on initial simulations which showed that the peak local SAR value existed outside the tumor, typically near the top of the head. The results of these simulations show $SAR_{P,S}$ increases above the $SAR_{P,S}$ predicted by the model without the tumor present for all four cases (Fig. 9). A maximum increase of 30% is seen in Patient 1.

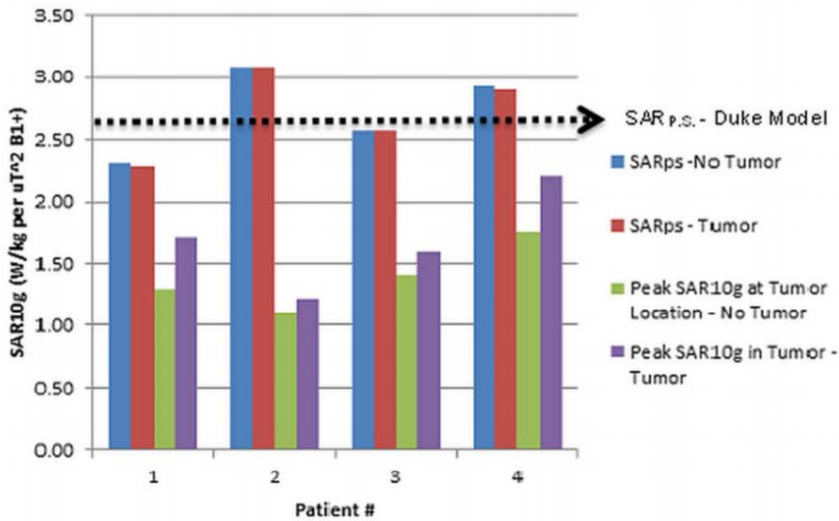


Figure 4: Each patient is simulated twice, once using the tumor model and again using a tumor absent model. From these simulations we compare four values: The peak local SAR for both the tumor model and the control, the peak local SAR over the volume that contains the tumor, and the peak local SAR over the same volume but with the tumor absent. The black dotted line represents the peak local SAR that would be computed using the original 'Duke' generic model.

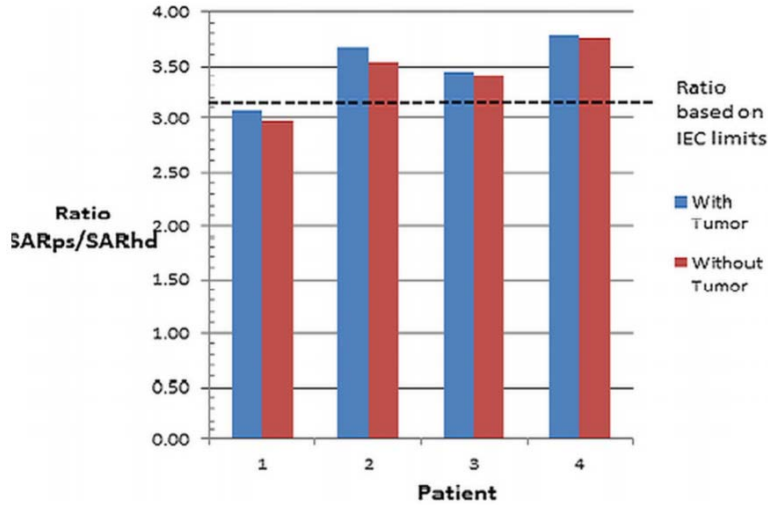


Figure 5: Ratio of peak local SAR (SAR_{ps}) to global head SAR (SAR_{hd}) for the four patient simulations with and without the tumor present. The dashed line represents the ratio of the IEC defined limits for peak local and global head SAR. Below the dashed line, global SAR is the limiting factor. Above the line, peak local SAR is the limiting.

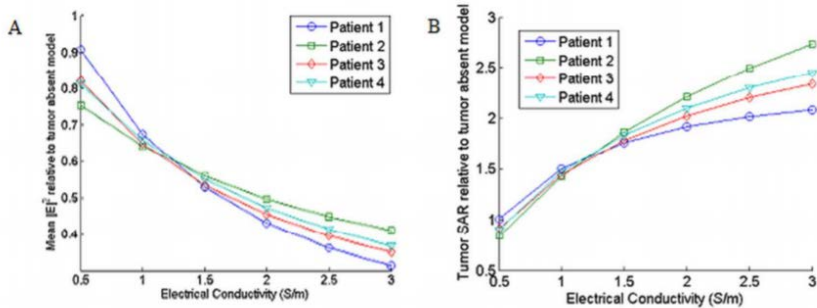


Figure 6: (A) The mean magnitude of the square of the electric field was calculated for each patient over the tumor region using different conductivity values in the simulation. These values are normalized per patient by the value calculated for the tumor absent model in the same region. (B) Relative local SAR change in the tumor compared to the tumor free region as a function of conductivity.

Discussion

Local SAR predictions are typically made using normal, healthy models. The purpose of this study was to calculate peak local SAR in tumor patient models using realistic tumor geometries and conductivity values. It is predicted that increased conductivity of a tumor could potentially lead to an increase in $SAR_{P,S}$. The simulation results shown in Fig. 4 were meant to accurately model the tumor properties and be representative of a typical 7T scan using a birdcage head coil. These simulations show that SAR_{10g} increases locally at the location of the tumor by up to 30% compared to the tumor absent model. However, this increased value does not exceed the $SAR_{P,S}$ which is seen elsewhere in the head. The $SAR_{P,S}$ seen in the tumor models is the same as the $SAR_{P,S}$ for the corresponding tumor absent models.

The simulations also confirm that $SAR_{P,S}$ is, in most cases, the limiting factor over global SAR. However, for one out of the four patients (patient 1), global SAR would actually be the limiting factor. This finding is somewhat contradictory to literature which states that local SAR is “nearly always” exceeded before global SAR⁸. It is also interesting that peak local to global SAR ratios calculated were very close to the IEC defined ratio – with an average ratio of 3.46 in simulation compared to 3.13 per the IEC. This finding, however, is particular to the coil modeled in these simulations.

One finding from this study is that changes in SAR_{10g} are not directly proportional to changes in conductivity. This, however, is not very surprising and could be predicted simply from inspection of Eq. 1. This equation shows that calculation of SAR is most sensitive to changes in electric field strength compared to the other factors since it is weighted quadratically. Regions where high SAR_{10g} is observed are always correlated to areas of high electric field intensity. For all four patient simulations, electric field is higher near the top of the head than in the tumor. It is also at this location near the top of the head where the $SAR_{P,S}$ is observed. However, it is important to note that electric field distribution will change based on many factors related to the setup of an MR experiment. Other combinations of any of the factors affecting electric field distributions (i.e. coil geometries, drive settings, patient size, patient placement, etc.) will lead to different determinations of $SAR_{P,S}$. Therefore, the set of simulations using realistic parameters for one experiment is not enough to show that brain tumors do not lead to an increase in $SAR_{P,S}$ for any generic setup. For this reason, additional studies were done using these four models, including looking specifically at how local SAR is affected by conductivity.

The plot of conductivity versus resulting electric field strength in Fig. 6A shows that local electric field strength decreases in response to a local increase in conductivity while all other simulation parameters remain the same. This is interesting because it means that highly conductive tumors appear to have a strong influence on the electric field distribution. The increase in conductivity leads to a shielding effect, preventing the electric field from penetrating deep into the tumor. In fig. 6B, average tumor local SAR is plotted as a percent increase relative to the average local SAR in the same region of the tumor absent model. While average SAR increases with conductivity, the effect is small compared to the large change in conductivity. This finding partially explains the results of the realistic tumor model simulations, where SAR_{10g} increased locally by around 30% while conductivity was increased by over 100% for the tumor models compared to the tumor absent models.

A further consideration is that various experimental setups could potentially lead to an electric field distribution that has a maximum at the tumor location. For example, the SAR_{p,s} location is typically seen near the very top of the head when using the birdcage coil described in this study - it is not uncommon for tumors (meningioma) to develop in this area. To simulate such a worst-case SAR situation, each patient was simulated again with the tumor position moved to the location where SAR_{p,s} is observed in the tumor absent model. Simulations of the tumor in this location now show that SAR_{p,s} increases in the tumor model compared to the tumor absent model. SAR_{p,s} increases in the worst case tumor model by as much as 30% (Patient 1, Fig. 9).

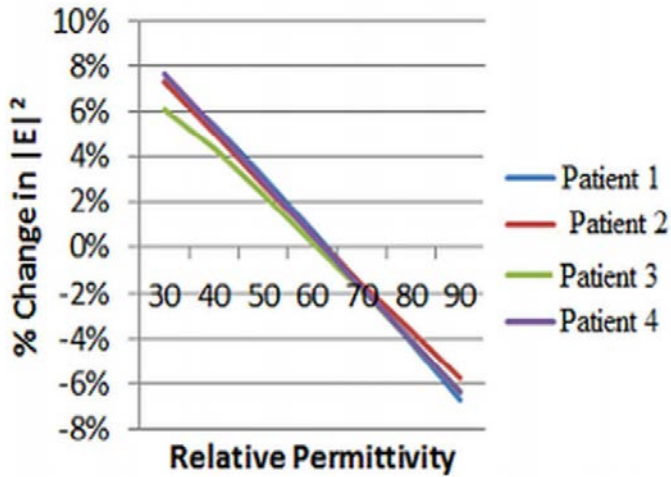


Figure 7: Increasing the relative permittivity causes a decrease in the average of the squared electric field amplitude in the tumor. The plot shows the change in squared electric field amplitude in percent for all four tumor patient models compared to the simulations with the assumed permittivity values used for all other simulations (60 for the enhancing tumor region and 73 for the non-enhancing tumor region). Note that changes in squared electric field amplitude are directly proportional to changes in local SAR.

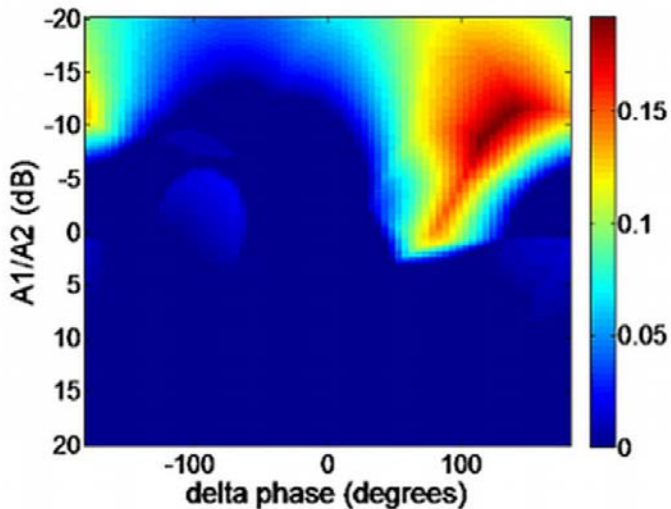


Figure 8: Relative increase in SARps calculated in the tumor model compared to the tumor absent model of Patient 1 for different drive settings. On the left axis is the voltage amplitude ratio between the two ports in decibels. On the bottom axis is the relative phase offset of port 2 to port 1. Quadrature is defined to be zero degrees offset.

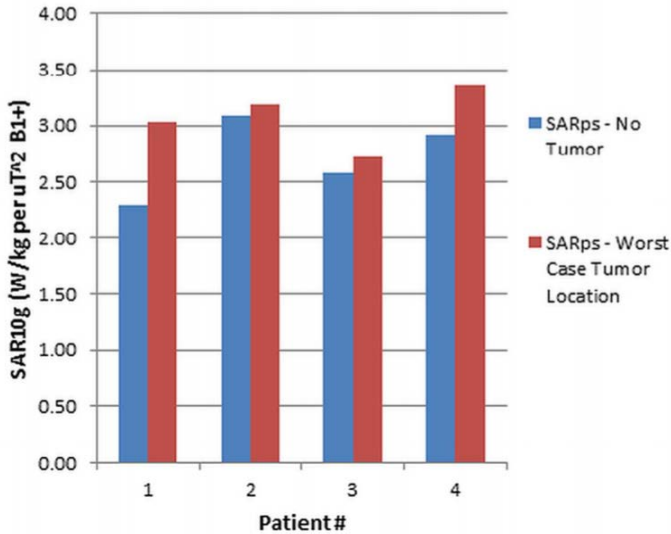


Figure 9: For each patient, the peak local SAR for the tumor absent model is plotted versus the peak local SAR for the model with the tumor moved to the location SAR hot spot (worst case). As expected, the worst case SAR model has peak local SAR values that exceed the tumor absent model peak local SAR.

The uniqueness of this study is that models were constructed of real brain tumors using actual in-vivo measurements of conductivity. However, in our attempt to make our models realistic, some tradeoffs had to be made. Challenges associated with the segmentation of the available images resulted in our models being slightly less detailed than models from the Virtual Family. Additionally, integrating the patient brain into the head of the Duke model creates some unrealistic features in the final model. However, we do not expect these deviations to have a large impact on resulting $SAR_{p,s}$ calculations, especially since these features are rare and exist in areas outside of either the tumor or the $SAR_{p,s}$ location. Furthermore, we do not see any obvious artifacts or discontinuities in the resulting EM field distributions which would signify a major error in the model. It is important to point out that there are very small inaccuracies inherently involved in any FDTD simulation due to stair-casing effects from the voxelization as well as assumptions about tissue types/properties. We must accept that the result is a close estimation of a real excitation and not be overly concerned with model perfection.

The results of this study highlight the fact that brain tumors should be an additional variable to consider when it comes to $SAR_{p,s}$ prediction. The effect of subject variability on SAR and the known inaccuracy of numerical simulation are

typically accounted for in practice by incorporation of a SAR safety tolerance factor. $SAR_{p,s}$ estimated through simulation is multiplied by a safety tolerance factor to ensure that local SAR determination is not underestimated. Based on this study, it would be advised to incorporate an additional safety tolerance factor when scanning a brain tumor patient using a head coil at 7T. Estimated $SAR_{p,s}$ should in that case be multiplied by an additional factor of 1.3. This number comes from the fact that the worst case $SAR_{p,s}$ increase seen in this study is 30%.

It is also worth noting that the $SAR_{p,s}$ limit is determined due to possible deleterious effects on healthy tissue. Local heating due to SAR in brain tumors might not have any negative impact on healthy tissue as it is used as a therapy sensitizer. Our recommendations are made strictly based on aforementioned restrictions by the IEC and FDA which do not distinguish between peak local SAR in healthy versus cancerous tissue.

Conclusion

The $SAR_{p,s}$ prediction for any particular scan will generally be based on a simulation using a healthy generic model. This can be a problem because brain tumors are known to have significantly higher electrical conductivity than healthy brain tissue. We conclude from this study that brain tumors can lead to higher peak local SAR than that predicted using a generic model. However, the peak local SAR increase due to the presence of a tumor, even in the worst cases, is relatively small. Larger differences in local SAR prediction have been observed from studies looking at inter-subject variability and coil –patient positioning. Increased tissue conductivity reduces the local electric field, effectively limiting any extreme conductivity related local SAR increase. $SAR_{p,s}$ will increase above the predicted value if the tumor is located at the region where the electric field spatially peaks. In this worst case, using a healthy model for SAR prediction will result in an underestimate of $SAR_{p,s}$ for a brain tumor patient, possibly even after incorporation of a standard safety tolerance factor. Therefore, it is recommended that an additional safety tolerance factor is incorporated into $SAR_{p,s}$ predictions when scanning a brain tumor patient at 7T.

References

1. Hoult DI, Phil D. Sensitivity and power deposition in a high-field imaging experiment. *Journal of magnetic resonance imaging : JMRI*. 2000;12(1):46–67.
2. Bottomley PA, Andrew ER. RF magnetic field penetration, phase shift and power dissipation in biological tissue: implications for NMR imaging. *Physics in medicine and biology*. 1978;23:630–643.
3. Collins CM, Wang Z. Calculation of radiofrequency electromagnetic fields and their effects in MRI of human subjects. *Magnetic resonance in medicine*. 2011;65(5):1470–82.
4. Center for Devices and Radiologic Health. Guidance for the submission of premarket notifications for magnetic resonance diagnostic devices. Rockville: Food and Drug Administration; 1988.
5. International Electrotechnical Commission. International standard, medical equipment—part 2: particular requirements for the safety of magnetic resonance equipment for medical diagnosis, 2nd revision. Geneva: International Electrotechnical Commission 2002; 601:2–33.
6. Zhang X, Schmitter S, Van De Moortele PF, Liu J, He B. From Complex B1 Mapping to Local SAR Estimation for Human Brain MR Imaging Using Multi-Channel Transceiver Coil at 7T. *IEEE Transactions on Medical Imaging*. 2013;32:1058–1067.
7. Voigt T, Homann H, Katscher U, Doessel O. Patient-individual local SAR determination: In vivo measurements and numerical validation. *Magnetic Resonance in Medicine*. 2012;68:1117–1126.
8. Oh S, Webb AG, Neuberger T, Park B, Collins CM. Experimental and numerical assessment of MRI-induced temperature change and SAR distributions in phantoms and in vivo. *Magnetic resonance in medicine : official journal of the Society of Magnetic Resonance in Medicine / Society of Magnetic Resonance in Medicine*. 2010;63(1):218–23.
9. Zhu Y, Alon L, Deniz CM, Brown R, Sodickson DK. System and SAR characterization in parallel RF transmission. *Magnetic resonance in medicine : official journal of the Society of Magnetic Resonance in Medicine / Society of Magnetic Resonance in Medicine*. 2012;67(5):1367–78.
10. Wang Z, Lin JC, Mao W, Liu W, Smith MB, Collins CM. SAR and temperature: simulations and comparison to regulatory limits for MRI. *Journal of magnetic resonance imaging : JMRI*. 2007;26(2):437–41.
11. Van den Berg C a T, van den Bergen B, Van de Kamer JB, Raaymakers BW, Kroeze H, Bartels LW, Lagendijk JJW. Simultaneous B1 + homogenization and specific absorption rate hotspot suppression using a magnetic resonance phased array transmit coil. *Magnetic resonance in medicine*. 2007;57(3):577–86.

12. Buchenau S, Haas M, Hennig J, Zaitsev M. A comparison of local SAR using individual patient data and a patient template. In: Proceedings 17th Scientific Meeting, International Society for Magnetic Resonance in Medicine. Vol. Honolulu. 2009. p. 4799.
13. Christ A, Kainz W, Hahn EG, Honegger K, Zefferer M, Neufeld E, Rascher W, Janka R, Bautz W, Chen J, et al. The Virtual Family--development of surface-based anatomical models of two adults and two children for dosimetric simulations. *Physics in medicine and biology*. 2010;55(2):N23–38.
14. Dimbylow PJ. Fine resolution calculations of SAR in the human body for frequencies up to 3 GHz. *Physics in medicine and biology*. 2002;47:2835–2846.
15. Murbach M, Neufeld E, Kainz W, Pruessmann KP, Kuster N. Whole-body and local RF absorption in human models as a function of anatomy and position within 1.5T MR body coil. *Magnetic Resonance in Medicine*. 2014;71(2):839–845.
16. De Greef M, Ipek O, Raaijmakers AJE, Crezee J, van den Berg C a T. Specific absorption rate intersubject variability in 7T parallel transmit MRI of the head. *Magnetic resonance in medicine*. 2013;69(5):1476–85.
17. van Lier ALHMW. Electromagnetic and Thermal Aspects of Radiofrequency Field Propagation in Ultra-High Field MRI. PhD Thesis. Enschede: Ipskamp Drukkers; 2012.
18. AL Van Lier, JM Hoogduin, DL Polders, VO Boer, J Hendrikse, PA Robe, PA Woerdeman, JJ Lagendijk, PR Luijten C van den B. Electrical conductivity imaging of brain tumours at 7T. Proceedings of the 19th Annual Meeting of ISMRM, Montréal, Canada. 2011:4464.
19. Tha KK, Stegning C, Suzuki Y, Katscher U, Keupp J, Kazumata K, Terasaka S, Van Cauteren M, Kudo K, Shirato H. Noninvasive Evaluation of Electrical Conductivity of the Normal Brain and Brain Tumors. In: ISMRM 2009 Proceedings. 2009. p. 1885.
20. Katscher U, Voigt T, Findekle C, Vernickel P, Nehrke K, Dössel O. Determination of electric conductivity and local SAR via B1 mapping. *IEEE transactions on medical imaging*. 2009;28:1365– 1374.
21. Volakis JL, Caputa K, Okoniewski M, Stuchly M a. An algorithm for computations of the power deposition in human tissue. *IEEE Antennas and Propagation Magazine*. 1999;41(4):102–107.
22. Polders DL. Quantitative MRI of he human brain at 7 tesla. PhD Thesis. Utigeverij BOXPress; 2012.
23. Sacolick LI, Wiesinger F, Hancu I, Vogel MW. B1 mapping by Bloch-Siegert shift. *Magnetic Resonance in Medicine*. 2010;63:1315–1322.
24. Van Lier ALHMW, Brunner DO, Pruessmann KP, Klomp DWJ, Luijten PR, Lagendijk JJW, van den Berg C a T. B1(+) phase mapping at 7T and its application for in vivo electrical conductivity mapping. *Magn Reson Med*. 2012;67:552–61.

25. Fedorov A, Beichel R. 3D Slicer as an image computing platform for the Quantitative Imaging Network. *Magn Reson Imaging*. 2012; 30(9):1323–1341.
26. Hasgall PA, Di Gennaro F, Baumgartner C, Neufeld E, Gosselin MC, Payne D, Klingeböck A, Kuster N. “IT’IS Database for thermal and electromagnetic parameters of biological tissues,” Version 2.5. www.itis.ethz.ch/database. Published August 1st, 2014. Accessed January 19, 2015.

Chapter 3

Improving Peak Local SAR Prediction in Parallel Transmit Using In-situ S-matrix Measurements

Matthew Restivo, Alexander Raaijmakers, Cornelis A.T. van den Berg, Peter Lujten, and Hans Hoogduin

Abstract

Purpose: Peak local specific absorption rate (pSAR10g) is an important parameter used to determine patient safety during RF transmission. pSAR10g predictions for parallel transmit MRI are affected by the level of coupling exhibited by a modeled array in the simulation environment. However, simulated array coupling is rarely equal to the physical array coupling. Accurately simulating the physical array coupling may improve the accuracy of predicted SAR levels.

Methods: The coupling (S-matrix) of a prototype 4-channel array was measured in-situ using directional couplers installed on a 7T scanner. Agreement between the simulated and measured S-matrix was achieved by using network co-simulation with a modified cost function. B1+ maps acquired in a phantom were compared to B1+ distributions determined from simulations.

Results: The modified co-simulation technique forces the simulations to have similar S-matrices to the measured values. A comparison of realistically vs. ideally simulated coupling conditions shows that ideally simulated coupling can result in large (>40%) error in pSAR10g predictions, even when the array is reasonably tuned. The simulated B1+ distributions match the measured B1+ distributions better when the coupling is accurately simulated.

Conclusion: Considering the measured array coupling matrix in numerical simulations eliminates a potential confound in pSAR10g prediction.

Introduction

At high field (3T and above), the radio frequency (RF) wavelength in tissue is approximately the same or shorter than the width of the human body, resulting in RF B1-field inhomogeneity.^{1,2} As a result, parallel transmit (pTx) is becoming more common in high-field magnetic resonance imaging (MRI) to correct for signal voids that occur due to inhomogeneous B1-field distributions.³ pTx arrays are composed of multiple elements driven independently, thus allowing the RF electromagnetic field to be steered (or shimmed) by varying the amplitude and phase relationships among the channels.⁴ However, while image quality is related to the RF magnetic field, it must be considered that the RF electric field interference, which is also affected by shimming, can cause significant temperature rise in tissue due to RF energy deposition expressed by the specific absorption rate (SAR).⁵

SAR, which arises from electrical RF currents in tissue generated by induction due to the RF pulses, must be controlled to ensure patient safety while scanning. The IEC⁶ and FDA⁷ outline guidelines for maximum permissible SAR defined globally (i.e. total delivered power per patient mass) and locally. At field strengths where pTx is common (>3T), it has been shown that localized heating related to the local SAR distribution is more of a safety risk than the global SAR related heating.⁸ Therefore, it is important to ensure that the 10g averaged peak local SAR (pSAR10g) is controlled.

Unfortunately, while global SAR can be approximated by monitoring the power balance using directional couplers during the scan⁹, the local SAR distribution cannot be easily probed and monitored in real time. Methods that best approximate local SAR in-vivo based on B1 mapping¹⁰ or MR thermometry¹¹ are not yet accurate or robust enough to ensure safety. Instead, we rely on numerical simulations of the RF electromagnetic field. Advanced modeling and simulation software in conjunction with highly detailed patient models help improve the precision of EM simulations;^{12,13} however, there are still many sources of error. For example, local SAR distributions are highly dependent on the specific geometry and anatomy of the subject, thus inter-subject variability of pSAR10g values may be high. A number of studies have investigated inter-subject variability^{14,15} and there even exist some proposed solutions, such as the creation of patient-specific body models specifically for safety assurance.^{16,17} Furthermore, it is necessary that numerical models be validated prior to relying on simulations for determining RF power limits. Procedures for validation of numerical models has been described in prior literature.^{18,19}

RF coupling of pTx array elements also has a large effect on local SAR predictions. In general, it is desirable to limit coupling by mutual overlapping of loop elements or through lumped-element decoupling networks. This works well for nearest neighbor coupling, but it is more difficult to decouple all elements, especially as the number of channels increases. Thus, some level of coupling exists for almost all pTx arrays. Coupling is best described by scattering parameter matrices (S-matrices).²⁰ Each element of the S-matrix is the complex ratio of reflected signal on a particular Tx channel to incident signal on the same or a different Tx channel. It is feasible to measure the physical pTx array coupling in the MR scanner by including directional couplers in the transmission lines that separately measure incident and reflected power for each channel.²¹ A major problem affecting numerical simulation is that the S-matrices of highly coupled arrays are difficult to replicate realistically. In simulation, coupling conditions are affected by many of the simplifications used in the simulation environment; for example stair-casing resulting from voxelization of the computerized model. Network co-simulation is a relatively novel technique that allows the electric circuits in an RF array to be optimized in conjunction with EM field simulation. It is traditionally used as a fast and robust method to optimize the lumped-element values in simulated array models based on ideal tuning, matching, and coupling conditions^{22,23}. Co-simulation works well to present a proper power balance in simulation for arrays that exhibit very low coupling.^{18,24} However, it is important to note that the physical array coupling is not always equal to the ideal conditions traditionally specified in co-simulation, and may vary significantly with loading. Realistic coupling should be considered as an important simulation parameter when simulating a pTx array to evaluate SAR safety or predicting pSAR10g levels. Since we are able to measure the physical array coupling in-situ with directional couplers, we can adapt the optimization of the co-simulation to instead find the lumped-element values which cause the simulated coupling to most accurately match the measured coupling, instead of assuming ideal array performance.

Peak local SAR becomes more difficult to predict as the number of channels and cross-coupling in parallel transmit MRI increases. The current strategy to compensate for simulation errors is to be very conservative in pSAR10g estimates by only considering the value produced by the worst-case constructive interference of electric fields.²⁵ The array is then limited in terms of B1 pulse amplitude, duration, and duty cycle based on this conservative assumption. In this work we show that realistically simulating the pTx coupling results in better EM field predictions. Increased confidence in pSAR10g predictions may allow for the restrictions on pTx arrays to be relaxed while still ensuring patient safety.

Methods

Measurements

The proposed method was tested at 7T using a prototype 4-channel Tx/Rx head array consisting of four rectangular loop coils distributed 90° apart (Fig. 1). The loop elements are 20 cm long and 10 cm wide with 11 capacitors distributed around the conductor path and one additional capacitor in parallel with the driving port. The four elements are shielded by an aluminum cylinder of 45 cm diameter and 30 cm height. The array was loaded with a 10 cm spherical phantom with known dielectric properties ($\sigma=1.0$ S/m, $\epsilon_r=80$, as measured with an Agilent 85070E dielectric probe) placed in the center of the array.

Directional couplers were fully integrated into a Philips 7T MR scanner with 8x2kW RF amplifiers. Eight directional couplers (EME 7020/30A, EME-HF-Technik) were installed in series with each of the coax transmission lines connecting the RF amplifier and the TR switch. The amplifiers are protected by circulators which deposit backwards power in a dummy load equal to the transmission line characteristic impedance (50 Ohm). The sampled signals at the couplers were calibrated to relate to the forward and backwards propagating waves at the coil connection plane. Calibration was performed by measuring the directional couplers with a well-defined open, short, and 50 Ohm calibration tool attached at the coil connection plane.

The S-matrices were measured with the array and phantom in-situ. S-matrices were computed from a quick dynamic sequence where forward power is delivered to one channel at a time and the reflections are monitored on all channels. B1+ maps were acquired with the loaded array right after S-matrix measurement for comparison with simulations. B1+ distributions were determined using low flip angle gradient echo (low FA GE) images because of superior dynamic range in comparison to other B1+ mapping techniques²⁶. A 10° flip angle was used to ensure that the low tip-angle approximation is valid such that low FA GE signal intensity is proportional to B1+ (i.e. below the Ernst angle of approximately 25° for the 500 ms T1 of the phantom and a 50 ms TR). B1-magnitude was divided out after determining B1- as the ratio of a 3D quadrature Actual Flip Angle (AFI) B1+ map²⁷ and quadrature low FA GE image. Dividing each low FA GE image by the complex low FA GE quadrature image subtracts out the receive phase, however the transmit phase of the quadrature image remains. In Fig. 1B, where the per channel phase images are shown, the simulated per channel phase images are also displayed relative to the quadrature transmit phase for direct comparison. The AFI B1+ used a flip angle of 50° and a

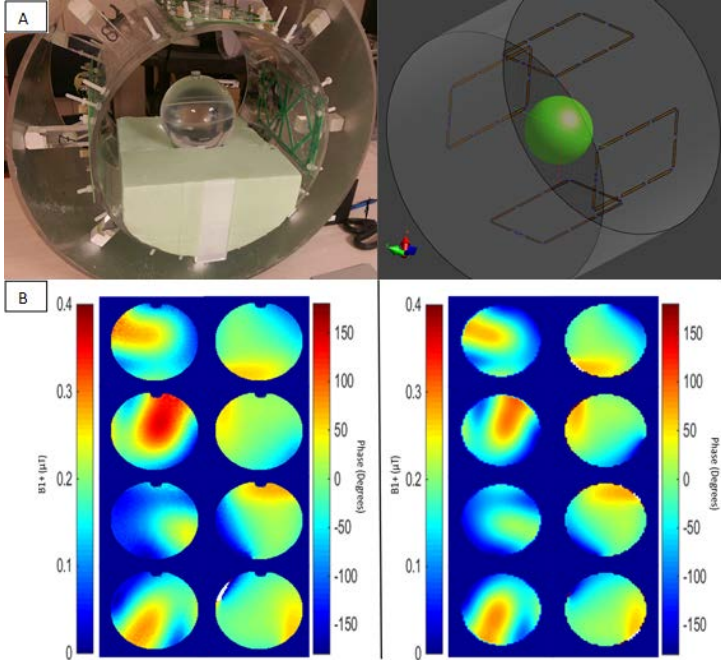


Figure 1: **A.** (Left) Experimental setup consists of 4 loop elements and a metallic shield surrounding a 10 cm diameter spherical phantom. (Right) The experimental setup modeled in Sim4Life. Gaps in the loop elements signify locations of the capacitors. **B.** The per channel B1+ amplitude and phase maps (relative to quadrature Tx phase) are compared between the measured (left) and simulated (right) values. **C.** Close up image of a single loop coil element.

dual TR ($TR_1 = 67$ ms, $TR_2 = 267$ ms). Low FA GE images are acquired with $1 \times 1 \times 1$ mm resolution for a grid size of $244 \times 244 \times 13$. The AFI B1+ map was acquired with a $2 \times 2 \times 2$ resolution, but reconstructed to $1 \times 1 \times 2$ to maintain the same FOV and grid size in the transverse plane as the Low FA GE images.

Network Co-Simulation

Network co-simulation is performed by simulating all lumped-elements and sources as transmitting ports while the remaining ports are terminated with a reference impedance. This allows for the scattering parameters of all the modeled ports to be determined. The S-matrix of the complete system can be reduced by assigning a complex impedance value (corresponding to a capacitance or inductance) to the ports that are in reality lumped-elements in the physical array. Solving for the reduced S-matrix, as described in literature^{22,23}, allows for the realization of the S-matrix for the modeled array with only the ports that correspond to the actual Tx channels in the physical array.

Typically in co-simulation, the ideal capacitor values are found through optimizing the S-matrix based on a target cost function. A common cost function for optimal array tuning is the 2-norm of the simulated S-matrix (i.e. minimum reflected power, where reflected power is defined as both self-reflections and backwards power coupled in from other elements)²⁴. Optimizing on minimum reflected power results in an ideal coupling condition, but does not necessarily reflect the realistic coupling of the physical array in the MR scanner. Instead, defined here is a modified cost function as the 2-norm of the difference between the simulated output S-matrix (S_{out}) and the measured S-matrix.

$$cost = \|S_{out}(C) - S_{measured}\| \quad [1]$$

The optimization returns a vector of capacitor values, C , such that the complex difference between measured and simulated S-matrix is minimized.

The experimental setup was modeled and simulated using Sim4Life (ZMT AG, Zurich). For co-simulation, all capacitors and sources were simulated as transmitting ports while the remaining ports were terminated with 50 ohms. The array consists of four loop elements each with 11 series capacitors, 1 parallel capacitor, and 1 actual source – thus resulting in 52 separate EM simulations. The grid included 2.57 MCells. The resolution of the grid is variable depending on the size of the structure being resolved. The dimensions of the voxels consisting of part of the coil or phantom are all less than 1x1x2 mm. Convergence of the broadband simulations was checked by ensuring at least 98% of the input power is dissipated in the environment within the simulation time. Each simulation converges fairly quickly using the co-simulation method due to the fact that the coil structures are not resonant given that no lumped elements are used.

The electric circuit side of co-simulation was implemented using Python scripting in conjunction with Sim4Life. The optimization of capacitor values was implemented using the SciPy²⁸ minimization routine using the cost function described above. Series capacitors in each loop element were assigned to a single group to distribute the capacitance equally as well as reduce the complexity of the minimization search. Each element also has a capacitor parallel to the source that is part of the matching network. This results in two capacitor groups per element and a total of eight groups in the electric circuit simulation routine. The minimization function with eight optimization variables will often find local minima that are not necessarily the global minimum. To find the global minimum, the optimization is repeated many times using randomly generated

seed values. For this simulation, 300 iterations yielded a stable global minimum solution, based on the fact the same minimum was achieved in at least three consecutive executions. The capacitor values that result in the smallest cost function are used to determine the driving weights of all 52 ports of the EM simulation. There is no need to solve the EM simulation again to determine the overall field patterns. This network-side optimization takes approximately 5 minutes on a PC with a 3.40 GHz processor.

Co-simulation was also performed using a cost function based on minimized total reflected power, for comparison with the proposed method. Simulated B1+ maps and E-field distributions were extracted after execution of the S-matrix optimization. E-field distributions were then used to calculate 10g-averaged local SAR distributions and evaluate the maximum value (pSAR10g).

A comparison was also done using a human model (Duke of the Virtual Population) with the array centered on the head. pSAR10g was computed using simulations with elements tuned based on ideal coupling and realistically measured coupling from the phantom study. Q-matrices were computed based on the E-field distributions for each of the four channels and averaged over 10g cubes to yield the appropriate SAR metric. Using Q-matrices, pSAR10g can be computed quickly for a large number of random drive settings. pSAR10g was calculated for 3000 randomly generated drive settings all normalized to 1W delivered power, based on determining the forward and reflected power in each setting then scaling the forward drives appropriately.

Results

Co-simulation based on the modified cost function (Eq. 1) yields a simulated S-matrix that closely approximates the measured S-matrix, shown in Figure 2. Note that some differences appear large in Fig. 2 due to the dB scale – large negative numbers all correspond to very small absolute power coupling. It is not so important to match exactly the amplitude or phase for the smallest value entries in the S-matrix since they will not have a large effect on the overall power balance or field distribution. It is most important to accurately match the largest entries of the measured S-matrices. The small difference between measured and simulated coupling remains because it is difficult for the model to perfectly mimic the real setup, thus not all S-matrices are realizable by adjusting only the lumped element values. In contrast, using co-simulation to simulate an array tuned for minimum reflected power produces a noticeably different S-matrix; particularly in phase, which is important for linear super-positioning of complex-

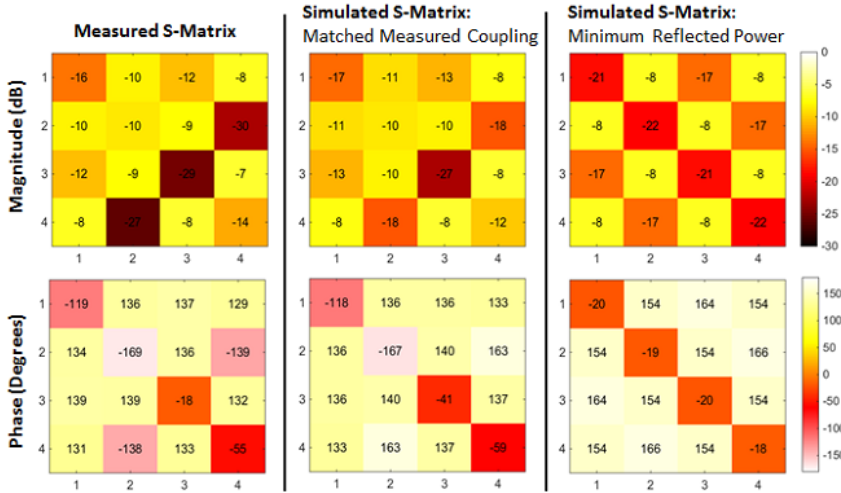


Figure 2: Measured S-matrix (magnitude and phase) compared to simulated S-matrices after circuit co-simulation. The “Matched Measured Coupling” condition uses the proposed modified cost function. The “Minimum Reflected Power” condition uses a typical co-simulation cost function based on minimizing reflected power.

valued EM field distributions (Fig. 2). The norm of the difference between the measured and simulated S-matrices evaluates to .15 when the modified cost function is used compared to .55 when the simulation is optimized for minimum reflected power.

The measured and simulated (using the matched S-matrix method) per channel B1+ distributions are shown in Fig. 1B. The similarity between the simulations and the measurements, with respect to the B1+ pattern and relative phase validates, in part, that the model geometry is accurate compared to the experimental setup. Additionally, the similarity in the phase images signifies that the dielectric properties of the phantom are approximately correct in the simulation.

B1+ maps were normalized to the incident power necessary to achieve 1 uT peak B1+ in the center of the phantom when the array is driven in quadrature – for ease of comparison with measurements. Due to the more optimal array performance of the co-simulation based on minimum reflected power, the quadrature B1+ maps for this situation correspond to 1.23 W total incident power, compared to 1.56 W for the simulations using the matched coupling condition. The same incident power is used for normalization of all other drive configurations of the same simulation as well. Differences in pSAR10g determination result between the two simulated coupling conditions even after accounting for different B1+ efficiency, signifying a noticeable difference in the

E-field interference patterns and not just a magnitude scaling based on different total delivered power. Differences in predicted pSAR10g vary up to 41% (Fig. 3, Drive 1) using the method to match the measured coupling compared to the traditional method of assuming an ideally optimized array. Ignoring B1+ and normalizing to the same level of incident power would lead to even larger pSAR10g disagreement.

The normalized root mean square errors (NRMSE) between the simulated and measured B1+ are reduced by simulating with the measured coupling. However, both simulations produce very similar quadrature B1+ images due to the fact that the two nearest-neighboring of each element are transmitting with equal power and opposite phase, resulting in an approximately decoupled situation. Larger differences are seen with more unbalanced drive settings (Drive 1 and 2 in Fig. 3) which are more affected by the coupling condition.

Given that the 4-ch array was relatively well tuned compared to the ideal case, we repeated the method for a different measured coupling condition to observe more extreme differences in pSAR10g prediction. The four array elements were replaced with four different array elements which were not thoroughly tuned and matched. One of the elements (Ch 2) showed particularly high self-reflection, indicative of poor tuning. This measured S-matrix was used replicated in simulation using the same adapted co-simulation method and then used to predict pSAR10g. The result (Fig. 4) demonstrates the variability of pSAR10g predictions with coupling conditions. Poor tuning can occur unintentionally in practice because coils are often tuned and matched in the lab using a single subject or phantom. Changes in loading and environment often result in coupling changes when imaging different subjects inside the scanner bore relative to coupling measured during coil construction

For the human model, pSAR10g predicted using ideal tuning is on average 33% higher than the pSAR10g predicted using realistic coupling for a large number of drive settings. As seen in Fig. 5, pSAR10g can be overestimated using ideal tuning by over 100% and underestimated by as much as 20% compared to a realistically coupled simulation. Some institutions use pSAR1g instead of pSAR10g because 10g averaging may smooth localized SAR hotspots that might lead to a significant local temperature increase. Evaluating pSAR1g shows slightly higher values compared to pSAR10g as expected. However the relative difference in predicted peak SAR over random drives shows a similar trend for both pSAR10g and pSAR1g (Fig. 5), signifying that the local SAR variance due to coupling exists for both metrics.

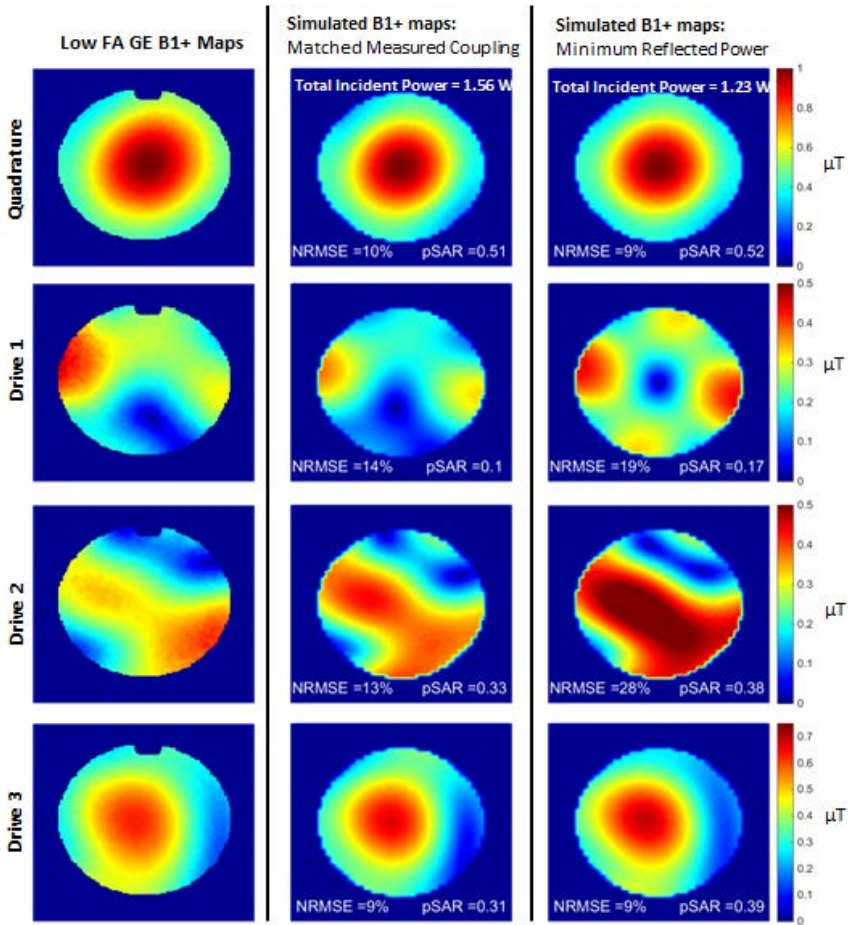


Figure 3: Comparison of measured and simulated B1+ maps for the array driven with equal drive amplitude and various relative phases. Drive configurations shown are quadrature i.e. [0,90,180,270] degrees for counterclockwise elements starting from the bottom, Drive 1 [0,90,0,90], Drive 2 [0,90,0,-90], and Drive 3 [0,45,90,135]. Simulated B1+ fields are scaled to the total incident power required to achieve 1 μT peak B1+ in quadrature. The right-most column shows the differences between the B1+ distributions for the two simulated coupling conditions ($B1+_{ideal} - B1+_{realistic}$), highlighting the difference in the underlying field patterns as opposed to simply a difference in intensity.

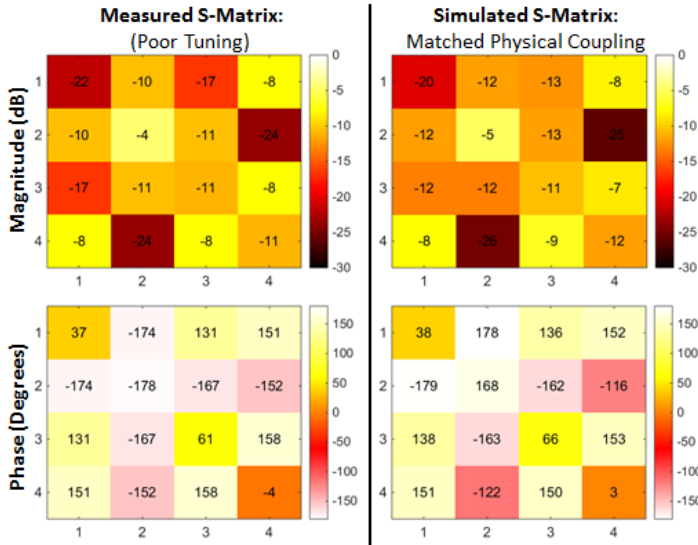


Figure 4: A comparison of simulated pSAR10g using the same array with different coupling conditions. All simulations are scaled by the total incident power required to achieve 1 μ T peak B1+ in quadrature. Total incident power = 1.23 W for the minimum reflection, 1.56 W for coupling condition 1, and 1.32 W for coupling condition 2. Aside from quadrature, all drive settings result in a predicted pSAR10g value that is dependent on the coupling condition. Additionally, pSAR10g does not systematically appear to be lower or higher for any particular coupling condition.

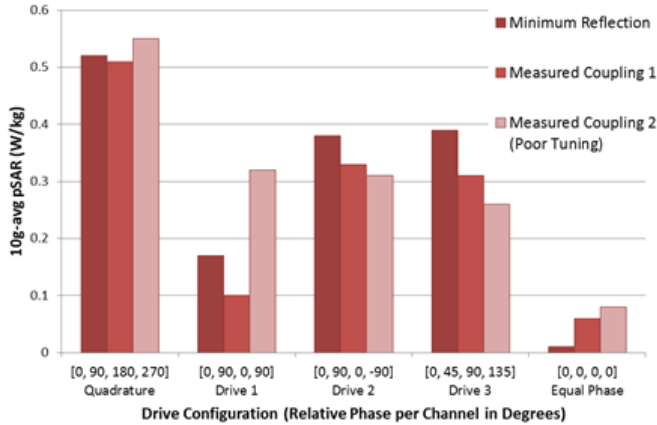


Figure 5: pSAR10g (top) and pSAR1g (bottom) calculated in a human head model for 3000 randomly generated drive settings normalized to 1 W delivered power. The ideal coupling situation is determined from traditional co-simulation and the realistic coupling situation is determined from the proposed method, using the measured S-matrix shown in Fig. 2. The relative difference is the potential error in pSAR when using traditional co-simulation instead of the proposed method (i.e. $\frac{pSAR_{ideal} - pSAR_{realistic}}{pSAR_{realistic}} * 100$) and sorted in ascending order.

Discussion

The current best practice for considering coupling in simulations is to use network co-simulation for optimization of an idealized coupling condition. The results of this study show that simulating in this fashion could yield pSAR10g predictions that are very different from a more accurately simulated coupling condition. The hypothesis that more accurate coupling in simulation directly translates to a more accurate SAR prediction is supported by the fact that measured B1+ maps are better estimated by more realistically coupled simulations compared to the ideally coupled simulations. B1+ maps are used because it is the easiest field distribution to measure using the MR scanner. However, further validation could involve probing local SAR through MR thermometry measurements³⁰ or E-field probes.

Previous studies have taken a different approach to addressing the problem of correctly simulating coupling. Beqiri et. al. evaluated ideal decoupling strategies to avoid simulating coupling; however, the result was that ideally decoupled fields could not be linearly combined to replicate the fully coupled field distribution for a 8-ch body array.²³ Here it is shown that measured coupling can be included in the simulations instead of finding solutions that neglect coupling altogether. However, a key limitation of this method is the assumption that coupling can be accurately measured. Noise in the directional coupler measurements or difficulty in directional coupler calibration could result in unreliable pSAR10g prediction.

While subject-specific pSAR10g variability remains a critical impediment to accurate pSAR10g predictions, variability based on coupling conditions appears to be on a similar order of magnitude. Previous studies have determined that subject-dependent pSAR10g variability in a birdcage headcoil is on the order of 60%¹⁵. Fig. 5 shows average pSAR10g variability of 33% in simulations using ideal coupling as opposed to realistic coupling for a human head. Fig. 4 suggests the variability increases with the dissimilarity between the real array coupling and the simulated coupling condition. Additionally, this method can potentially partially compensate for a mismatch between the subject and body model, given that array loading variations will be detected by the S-matrix measurement. Forcing the S-matrix to be matched will at least ensure that the power balance of the array channels is correctly simulated.

In the human model as well as in the phantom, the ideally coupled simulation results in generally higher pSAR10g values for most drive settings even after

compensating for the difference in power balance. A possible interpretation of this result is that the highest SAR values are a result of constructive E-field interference between channels, since the ideally tuned simulation has higher nearest neighbor coupling compared to the realistically measured coupling. However, this trend does not hold for all drive settings. Figure 5 shows that pSAR10g can be underestimated by up to 20% in the worst case.

Conclusion

More accurate prediction of pSAR10g is necessary to reduce the conservative power limitations on pTx arrays for high-field MRI. Here a method was presented to help reduce the unknowns in pTx array simulation through direct measurement of the S-matrix with the loaded array in-situ. The simulation was forced to have the same coupling as the measurement by adapting the cost function of the optimization routine that is part of network co-simulation framework. Results support the fact that coupling significantly influences pSAR10g prediction. This method also appears to better estimate the physical EM field distribution based on B1+ mapping.

References

1. Röschmann P. Radiofrequency penetration and absorption in the human body: limitations to high-field whole-body nuclear magnetic resonance imaging. *Medical physics*. 1987;14(6):922–31.
2. Ibrahim TS, Lee R, Abduljalil AM, Baertlein BA, Robitaille PM. Dielectric resonances and B(1) field inhomogeneity in UHFMRI: computational analysis and experimental findings. *Magnetic resonance imaging*. 2001;19(2):219–26.
3. Hoult DI, Phil D. Sensitivity and power deposition in a high-field imaging experiment. *Journal of magnetic resonance imaging : JMRI*. 2000;12(1):46–67.
4. Padormo F, Beqiri A, Hajnal J V, Malik SJ. Parallel transmission for ultrahigh-field imaging. *NMR in biomedicine*. 2015 May 19 [accessed 2015 Nov 24].
5. Bottomley PA, Andrew ER. RF magnetic field penetration, phase shift and power dissipation in biological tissue: implications for NMR imaging. *Physics in medicine and biology*. 1978;23:630–643.
6. International T, Commission E, Iec T. IEC 60601-2-33 Safety Standard for MR Systems : Third Edition Hans Engels Philips Medical Systems , The Netherlands.
7. Center for Devices and Radiologic Health. Guidance for the submission of premarket notifications for magnetic resonance diagnostic devices. Rockville: Food and Drug Administration; 1988.
8. Wang Z, Lin JC, Mao W, Liu W, Smith MB, Collins CM. SAR and temperature: simulations and comparison to regulatory limits for MRI. *Journal of magnetic resonance imaging : JMRI*. 2007;26(2):437–41.
9. Zhu Y, Alon L, Deniz CM, Brown R, Sodickson DK. System and SAR characterization in parallel RF transmission. *Magnetic resonance in medicine*. 2012;67(5):1367–78.
10. Voigt T, Homann H, Katscher U, Doessel O. Patient-individual local SAR determination: in vivo measurements and numerical validation. *Magnetic resonance in medicine*. 2012;68(4):1117–26.
11. Alon L, Deniz CM, Brown R, Sodickson DK, Zhu Y. Method for in situ characterization of radiofrequency heating in parallel transmit MRI. *Magnetic resonance in medicine*. 2013;69(5):1457–65.
12. Christ A, Kainz W, Hahn EG, Honegger K, Zefferer M, Neufeld E, Rascher W, Janka R, Bautz W, Chen J, et al. The Virtual Family--development of surface-based anatomical models of two adults and two children for dosimetric simulations. *Physics in medicine and biology*. 2010;55(2):N23–38.
13. Dimbylow PJ. Fine resolution calculations of SAR in the human body for frequencies up to 3 GHz. *Physics in medicine and biology*. 2002;47:2835–2846.

Improving pSAR10g Prediction using In-situ S-matrix Measurements

14. Murbach M, Neufeld E, Kainz W, Pruessmann KP, Kuster N. Whole-body and local RF absorption in human models as a function of anatomy and position within 1.5T MR body coil. *Magnetic Resonance in Medicine*. 2014;71(2):839–845.
15. de Greef M, Ipek O, Raaijmakers AJE, Crezee J, van den Berg C a T. Specific absorption rate intersubject variability in 7T parallel transmit MRI of the head. *Magnetic resonance in medicine*. 2013;69(5):1476–85.
16. Homann H, Börner P, Eggers H, Nehrke K, Dössel O, Graesslin I. Toward individualized SAR models and in vivo validation. *Magnetic resonance in medicine*. 2011;66(6):1767–76.
17. Jin J, Liu F, Weber E, Crozier S. Improving SAR estimations in MRI using subject-specific models. *Physics in medicine and biology*. 2012;57(24):8153–71.
18. Hoffmann J, Henning A, Giapitzakis IA, Scheffler K, Shajan G, Pohmann R, Avdievich NI. Safety testing and operational procedures for self-developed radiofrequency coils. *NMR in biomedicine*. 2015 Apr 6 [accessed 2016 Feb 4].
19. Bitz AK, Kraff O, Orzada S, Maderwald S, Brote I, Johst S, Ladd ME. Assessment of RF Safety of Transmit Coils at 7 Tesla by Experimental and Numerical Procedures. *Proc. ISMRM* 19. 2011;490.
20. Ludwig R, Bretchko P. *RF Circuit Design: Theory & Applications* (2nd Edition). 2007 Jun 1
21. Weidemann G, Seifert F, Hoffmann W, Seemann R, Waxmann P, Ittermann and B. *Proc. ISMRM* 23. 2015;1775.
22. Kozlov M, Turner R. Fast MRI coil analysis based on 3-D electromagnetic and RF circuit co-simulation. *Journal of magnetic resonance*. 2009;200(1):147–52.
23. Beqiri A, Hand JW, Hajnal J V, Malik SJ. Comparison between simulated decoupling regimes for specific absorption rate prediction in parallel transmit MRI. *Magnetic resonance in medicine*. 2014 Nov 3 [accessed 2015 Aug 4].
24. Kozlov M, Turner R. RF transmit performance comparison for several MRI head arrays at 300MHz. In: *Microwave Conference (EuMC), 2013 European*. 2013. p. 601–604.
25. Kraff O, Fischer A, Nagel AM, Mönninghoff C, Ladd ME. MRI at 7 Tesla and above: demonstrated and potential capabilities. *Journal of magnetic resonance imaging: JMRI*. 2015;41(1):13–33.
26. Malik SJ, Keihaninejad S, Hammers A, Hajnal J V. Tailored excitation in 3D with spiral nonselective (SPINS) RF pulses. *Magnetic resonance in medicine*. 2012;67(5):1303–15.
27. Yarnykh VL. Actual flip-angle imaging in the pulsed steady state: a method for rapid three-dimensional mapping of the transmitted radiofrequency field. *Magnetic resonance in medicine*. 2007;57(1):192–200.

Improving pSAR10g Prediction using In-situ S-matrix Measurements

28. Oliphant TE. Python for Scientific Computing. *Computing in Science & Engineering*. 2007;9(3):10–20.
29. Graesslin I, Homann H, Biederer S, Börnert P, Nehrke K, Vernickel P, Mens G, Harvey P, Katscher U. A specific absorption rate prediction concept for parallel transmission MR. *Magnetic resonance in medicine*. 2012;68(5):1664–74.
30. Oh S, Webb AG, Neuberger T, Park B, Collins CM. Experimental and numerical assessment of MRI-induced temperature change and SAR distributions in phantoms and in vivo. *Magnetic resonance in medicine*. 2010;63(1):218–23.

Chapter 4

A Novel Approach to Real-time Local SAR Monitoring for Parallel Transmit MRI at 7T using Directional Couplers

Matthew Restivo, Alexander Raaijmakers, Christian Findeklee, Giel Mens, Wim Prins, Cornelis van den Berg, Peter Luijten, and Hans Hoogduin

Abstract

Purpose: Local SAR monitoring during parallel transmit MRI requires scaling numerical simulations by known or measured values that describe the RF waveform. Directional couplers provide a simple solution to monitor the forward and backward RF power levels and phases. However, previously derived methods for local SAR monitoring using directional couplers require complex simulation to ensure proper handling of array coupling. We propose a new solution using directional couplers to estimate the RF current on each transmit element, allowing the simulations to be greatly simplified.

Methods: The RF current on each transmit element is derived using circuit analysis and the known circuit topology of a loop coil from forward and backward directional coupler measurements. The method is tested using a 4 element loop coil head array at 7T to compare predicted and measured field distributions.

Results: Using this method, we are able to obtain B1+ field map predictions that appear similar to acquired B1+ maps in a phantom. The proposed method outperforms the method of scaling by delivered power.

Conclusion: The method presented can be used to estimate RF currents using directional couplers allowing for simplified local SAR monitoring. However, this method is limited to certain array configurations and circuit topologies.

Introduction

Human subjects undergoing an MR exam are exposed to RF energy that can potentially lead to tissue heating.¹ In order to prevent excessive heating, safety limits are in place to restrict the allowable specific absorption rate (SAR) in body tissue during RF transmission.^{2,3} At ultra-high field strength, it is standard practice to adhere to the SAR guidelines for local transmit coils which define limits on the local SAR distribution. This creates the need to either be able to assess the local SAR distribution delivered to the subject prior to scanning or reliably monitor the local SAR distribution during the scan.

Because the SAR field arises from the electric fields, it cannot be directly probed using MRI. Methods for estimating the SAR distribution using the RF excitation magnetic field, which can be measured in-vivo using B1+ mapping, are not yet reliable enough to be used for safety monitoring.^{4,5} Alternatively, measuring heating directly using MR thermometry is not sensitive enough in humans to detect the small temperature rises which may lead to safety concerns (~1 degree Celcius).^{6,7} Both B1+ mapping and MR thermometry are additionally not practical because local SAR hotspots may likely occur outside the FOV of the system. Therefore, numerically simulating the EM field using computer models for the RF coil and realistic human anatomies has become standard practice for estimating the SAR field. However, numerical simulations are slow and typically require hours to run, even with advanced acceleration techniques. For conventional single channel RF coils, the time requirement is not limiting. These coils, like a quadrature birdcage, always produce the same EM field (assuming the same subject model) scaled by the amplitude of the delivered power. Numerical simulations become increasingly complicated by the use of parallel transmit (pTx) systems. Each transmit element of a pTx array can be driven with independent amplitude and phase settings leading to an infinite number of plausible drive configurations that cannot be simulated ahead of time. Each drive configuration may result in a different EM field distribution, which in turn results in a different prediction for the peak local SAR value (pSAR) used for making RF safety decisions. It is not feasible to simulate each particular drive configuration prior to scanning.

One solution is to determine the worst case drive configuration that will result in the highest pSAR value anywhere in the body, and then limit the power available to the pTx array based on this conservative value.^{8,9} Limiting an RF array based on worst case pSAR is not ideal since this value tends to be much higher than the pSAR generated by the coil under most normal operating drive configurations. A

better solution is to recognize that independent Tx elements generate EM field distributions that add linearly. Using this superpositioning concept, any drive configuration of a pTx array with N-channels can be determined by only N simulations. The SAR of any voxel in the simulation domain can then be computed by reducing the per channel SAR contribution for each of the N-channels to an N-by-N matrix as described in Ref. (10). The per voxel SAR resulting from any drive configuration at time point (t) during the RF pulse can be calculated by equation:

$$SAR(x, t) = I(t)^* Q(x) I(t) \quad [1]$$

Where Q is the N-by-N SAR matrix, also called a Q-matrix, and $I(t)$ is a N-by-1 vector that describes the complex valued drive of each channel during any time point in the RF waveform. (I^* describes the complex conjugate transpose of the drive vector.) Using this equation local SAR can be predicted prior to scanning or even monitored in real-time during a MR scan using numerical simulations, given that the drive vector $I(t)$ is known. To reduce the computational burden, the number of matrices that has to be evaluated can be reduced using virtual observation points (VOPs).¹¹

In practice, it is difficult to determine the complex driving weights ($I(t)$ in Eq. [1]) for each channel. Graesslin et al.¹⁰ define $I(t)$ as a vector combining all the complex electric current values of the transmit elements. It is known from Maxwell's equations that the EM field produced by a current in a wire scales linearly with the amplitude and phase of the current. Electric current in the transmit array can be measured using current-sensing pickup probes. Pickup probes placed very close to the transmit elements detect magnetic flux, which can be related to the complex current value through calibration.¹² This has been shown to work well at 3T when incorporated into a fixed pTx body coil inside the scanner bore.¹³ However, pickup probes do not work well for local transmit arrays because a one-time calibration of these probes is not representative for each placement of the array on the patient. The calibration may be sensitive to changes in array placement or movement of the transmission line cables feeding the array. For example, the high power transmission line signal can be many orders of magnitude larger than the pickup probe signal, thus low levels of cross-cable coupling can severely distort the measurements.

Directional couplers, integrated into the transmission lines of each amplifier channel, split the RF signal into its forward and backward components. Once calibrated, directional couplers provide robust RF waveform and power

measurements. They are already implemented in many systems for real-time global SAR monitoring.¹⁴ Given that electric current on the channel is related to forward and backward signals, directional couplers can also be used to measure the exact currents on the transmit elements which is essential for local SAR determination. Using the square root of the measured power alone to scale simulations is a problem because the phase information is lost. A better solution is to use the measured forward signal amplitude and phase (equal to the square root of the forward power). However, this requires that the impedance seen at the output of each channel is modeled realistically. This can be done in practice by ensuring simulated scattering parameters to match that of the physical array setup.^{15–17} If scattering is modeled properly in the simulations, then the field distributions are estimated by a linear combination scaled by the square roots of the forward power and phases of the forward signals.

In this work we explore an alternative approach to local SAR monitoring that uses directional couplers for current sensing. Current sensing should be possible given that electric current is related to the forward and backward RF signals sampled by the directional couplers. The advantage of using currents is that it simplifies the simulation setup considerably by allowing inter-element coupling to be ignored, as presented in SAR monitoring solutions with pickup probes (Ref. ¹²). However, this method would be preferred over using pickup probes given the challenges associated with pickup probe calibration and since directional couplers are already commonly implemented in pTx systems at ultrahigh field with local transmit arrays.

Theory and Methods

Transmission Chain and Directional Coupler Description

Transmission lines carry the RF waveform from the amplifiers to the transmit array, typically in the form of long coax cables. Signals propagate along these transmission lines in both directions: forward and backward. In transmission line theory¹⁸, waves can conveniently be described by their forward and backward components, a and b respectively. These wave variables are related to the current (I) and voltage (V) at a particular point in the transmission line, as described in Eqs. 2 & 3, where Z_0 is the characteristic impedance of the transmission line (typically 50 Ohm).

$$a = \frac{1}{2} \left(\frac{V}{\sqrt{Z_0}} + \sqrt{Z_0} I \right) \quad [2]$$

$$b = \frac{1}{2} \left(\frac{V}{\sqrt{Z_0}} - \sqrt{Z_0} I \right) \quad [3]$$

Note that in these equations voltage and current are denoted by their effective phasors. Directional couplers are devices that couple out small fractions of forward and backward wave such that they depend linearly of the traveling wave amplitudes. The coupled signal amplitude and phase measured by the directional couplers can be conveniently related to the wave variables \mathbf{a} and \mathbf{b} through a calibration step.¹⁹ The calibration requires measuring the power levels at the end of the (matched) transmission lines with a power meter, a corresponding phase measurement, and measurements under certain (at least three) well-defined conditions (i.e. open, short, and match, typically given by 50 Ohm termination). After calibration, the measured directional coupler signals relate directly to wave variables at the end of the transmission line (rather than the point in the line where the couplers are placed). The shifted reference plane for the directional coupler measurements is defined as the coil connection plane (CCP). A diagram of the transmit chain is illustrated in Fig 1.

Also shown in Fig. 1, is the importance of the matching network in the transmit path. Matching networks are used to transform the impedance of the transmit element to match the characteristic impedance of the feeding transmission line. This leads to optimal power transfer from the transmission line to the load. However, typically the matching network provides an alternative pathway for current on the line to travel instead of following the main conductor of the transmit element. The effect is that even after calibration, the current at the end of the line is not equal to the current on the transmit element. Therefore, for local SAR monitoring with directional couplers, it is necessary to come up with a derivation for the current on the transmit element that takes into account the effect of the matching network.

Circuit Model for a RF Transmit Coil

The effect of the matching network on the current transformation is better illustrated by looking at an RF element as an electrical circuit. In general, a loop coil for MRI applications is a simple LC circuit made from a closed-loop conductor tuned to the resonant frequency for MRI by series capacitors, as

shown in Fig. 2a. A matching network is added to transform the impedance of the loop coil to 50 Ohm at the desired operating frequency.

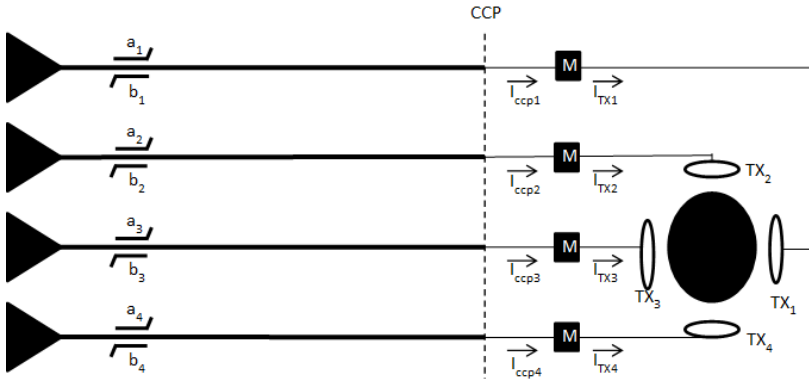


Figure 1: Simplified illustration of the transmission path for a four channel pTx array of loop coils. The triangles represent the RF amplifiers that generate the signal on the transmission lines (thick black lines). The directional couplers are integrated into the transmission path, measuring the forward (a) and backward (b) signals and feeding the lines back into receivers (not shown) for measurements. The junction of the transmission cables with the individual array elements is referred to as the coil connection plane (CCP). The current at the CCP is affected by the matching network (M) before feeding the individual transmit (TX) elements.

The entire coil can be represented as a circuit consisting of different lumped impedances. The total coil impedance is a function of fixed impedances (i.e. lumped elements, wire inductance, and copper resistance) and variable impedances caused by the loading to the body as well as inductive coupling from current in other elements. The variable component contributes to the problem that the total impedance of a particular element will not be consistent over time, as the position relative to the subject and drive configuration may change. However, many loop coils have matching networks that consist of a lumped element in parallel with the feeding transmission line. This provides an alternate path for the current to travel, and must be represented separately in the coil model, as shown in Fig. 2b. Given that this circuit branch is very small in size compared to the main loop conductor, it is assumed that the impedance of this segment will not be sensitive to loading and coupling.

The purpose of the circuit model is to come up with a robust estimation of element current using only variables that are either easily measurable or fixed. Using the model derived in Fig. 2b, the transmit element current (I_{loop}) can be derived through Kirchhoff's current law, as the difference between the source current (I_{CCP}) and the current through the parallel component of the matching network ($I_{matching}$). The current through the parallel component of the matching

network is derived given that we expect the impedance of this circuit segment (Z_{matching}) to be constant.

$$I_{\text{loop}} = I_{\text{CCP}} - I_{\text{matching}} = I_{\text{CCP}} - \frac{V_{\text{CCP}}}{Z_{\text{matching}}} \quad [4]$$

I_{ccp} and V_{ccp} can be determined from the directional coupler measurements through the definition of \mathbf{a} and \mathbf{b} shown in Eqs. 2 & 3, then solving for I and V.

$$I_{\text{CCP}} = \frac{a - b}{\sqrt{Z_0}} \quad [5]$$

$$V_{\text{CCP}} = \sqrt{Z_0}(a + b) \quad [6]$$

The importance of Z_{matching} is clear from Eq.4. Determination of this impedance is a crucial part of the proposed method and is described later in this section.

It should be noted here that since MRI deals with RF frequencies, the above equations only hold if the size of the circuit segments is small in relation to the RF wavelength. This is certainly true for the loop coil used in this study since the size of the parallel component of the matching network is only a couple of centimeters. The loop current is defined at a location in the conductor immediately after the matching network, thus the current feeding the loop can be known from the above equations. Any variation in current amplitude and phase over the conductor should be accurately reflected in simulations.

Hardware

The concept was tested using a Philips 7T MR scanner (Utrecht, Netherlands). Directional couplers were installed on eight transmission lines coming from 8 x 2 kW amplifiers. A calibration step was performed on each channel to relate the signals measured by the directional couplers to the coil-connection-plane wave amplitudes a_{ccp} and b_{ccp} with units \sqrt{W} . This calibration used well defined open, short, and 50 ohm connections at the end of the transmission line cables. These measurements were used to calibrate out the line reflections in the transmission chain and attenuation over the length of the cable. Measurements were also performed with a power meter connected to the end of the transmission chain (i.e. CCP) to convert raw directional coupler samples to \sqrt{W} . Finally, the transmission lines were fed back into the same test receiver to calibrate the relative phase of each amplifier.

prototype four-channel head transmit array was constructed (for testing), from individual rectangular loop elements shown in Fig 3A. The elements (11.5 cm wide by 21 cm long) were secured onto a plastic cylindrical shell that provided the structure of the array. The array was shielded by an aluminum foil shell that fits around the plastic structure. The four elements were placed in 90 degree increments providing for complete coverage around the load. For this experiment we used a load consisting of a 10 cm diameter, fluid-filled spherical phantom. The dielectric properties of the fluid was measured to have an electrical conductivity (σ) equal to 1.0 S/m and a relative permittivity (ϵ_r) of approximately 80 (same as distilled water). A model of the full array with the load is shown in Fig. 3c.

Parallel Matching Network Impedance

The parallel component of the matching network impedance was measured during coil construction on the bench using a network analyzer. For the coil under test, the component is just a single capacitor which can be seen at the bottom of Fig. 3a. The impedance of each transmit element was first measured without the capacitor in place. The capacitor was then soldered into the circuit, and the impedance of each transmit element was measured again. The two measurements were used to calculate the effective value of $Z_{matching}$. This two-measurement method was used so that the impedance could be determined with the capacitor in place.

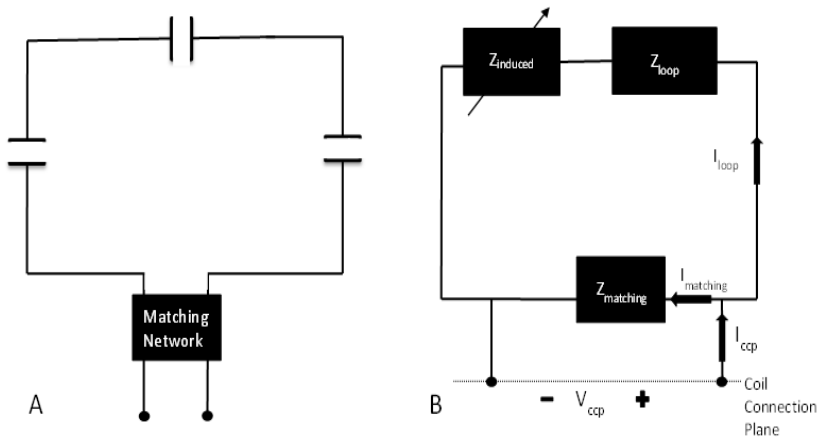


Figure 2: (A) Diagram of a typical loop coil used for excitation in MRI. The element generally consists of a resonant loop matched to the characteristic impedance of the transmission line by a matching network. (B) A circuit analysis model for a loop coil that is used to derive an equation for the current in the main loop conductor. This model highlights the two current paths and three relevant lumped impedances. One current path is the one along the main conductor and is responsible for EM field generation. The other leg is the current path through the parallel component of the matching network. The matching network may also have a serial component which is included in Z_{loop} . The dimensions of the $Z_{matching}$ path are very small compared to the main conductor path and therefore it does not see a significant effect of loading. Z_{loop} and $Z_{matching}$ are impedances from fixed

components while Z_{load} is due to the loading of the coil by the subject or object being imaged, and thus is variable (symbolically illustrated by a through arrow similar to the representation of a potentiometer). The dotted line illustrates the coil connection plane (CCP) which is where the coil connects to the transmission line. It is also the point to which the directional couplers are calibrated, as well as the point where the source is connected in simulation.

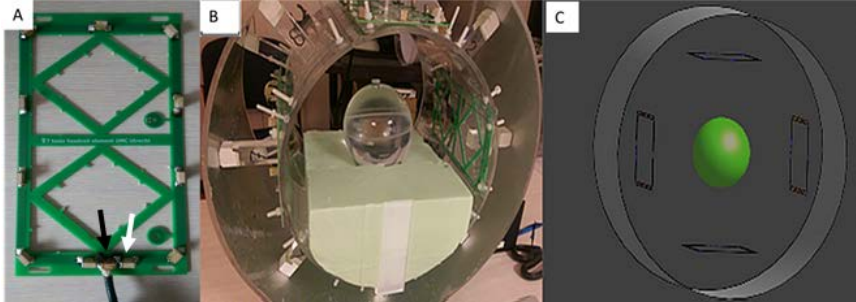


Figure 3: (A) Photo of one of the individual loop elements used. The black arrow shows the location of the capacitor used for matching which is in parallel with the source. The white arrow shows to the location where the current is measured in the simulation domain. (B) Photo of the 4-ch array loaded with the spherical phantom used for testing. (C) The computer model of the array setup used for numerical simulation.

Simulations

Simulations were performed using Sim4Life (ZMT AG, Zurich, CH). The array was modeled by four identical loop elements with the same geometric shape and size as the physical loop elements used for imaging, including gaps for capacitors and matching network. The shield around the array elements and the spherical phantom were included to replicate the setup of the MR experiment. FDTD simulations were performed using a grid consisting of 2.6 million cells. Voxelized resolution in the phantom is less than 2 mm in the transverse directions and 5 mm in the longitudinal direction. The loop elements were driven by 298 MHz harmonic voltage sources with a simulation time of 100 periods to ensure the convergence to steady-state given the high-Q nature of a resonant loop coil. Convergence was checked by visually verifying that steady-state was reached, as well as making sure the power balance (dissipated + radiated power / input power) was close to 1 (within +/- 3%).

Four separate simulations were needed for the Q-matrix SAR formulation. The four simulations were performed in an ideally decoupled way. This means that for each simulation, the loop element containing the active source was tuned and matched for resonance at 298 MHz. The capacitors in the three remaining loops were replaced by large impedances (1 k Ω) to ensure virtually no current is generated in these loops through RF coupling. The sources in the inactive loops were simulated as 50 ohm impedances. The simulations were normalized to

current in the loop of the active element. Current was measured by a sensor placed at the location of the first series capacitor going counter clockwise around the element starting at the source (highlighted by the white arrow in Fig. 3A).

Image Acquisition

MR imaging was performed to acquire B1+ measurements of the setup described above. These B1+ measurements were compared to the predicted B1+ field distributions based on simulated single-channel B1+ maps and current measurements. Measured B1+ distributions were determined using low flip angle gradient echo (low FA GE) images because of better dynamic range in comparison to other B1+ mapping techniques.²⁰ A 1° flip angle was used to ensure that the low tip-angle approximation is valid such that low FA GE signal intensity is proportional to B1+ (i.e. below the Ernst angle of approximately 25° for the 500 ms T1 of the phantom and a 50 ms TR). B1- magnitude was divided out after determining B1- as the ratio of a 3D quadrature Actual Flip Angle (AFI) B1+ map²¹ and quadrature low FA GE image. The 3D quadrature AFI B1+ map acquisition used a flip angle of 50° (TR1 = 40 ms, TR2 = 200 ms). Low FA GE and AFI B1+ map images are acquired with 1x1x5 mm resolution for a grid size of 128x128x7. Low FA GE images were acquired using five different drive configurations (shown in Table 2) for comparison of B1+ maps.

Scaling and B1+ Field Prediction

Directional coupler signals were sampled during the RF pulse on all four channels. For each image, the corresponding forward and reflected directional coupler signals were used to estimate loop element current on each channel, as described in Eq. 4-6. Each of the four simulations corresponding to individual ideally decoupled elements were scaled according to the estimated current and summed to produce the predicted field distribution.

Results

The measured values for $Z_{matching}$ are shown in Table 1. The capacitor in the physical loop elements used for matching (highlighted with a black arrow in Fig. 3A) has a value of 16 pF which equates to an impedance of about -33i Ohms. The measurements are all very close to this value with deviation caused by tolerance of the capacitor, the resistance of the solder joints, and small inductive component of the wire segment and the capacitor itself.

| Table 1 | Coil 1 | Coil 2 | Coil 3 | Coil 4 |
|------------------------|-----------|-----------|-----------|-----------|
| Impedance (Ω) | 1.4-28.0i | 1.1-30.7i | 0.9-27.1i | 0.5-30.1i |

Samples taken from the directional couplers yielded reliable measurements for the forward and backward RF waveform. An example of this is shown in Fig. 4 which shows the directional couplers samples over one RF waveform during quadrature drive. The waveform is correctly captured and the peak value of .25 W per channel matches with what was expected for the B1+ requested by the scanner. The requested drive settings and the directional coupler measurements at the peak of the RF waveform of the five drive settings used are listed in Table 2.

To test the method, pTx MRI experiments were performed with the array driven in five different drive configurations. Converting the directional coupler measurements to a current waveform was done using Eqs. 4-6. The per channel current waveform determined from quadrature drive is shown in Fig. 5. The resulting predicted B1+ field distributions for quadrature and the other drive settings from table 2 are shown in Fig. 6 and compared to the measured distributions. Predicted B1+ field distributions using delivered power (i.e. forward minus backward power) are also shown in the comparison. Results clearly show that the predicated field distributions using the proposed method are more accurate. This demonstrates that delivered power scaling is insufficient for predicting field distributions using arrays where coupling cannot be neglected.

Discussion

Transmit element current sensing in multi-channel RF excitation is important for predicting EM field distributions with simulated field data without having to be concerned about array coupling. The practicality of this work is that it can be used for real-time local SAR monitoring using the Q-matrix formalism described in Eq. 1. Using directional couplers for current sensing would be an improvement over pick-up probes due to the difficulty in including pick-up probe measurements for local transmit arrays. The results from this work provide evidence that current sensing is possible using directional couplers, however, there are still some limitations to this method.

The results shown in Fig. 6 demonstrate that transmit element current amplitude and phase is being approximated well using the directional couplers and the derivation in Eq. 4. The B1+ predicted using the directional coupler measurements matches reasonably well to the measured distributions. This

method dramatically outperforms the method of scaling the fields by delivered power – a common technique that works for well-decoupled arrays, but not when non-trivial levels of array coupling are present. Still, some discrepancies between the measured and predicted field distributions exist also for the current sensing method.

The proposed method is applicable for providing correct SAR predictions for pTx arrays. In this work, the method is used predominantly to predict B1+ distributions because of validation purposes. The B1+ distributions are the only component of the RF transmit field that is easily measurable with MRI. Some works have shown that B1+ is not a good estimator of local SAR because the electric field is more heavily influenced by anatomical variations, and thus B1+ distributions can look the same for two different models while they have very different peak local SAR.²² However, in a homogenous spherical phantom with no anatomical variation, an accurately simulated B1+ field implies that the simulated electric field is also correct. When predicting local SAR in a human, it is necessary to have a highly accurate anatomical model. This is the subject of many other investigations and is not considered in this work.^{23–25}

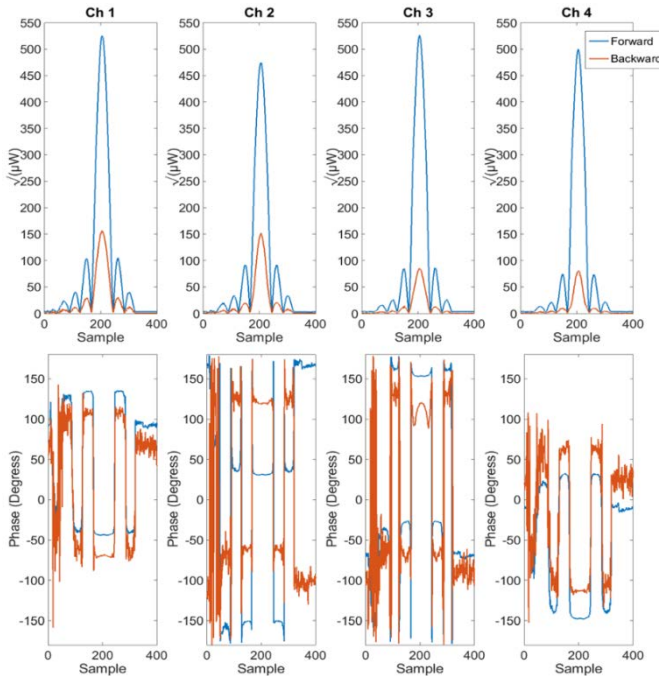


Figure 4: Directional coupler measurements on the four transmission lines calibrated to the coil connection plane displayed for drive 1 (quadrature drive). The directional couplers sample the

forward and backward signal magnitudes and phases over the sinc-like RF pulse. The phase of the forward signal on neighboring channels are approximately 90 degrees offset at the peak, as expected for quadrature drive. Phase measurements appear noisy at the beginning and end of the pulse where the magnitude is near zero.

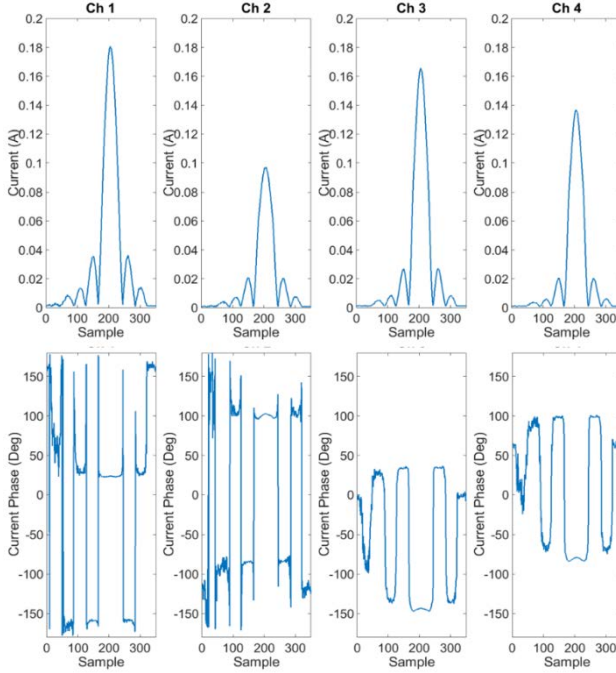


Figure 5: The current levels on each of the four elements derived using the forward and backward waveforms shown in Fig. 4 (Drive 1, i.e. quadrature drive).

The worst case peak local SAR can be analyzed from the largest eigenvalue of the Q-matrix domain. For the simulated four channel array and phantom setup, the worst case pSAR_{10g} comes out to be 4.48 W/Kg normalized to 1 A² of total current squared summed over each element. Note that current squared is proportional to power through the impedance, thus all randomly generated excitation vectors have approximately the same power although the overall impedance is also varying with the drive setting. Computing the pSAR_{10g} for 10000 excitation vectors with randomly generated relative amplitude and phase settings (normalized to 1 A² sum of current squared over all channels, Fig. 7) shows that the average pSAR_{10g} is 2.36 W/kg. This shows the benefit of using more accurate local SAR monitoring over assuming the worst case. Fig. 7 shows that assuming the worst case pSAR_{10g} overestimates the actual pSAR_{10g} on average by 120%.

This study analyzed the potential to use directional couplers for current sensing with only one kind of loop coil topology. However, the concept presented in the theory section is a basic circuit analysis technique that can be used for a variety of transmit elements and matching networks. This method specifically applies to coils using a matching circuitry consisting of impedances in parallel or series with the main loop conductor. The derivation presented in the theory section (specifically Eq. 4) does not hold when the matching network consists of elements that cannot be interpreted as being in parallel or series with the main conductor, such as a pi-network. However, it is possible that a similar derivation can be applied based on the equivalent circuit model for any specific network; i.e. it may require just a more general network description.

It is also important to consider that current normalization is only valid when ideal decoupling is simulated. Some coil geometries cannot be simulated in an ideally decoupled fashion due to the presence of capacitive or inductive decoupling networks between elements. When the transmit elements are directly linked through physical structures, the current pattern produced by a single channel is not confined to a single element. The limitations of ideally decoupled simulations compared to fully coupled coil models can be found in the work of Beqiri et al.²⁷ However, it should also be noted that simulating ideal decoupling is straight forward. The alternative to ideal decoupling is to simulate realistic scattering, which generally involves using network co-simulation²⁸ or very careful modeling^{16,17}. Network co-simulation requires that every lumped element in the circuit is simulated as a transmitting port.^{29,30} Therefore, the complexity of the simulations, with respect to computation time and data size, quickly scales up with the number of lumped elements in the array. Additionally, the Q-matrices can only be calculated after scattering parameters are measured and the co-simulation scattering is optimized to match. This takes time and limits the practicality of this method for scanning real subjects. While linked element pTx arrays can be made to exhibit very low coupling, non-linked type arrays might be preferable due to the simplicity of simulations and the applicable local SAR monitoring methods described in this work.

Conclusion

Directional couplers are already a common solution for global SAR monitoring as well as power monitoring in pTx systems. The extension to local SAR monitoring using this method only requires some additional knowledge about the matching network. This, theoretically, could be provided by the coil manufacturer. Using directional couplers for current monitoring is a powerful

solution to local SAR monitoring that is fundamentally straightforward and more practical to implement compared to techniques that require the scattering parameters to be accurately simulated. The results suggest that current sensing with directional couplers is possible.

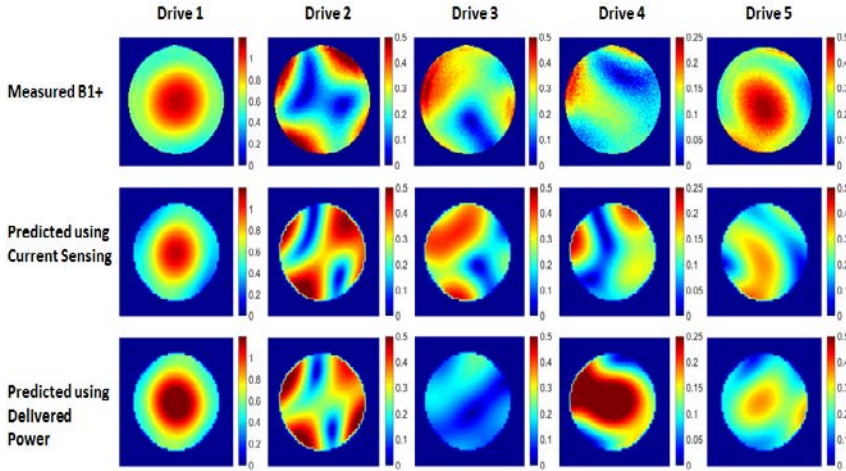


Figure 6: The first row shows the measured B1+ maps in a phantom at 7T using five different amplitude and phase combinations to drive a four channel pTx array. The specific drive settings are listed in Table 2. The second row shows the simulated B1+ patterns predicted using the method presented in this paper, which uses the directional coupler measurements to derive the electrical current on the four elements. The third row shows the B1+ pattern predicted when the simulations are scaled by the delivered power (forward minus reflected) measured by the directional couplers on each channel. All scales are in μT .

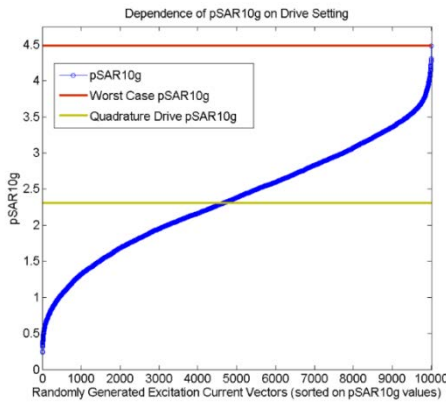


Figure 7: Worst case pSAR10g (red line) is determined by finding the largest eigenvalue of the set of 10g averaged Q-matrices. This corresponds to the highest attainable local SAR value when the sum of the square of the currents in each channel equals 1 A^2 . The blue line shows the pSAR10g values generated by 10000 randomly generated complex valued 4×1 vectors simulating the driving current in

Real-Time Local SAR Monitoring for pTx 7T MRI Using Directional Couplers

each channel, normalized so the sum of squares adds up to 1 A^2 (thus effectively having approximately equal power). The values are sorted in ascending order to show the span of local SAR values. The yellow line shows the pSAR10g generated by the quadrature drive. The purpose of this plot is to show that most drive settings produce pSAR10g levels much lower than the worst case. This includes efficient drive settings which will be more commonly used for high B1+ or optimal shimming, as shown by the quadrature case.

The absence of practically implementable local SAR monitoring is limiting the use of parallel transmit arrays in 7T MRI. Without local SAR monitoring, current approaches to local SAR management are based on worst case electric field interference which results in extremely conservative limits. Basing peak local SAR prediction on the actual measured amplitude and phase of the current on the transmit elements will yield more accurate local SAR predictions for pTx systems at 7T.

| | Requested Drive Settings | | | | Forward Power Measured by DiCos | | | | Backward Power Measured by DiCos | | | | |
|---------|--------------------------|-------|-------|-------|---------------------------------|-------|-------|-------|----------------------------------|-------|-------|-------|-------|
| | Ch 1 | Ch 2 | Ch 3 | Ch 4 | Ch 1 | Ch 2 | Ch 3 | Ch 4 | Ch 1 | Ch 2 | Ch 3 | Ch 4 | |
| Drive 1 | Power (W) | 0.250 | 0.250 | 0.250 | 0.250 | 0.263 | 0.237 | 0.263 | 0.250 | 0.078 | 0.076 | 0.042 | 0.040 |
| | Phase (Deg) | 0 | 90 | 180 | -90 | 0 | 87 | 178 | -92 | -26 | 176 | 143 | -58 |
| Drive 2 | Power (W) | 0.250 | 0.250 | 0.250 | 0.250 | 0.265 | 0.248 | 0.262 | 0.260 | 0.043 | 0.101 | 0.105 | 0.093 |
| | Phase (Deg) | 0 | -90 | 180 | 90 | 0 | -91 | -176 | 93 | -6 | 27 | 152 | 89 |
| Drive 3 | Power (W) | 0.250 | 0.250 | 0.250 | 0.250 | 0.254 | 0.230 | 0.261 | 0.240 | 0.218 | 0.196 | 0.187 | 0.217 |
| | Phase (Deg) | 0 | 90 | 0 | 90 | 0 | 95 | -1 | 97 | -143 | -178 | -169 | 144 |
| Drive 4 | Power (W) | 0.250 | 0.250 | 0.250 | 0.250 | 0.245 | 0.240 | 0.234 | 0.258 | 0.222 | 0.240 | 0.233 | 0.150 |
| | Phase (Deg) | 0 | 0 | 0 | 0 | 0 | -7 | -1 | 0 | 135 | 166 | 104 | 162 |
| Drive 5 | Power (W) | 0 | 0 | 0.250 | 0.250 | 0.015 | 0.012 | 0.238 | 0.254 | 0.143 | 0.114 | 0.119 | 0.033 |
| | Phase (Deg) | 0 | 0 | 180 | 180 | 0 | 74 | 172 | 173 | -51 | 3 | -106 | -12 |

Table 2. The requested drive settings (amplitude and phase) and the directional coupler values measured at the peak of the RF waveform for the five drive settings used for imaging. Phases are always denoted with respect to channel 1. Forward power measurements are very similar to the requested drive, as expected. Note that the phase measurements are not significant (and may be inaccurate) when the power amplitude of the signal is very low (ex. measured forward signal phase for Ch 2, Drive 5).

References

1. Bottomley PA, Andrew ER. RF magnetic field penetration, phase shift and power dissipation in biological tissue: implications for NMR imaging. *Physics in medicine and biology*. 1978;23:630–643.
2. International T, Commission E, Iec T. IEC 60601-2-33 Safety Standard for MR Systems : Third Edition Hans Engels Philips Medical Systems , The Netherlands.
3. FDA Guidelines for Magnetic Resonance Equipment Safety.
4. Voigt T, Heumann H, Katscher U, Doessel O. Patient-individual local SAR determination: In vivo measurements and numerical validation. *Magnetic Resonance in Medicine*. 2012;68:1117–1126.
5. Katscher U, Voigt T, Findelee C, Vernickel P, Nehrke K, Dössel O. Determination of electric conductivity and local SAR via B1 mapping. *IEEE transactions on medical imaging*. 2009;28(9):1365–1374.
6. Oh S, Webb AG, Neuberger T, Park B, Collins CM. Experimental and numerical assessment of MRI-induced temperature change and SAR distributions in phantoms and in vivo. *Magnetic resonance in medicine : official journal of the Society of Magnetic Resonance in Medicine / Society of Magnetic Resonance in Medicine*. 2010 [accessed 2014 Aug 25];63(1):218–23.
7. Alon L, Deniz CM, Brown R, Sodickson DK, Zhu Y. Method for in situ characterization of radiofrequency heating in parallel transmit MRI. *Magnetic resonance in medicine*. 2013 [accessed 2015 Nov 24];69(5):1457–65.
8. Ipek O, Raaijmakers AJ, Lagendijk JJ, Luijten PR, van den Berg CAT. Intersubject local SAR variation for 7T prostate MR imaging with an eight-channel single-side adapted dipole antenna array. *Magnetic resonance in medicine*. 2014 [accessed 2016 Mar 23];71(4):1559–67. <http://www.ncbi.nlm.nih.gov/pubmed/23754584>
9. Oezerdem C, Winter L, Graessl A, Paul K, Els A, Weinberger O, Rieger J, Kuehne A, Dieringer M, Hezel F, et al. 16-channel bow tie antenna transceiver array for cardiac MR at 7.0 tesla. *Magnetic resonance in medicine*. 2015 Jul 17 [accessed 2016 Mar 24].
10. Graesslin I, Homann H, Biederer S, Börner P, Nehrke K, Vernickel P, Mens G, Harvey P, Katscher U. A specific absorption rate prediction concept for parallel transmission MR. *Magnetic resonance in medicine*. 2012 [accessed 2015 Aug 4];68(5):1664–74.
11. Eichfelder G, Gebhardt M. Local specific absorption rate control for parallel transmission by virtual observation points. *Magnetic Resonance in Medicine*. 2011 [accessed 2014 Aug 25];66(5):1468–1476.

12. Graesslin I, Vernickel P, Börner P, Nehrke K, Mens G, Harvey P, Katscher U. Comprehensive RF safety concept for parallel transmission MR. *Magnetic resonance in medicine*. 2015 [accessed 2016 Aug 15];74(2):589–98.
13. Vernickel P, Röschmann P, Findekle C, Lüdeke K-M, Leussler C, Overweg J, Katscher U, Grässlin I, Schünemann K. Eight-channel transmit/receive body MRI coil at 3T. *Magnetic Resonance in Medicine*. 2007 [accessed 2016 Aug 15];58(2):381–389.
14. Zhu Y, Alon L, Deniz CM, Brown R, Sodickson DK. System and SAR characterization in parallel RF transmission. *Magnetic resonance in medicine*. 2012 [accessed 2014 Aug 25];67(5):1367–78.
15. Restivo MC, van den Berg CAT, van Lier ALHMMW, Polders DL, Raaijmakers AJE, Luijten PR, Hoogduin H. Local specific absorption rate in brain tumors at 7 tesla. *Magnetic resonance in medicine*. 2015 Mar 5 [accessed 2015 Aug 4].
16. Bitz AK, Kraff O, Orzada S, Maderwald S, Brote I, Johst S, Ladd ME. Assessment of RF Safety of Transmit Coils at 7 Tesla by Experimental and Numerical Procedures. *Ismrm*. 2011;16(2008):1.
17. Hoffmann J, Henning A, Giapitzakis IA, Scheffler K, Shajan G, Pohmann R, Avdievich NI. Safety testing and operational procedures for self-developed radiofrequency coils. *NMR in biomedicine*. 2015
18. Ludwig R, Bretchko P. *RF Circuit Design: Theory & Applications (2nd Edition)*. 2007 Jun 1 [accessed 2015 Aug 6].
19. Padormo F, Beqiri A, Malik SJ, Hajnal J V. RF system calibration for global Q matrix determination. *Magnetic Resonance Imaging*. 2016;34(5):690–693.
20. Malik SJ, Keihaninejad S, Hammers A, Hajnal J V. Tailored excitation in 3D with spiral nonselective (SPINS) RF pulses. *Magnetic resonance in medicine*. 2012 [accessed 2015 Aug 4];67(5):1303–15.
21. Yarnykh VL. Actual flip-angle imaging in the pulsed steady state: a method for rapid three-dimensional mapping of the transmitted radiofrequency field. *Magnetic resonance in medicine*. 2007 [accessed 2015 Nov 11];57(1):192–200.
22. Alon L, Deniz CM, Carluccio G, Brown R, Sodickson DK, Collins CM. Effects of Anatomical Differences on Electromagnetic Fields, SAR, and Temperature Change. Concepts in magnetic resonance. Part B, *Magnetic resonance engineering*. 2016 [accessed 2016 Aug 15];46(1):8–18.
23. Christ A, Kainz W, Hahn EG, Honegger K, Zefferer M, Neufeld E, Rascher W, Janka R, Bautz W, Chen J, et al. The Virtual Family—development of surface-based anatomical models of two adults and two children for dosimetric simulations. *Physics in medicine and biology*. 2010 [accessed 2014 Jul 23];55(2):N23–38.

24. Alon L, Cloos M, Assaf T, Sodickson DK, Collins CM. Subject Specific Body Model Creation using MR Fingerprinting. *Proc. Intl. Soc. Mag. Reson. Med.* 23. 2015 [accessed 2015 Nov 24]:0299.
25. Homann H, Börner P, Eggers H, Nehrke K, Dössel O, Graesslin I. Toward individualized SAR models and in vivo validation. *Magnetic resonance in medicine.* 2011 [accessed 2015 Aug 4];66(6):1767–76.
26. De Greef M, Ipek O, Raaijmakers AJE, Crezee J, van den Berg C a T. Specific absorption rate intersubject variability in 7T parallel transmit MRI of the head. *Magnetic resonance in medicine : official journal of the Society of Magnetic Resonance in Medicine / Society of Magnetic Resonance in Medicine.* 2013 [accessed 2014 Aug 25];69(5):1476–85.
27. Beqiri A, Hand JW, Hajnal J V, Malik SJ. Comparison between simulated decoupling regimes for specific absorption rate prediction in parallel transmit MRI. *Magnetic resonance in medicine.* 2014 Nov 3 [accessed 2015 Aug 4].
28. Restivo M, Raaijmakers A, van den Berg C, Luijten P, Hoogduin H. Improving peak local SAR prediction in parallel transmit using in situ *S*-matrix measurements. *Magnetic resonance in medicine.* 2016 May 13
29. Kozlov M, Turner R. Fast MRI coil analysis based on 3-D electromagnetic and RF circuit co-simulation. *Journal of magnetic resonance (San Diego, Calif. : 1997).* 2009 [accessed 2015 Apr 17];200(1):147–52.
30. Kozlov M, Turner R. RF transmit performance comparison for several MRI head arrays at 300MHz. In: *Microwave Conference (EuMC), 2013 European.* 2013. p. 601–604.

Chapter 5

Advantages of Local Transmit for Prostate Imaging at 3T using an 8-Channel Parallel Transmit Array of Meandering Dipoles Compared to the Conventional Body Coil

Matthew Restivo, Hans Hoogduin, Shaihan Malik, Arian Beqiri, Francesco Padormo, Aidin Ali Haghnejad, Cornelis van den Berg, Dennis Klomp, Peter Luijten, Joseph Hajnal, and Alexander Raaijmakers

Abstract

Purpose: The standard 3T birdcage body coil is not very efficient with respect to power in generating the desired radiofrequency fields (B_1^+) for body imaging. Local transmit arrays are typically more efficient given the proximity of the RF elements to the imaged anatomy. The potential for lower global/local power deposition (SAR) and improved B_1^+ field homogeneity using local transmit for 3T body imaging is examined.

Methods: An eight-channel meandering dipole local transceive array was built for a 3T system with multi-transmit capabilities. FDTD simulations were used to compare theoretical whole-body and local SAR performance. B_1^+ maps and 2D-TSE images of the prostate were acquired in-vivo on four subjects.

Results: Simulations confirmed a 70% increase in B_1^+ per unit power and similar peak local SAR (pSAR10g) efficiency using the local array compared to the body coil. The acquired images show that good B_1^+ intensity and homogeneity can be achieved at depth in the body while ensuring RF safety.

Conclusion: Simulation and imaging results show that the use of local transmit arrays for 3T body imaging is a promising approach to reduce required RF power and, thereby, relax global SAR related imaging constraints.

Introduction

Diagnostic imaging of the head, neck and extremities is often performed on 3T MRI systems due to the improved signal to noise (SNR) relative to 1.5T. However, body imaging at 3T suffers from the fact that the radio frequency (RF) wavelength in tissue becomes shorter than the width of the human body. This can lead to RF excitation profile inhomogeneity, resulting in variable contrast and, in extreme cases, even signal voids in the image.^{1,2} State of the art 3T MRI scanners use a two-port birdcage-type body coil integrated into the scanner bore for RF excitation. The advantage of the two-port body coil is that B_1^+ homogeneity can be further improved in a particular region of interest (ROI) by varying the phase and amplitude relationship between the driving ports (RF shimming).^{3,4} In this way, the issue with reduced wavelength and the RF excitation profile inhomogeneity has been adequately addressed for most imaging applications. However, one major drawback of the 3T body coil which remains is that it is inefficient with respect to power; i.e. a lot of power is required at the coil to generate the necessary B_1^+ for imaging. Much of that power ends up deposited in the patient, which is reflected by high whole-body average specific absorption rate (wbSAR) values.⁵ High wbSAR values are a limiting factor for rapid imaging where high B_1^+ rms is necessary, because it imposes a minimum TR value to avoid heating of the patient up to potentially dangerous levels.

A possible alternative to the birdcage-type coil for body imaging is to use a local transmit/receive array (similar to the currently used receive arrays) that is placed directly onto the body. Such local transmit arrays are common for body imaging at higher field strengths (7T and above) due to the lack of a body coil in ultra-high field MR scanners.⁶⁻¹⁰ Local transmit arrays have been shown to produce sufficient B_1^+ at depth with reasonable homogeneity in the desired ROI.¹¹ While the birdcage body coil deposits energy throughout the body regardless of the imaging ROI, local transmit arrays deliver energy to a much more confined region. Therefore, a local transmit array can be used at 3T to generate lower wbSAR values and still achieve the same image quality as with the body coil.¹² There are additional benefits to be gained by exploiting the degrees of freedom using multi-transmit versus a dual channel transmit coil. Better homogeneity and higher B_1^+ values over user selected ROIs can be achieved by adjusting the relative drive phases such that the B_1^+ contributions from all channels sum constructively (RF phase shimming).¹³ Even greater benefits can be achieved by allowing the relative phase and amplitude of each channel vary over the duration of the pulse, referred to as tailored-waveform. Novel tailored-waveform multi-

transmit strategies have been developed to improve homogeneity^{14,15}, shorten pulse duration¹⁶, and provide 2D-spatial selectivity¹⁷.

The IEC 60601 standard outlines different SAR limits for volume type and local transmit coils. Volume coils such as the birdcage body coil, under the normal operation mode, are limited to wbSAR less than 2 W/kg.¹⁸ Whole-body SAR is determined from the total power absorbed by the patient divided by the patient mass. Assuming that all delivered power ends up being deposited in the patient, a conservative measurement of wbSAR can be determined by monitoring incident and reflected power entering and exiting the coil connection plane with bi-directional couplers.¹⁹ For local transmit coil arrays, the RF power is also restricted by the maximum of the local SAR averaged over 10g mass cubes (pSAR10g). Depending on the location in the body and the level of control over the well-being of the patient, this limit may vary from 10 to 40 W/kg. It is difficult to probe the SAR10g distribution in-vivo.²⁰ Thus power constraints for local transmit coils must be established using numerical FDTD simulations with anatomically realistic human body models.^{21,22} While it is clear that wbSAR can be reduced by using local transmit arrays, it is unclear whether local arrays can outperform the body coil with respect to local SAR efficiency (quantified as the ratio of B1+ to the square root of pSAR10g). It is especially noteworthy to investigate whether any benefit can be gained in practice, given that the SAR limits placed on local arrays tend to be more restrictive.

Previous work has shown that using transmit/receive (transceive) phased arrays consisting of two and four channels specifically designed for prostate imaging at 3T can significantly reduce total power requirements and also be operated under the local SAR guidelines.^{24,25} Similarly, a four channel array for 3T cardiac imaging has shown promising results compared to the volume coil.²⁶ In this work, we expand on these results and propose a new 3T prostate transceive array that takes advantage of recent advances in parallel transmit technology and looks more in-depth into the SAR analysis. Our array is constructed from eight meandering dipole antennas, based on a similar design for 7T and optimized for the lower RF frequency. We expect dipoles to be superior over loop coils for body imaging because they have a slower attenuation profile at depth, which should result in better B1+ homogeneity.

Using numerical simulations, we compare the global and local SAR efficiencies of both the body coil and the local transceive array in order to fully analyze the potential improvements in required power and local SAR safety. Since this setup allows the relative phase of these elements to be set by the user, there is potential

for a wide range of local SAR efficiencies which need to be considered. Additionally, we consider that global and local SAR efficiencies may vary with body shape/size. Finally, we acquired in-vivo images of the prostate on a number of subjects with the proposed transceive array to demonstrate the potential of this array for 3T prostate imaging in practice.

Methods

Array Design

An 8-element meandering dipole array has been designed for this study. Dipole elements were chosen because of their minimal inter-element coupling and their gradual attenuation profile at depth, resulting in more homogeneous reception and excitation patterns with less overtopping near the surface.²³ This array was initially based on the fractionated dipole array design used at 7T.

Photos of the array and the individual elements are shown in Fig. 1. Dipole antennas were constructed from printed circuit boards on top of polycarbonate covers. Each element is 32 cm long and 5 cm wide to achieve the necessary inductance for resonance without using lumped inductors and achieve adequate stability against loading variation. The polycarbonate substrate underneath the conductors provides a minimum of 20 mm spacing to the subject. The conductors are shaped as meandering structures to provide sufficient additional inductance. Alternative antenna designs where the required additional inductance was realized with lumped element inductors have also been attempted but their Q-factor was impractically high, resulting in unacceptable inter-subject variations. In addition, even when matched properly, suboptimal ‘coupling’ of the antenna to the phantom resulted in reduced signal strength at depth.²⁷ The eight elements are distributed around the body with four placed on top and four beneath the subject. The four top and four bottom elements are fastened to a flexible plastic plate to ensure proper spacing between adjacent elements.

The self-reflection of each element and the coupling to each nearest-neighboring element was measured for four different subjects while situated in the bore of the scanner in order to assess how much power is being delivered to the subject as well as determining the matching variation amongst subjects. The measurement was done using a network analyzer outside the scanner room that was connected to the array by coax cables running through the patch panel. These cables were calibrated out in advance of the measurement.

Simulations

The array was simulated using an FDTD numerical solver (Sim4Life, ZMT AG, Zurich, CH) to assess safety and make comparisons to the body coil. The array as described above was modeled in the simulation environment around the human model “Duke” from the Virtual Population, version 1²¹. The Duke model was scaled to create models with different body sizes. The model was scaled in the transverse plane to create smaller and wider subjects, but the height and muscle/fat ratio were kept approximately the same. The RF shield present in the bore of the scanner was included in the simulation model to represent the realistic scanner environment. For FDTD simulations, the computer model was converted into cubic voxels on a rectilinear grid, called “Cells”. The grid size used was approximately 6.4 MCells. This grid size corresponded to a voxel size in tissue containing regions under the coil of less than 2 mm in all dimensions. The small voxel size was necessary to resolve the intricate structure of the meandering dipole elements. A larger voxel size was used outside of the longitudinal extent of the array to speed up simulation time. A similar voxel resolution was used for the body coil simulation; however, it required more cells (11 MCells) due to the larger longitudinal extent of the coil. Each simulation was excited using a broadband “Gaussian” voltage source centered at 128 MHz with a bandwidth of 100 MHz. Convergence of each broadband simulation was checked by ensuring the power balance ratio (total dissipated/total input power) for the simulation was greater than 97%.

Both the local transceive array and body coil were simulated as multi-port simulations with each source independently active. In this way, any shim setting can be simulated by linear combinations of the individual channel field patterns. Tuning and matching of the elements in the simulation environment was neglected. Instead, the high reflection coefficients were compensated by normalizing the field distributions by the total delivered power. This could normally lead to problems related to incorrectly simulated coupling; however, both simulated and measured coupling to neighboring elements was low. Local SAR Q-matrices were calculated for both the transceive array and the body coil. For the transceive array, the local SAR Q-matrices were used to determine the worst case peak local SAR_{10g} given that all channels were active and delivering the same power with the most disadvantageous phase settings.²⁸ Worst case peak SAR_{10g} was estimated when transmitting with a total of 1 W delivered power. This value was used as a conservative limit to ensure safe scanning while monitoring incident power with directional couplers.

Advantages of an 8-ch Local Tx Array Compared to the Conventional Body Coil

Imaging

Imaging was performed on a Philips 3T multi-transmit scanner. This system has an 8-channel body coil integrated in the bore, which was actively detuned while scanning with the local transceive array. Eight RF amplifiers were used to drive the array. High power cables connected the amplifiers to the array elements through a TR-switch (MR Coils B.V. Drunen, The Netherlands). The TR-switch allows for the elements to be used also for reception, since no separate receive coil array was used.

Four subjects were scanned using the local transceive array. Subjects were placed in the scanner feet-first with the array centered on the prostate. The prostate was chosen as an imaging target to show that the array is capable of imaging targets at depth.

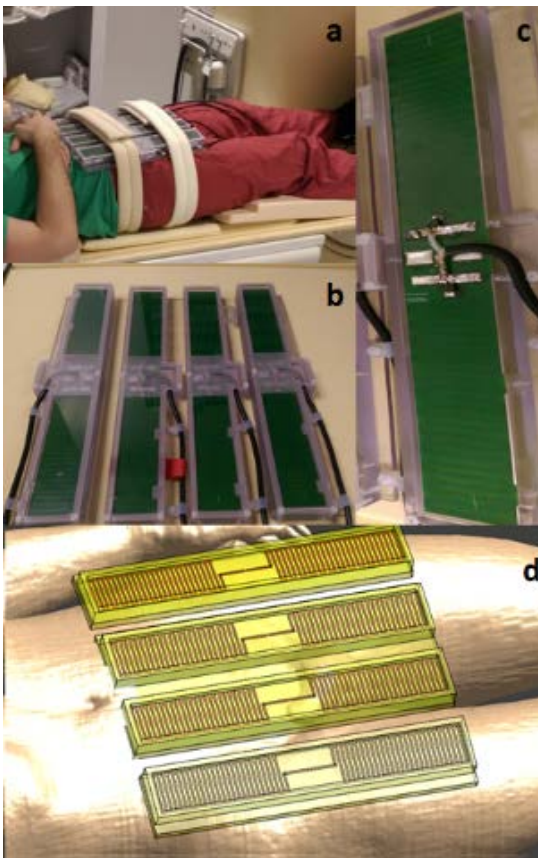


Figure 1: (a) A subject going into the scanner with the transceive array centered on the prostate. (b) Close up of the top 4 elements. (c) Close up of a single element showing the connection of the coax

Advantages of an 8-ch Local Tx Array Compared to the Conventional Body Coil

cable to the antenna. The meandering copper structure is faintly visible on top of the green PCB substrate. (d) The top four elements on a body model (Duke, ViP 3.0) in the simulation environment (Sim4Life). The meandering structure of the conductors is more easily distinguishable.

For all subjects, a dynamic low flip angle gradient echo series was acquired first to determine the relative phase maps in the body for each of the eight channels. Phase images were used to adjust the transmit phases for constructive interference in the prostate (i.e. phase shimming¹³). Actual Flip Angle Imaging²⁹ (AFI) B_1^+ maps with the applied shim setting were acquired to assess B_1^+ levels and homogeneity (Flip Angle = 65° , TR = 40/200 ms, FOV = $250 \times 422 \times 30$, resolution = $5 \times 5 \times 10$ mm³). All channels were driven with the same level of incident power. Peak incident power was set to be maximum 300 W per channel using directional couplers integrated into the transmission lines and calibrated to the coil connection plane.³⁰ Prostate images were acquired using a 2D-TSE sequence (Flip Angle = 90° , TE = 80 ms, TR = 5000 ms, TSE factor = 16, FOV = 250×422 , resolution = $1 \times 1 \times 3$ mm³). Such a long TR was used to ensure low average SAR. Assuming full power transfer (which is conservative given the measured reflection coefficients) with a duty cycle of 0.0021, then the time-averaged delivered power was 5.1 W. Considering a worst case peak SAR_{10g} of 0.50 W/kg per 1 W delivered power (determined from simulation results), this translates to 2.55 W/kg peak SAR_{10g} for this sequence; well under the 10 W/kg restriction set by the IEC. Such a conservative power limit was used due to the ethical guidelines of the institute for a coil under development.

Results

Array Design

The partial S-parameter matrices are shown in Fig. 2. Reflection coefficients varied per subject as expected. However, for every subject, the worst case reflection was better than -6 dB. While this may seem like very high reflection, -6 dB corresponds to >75% power transfer, which means that >86% of the expected B_1^+ can be achieved from even the worst performing element. Coupling to neighboring elements was low. The highest measured nearest neighbor coupling was -12 dB. After correcting for the relatively high self-reflection coefficients in the coupling measurements, the nearest neighbor coupling values are all still less than -11.4 dB.

Simulations

Simulation results confirmed the previously known concept that local transmit requires much less power than the body coil to achieve the same B_1^+ . This is

shown in Fig. 3 using the standard sized Duke body model. The body coil requires 3600 W delivered power to achieve a mean B1+ over the ROI of 12 μ T,

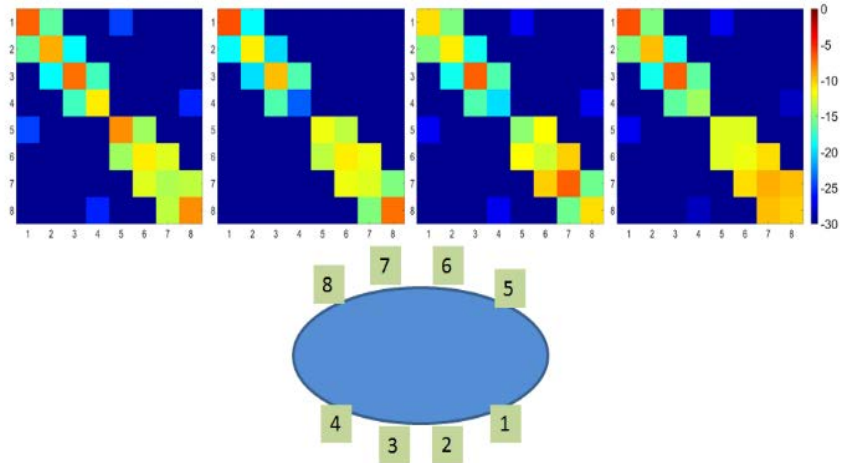


Figure 2: Magnitude (dB) S-Matrix measurements for the 4 different subjects measured with a network analyzer. Only self-reflections and nearest neighbor coupling was measured. The schematic indicates the approximate locations of the elements relative to each other and the body of the subject.

when driven with the optimum phase shim setting. The dipole array, however, can achieve the same B1+ with only 1246 W delivered power. Also shown in Fig. 3 are the maximum intensity projections of the SAR10g assuming a 1% RF duty cycle. The peak local SAR values produced by the body coil and the dipole array are very similar. The body coil generates relatively high local SAR values over a wide area of the body, including the extremities. Whereas, the local transmit array generates local SAR that is confined to the region of the body near the surface, directly under or on top of where the elements are placed.

To access some of the effects of subject variability on the SAR efficiency of the dipole array compared to the body coil, the B_1^+ distribution shimmed on the prostate and the estimated pSAR10g, normalized to 1 W delivered power, were computed for the Duke body model scaled to three different sizes (Fig. 4). As expected (and was also shown in Fig. 3), the local array produces more average B_1^+ in the prostate region for the same amount of delivered power compared to the body coil in all of the models simulated. On average, over the three body models, the local transmit array is 75% more efficient than the body coil with respect to power (i.e. global SAR efficiency). The local transmit array generates higher pSAR10g for 1 W delivered power in all three models compared to the body coil. However, the ratio of B1+ to square root pSAR10g (i.e. local SAR efficiency) is actually higher for the local transmit array compared to the body

coil. This effect is seen in all three subject models and is more pronounced as the size of the body model increases.

As part of a comprehensive local SAR analysis, we examined the effect of varying the shim setting on the resulting local SAR and B_1^+ values (Fig. 5). The average B_1^+ and $\sqrt{pSAR10g}$ are plotted for 15000 drive settings with randomly assigned phases. The birdcage coil and the 8-channel dipole array produce very different B_1^+ vs $\sqrt{pSAR10g}$ patterns due to the degree of freedom. The birdcage has only one degree of freedom, thus varying the relative drive phases traces a line in the B_1^+ vs $\sqrt{pSAR10g}$ plot. The 8-channel dipole array has seven degrees of freedom and produces a cloud like distribution of possible B_1^+ and $\sqrt{pSAR10g}$ values. One observation is that the local transmit array produces very high $pSAR10g$ when driven in the worst case (for example: .50 W/kg for the array versus .15 W/kg for the body coil per 1 W delivered power, in the medium sized body model). However, the worst case $pSAR10g$ is considerably higher than the more common $pSAR10g$ values observed for other drive settings. In normal operation, $pSAR10g$ will be much lower. For example, $pSAR10g$ for the optimal RF shimmed phase settings results in a 44% reduction in $pSAR10g$ compared to when the array is driven with the worst case settings. This is an important note because the multi-channel transmit arrays are often limited on the worst case $pSAR10g$ values, when in practice, the actual $pSAR10g$ will be much lower. It can be seen that the optimal shim setting for achieving the most B_1^+ in the prostate is also the most efficient with respect to $B_1^+/\sqrt{pSAR10g}$. The dotted line in Fig. 5a represents the optimal (best case) local SAR efficiency of the dipole array. Since all observation points from the body coil lie to the left of this dotted line, it can be concluded that the dipole array is more efficient with respect to local SAR when optimally driven (which also happens to be the most optimal with respect to B_1^+ , the same shim setting that was shown in Figs. 3 and 4).

In addition to $pSAR10g$, the B_1^+ profile homogeneity can also be evaluated over a large range of potential phase shim settings. Fig. 5b shows that the birdcage is capable of achieving the most homogenous B_1^+ profiles, determined by the coefficient of variation (standard deviation divided by the mean) over the central prostate containing region of the body (dotted box in Fig. 3). However, the optimal phase shimmed B_1^+ distribution with the 8-ch dipole array produces similar homogeneity with the added benefit of better $B_1^+/\sqrt{pSAR10g}$ performance and, of course, lower global SAR.

Advantages of an 8-ch Local Tx Array Compared to the Conventional Body Coil

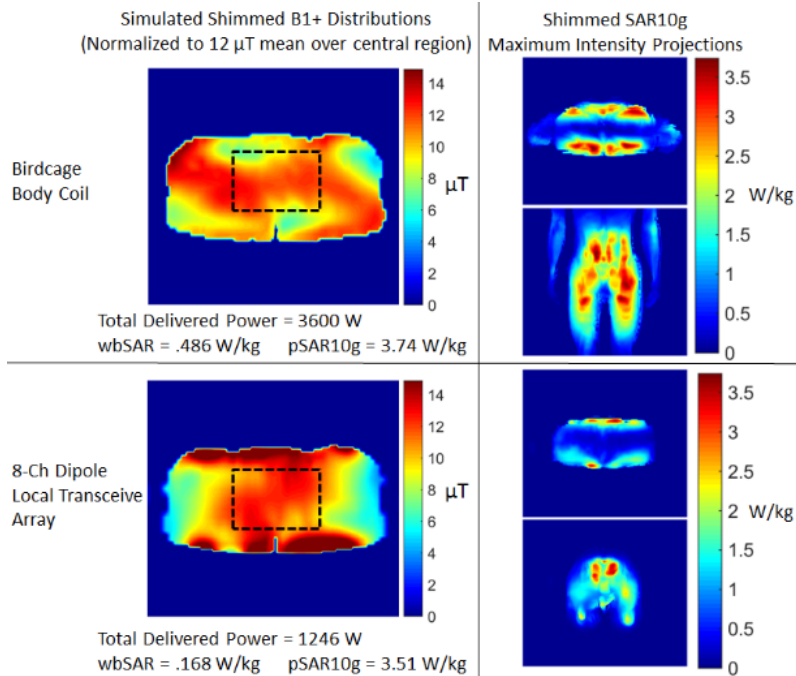


Figure 3: (Left) Simulated B₁⁺ distributions normalized to 12 μT mean B₁⁺ in the central region containing the prostate (highlighted by the dotted box) using the medium sized Duke body model. The 8-Ch transceive array requires much less peak power to achieve the same B₁⁺. wbSAR and pSAR10g values are time averaged, assuming an RF pulse 1% duty cycle. (Right) The SAR10g maps show that the body coil generates slightly higher pSAR10g for the same average B₁⁺. Additionally, the SAR10g hot spots generated by the body coil extend deeper into the body and exist over a larger region of the torso.

Imaging

B1 mapping using the 8-channel transceive array shows relatively similar excitation profiles for each of the four subjects imaged (Fig. 6), although the phases were optimized for each subject individually. Using a phase shimmied excitation pulse with equal power incident (300 W) on all eight channels, average B₁⁺ values in the prostate between 10 and 13 μT are achieved. Average B₁⁺ in the prostate is related to the size of the subject, with the highest prostate B₁⁺ achieved in the smallest subject.

These spatial B₁⁺ patterns also match reasonably well with the simulated phase shimmied B₁⁺ distribution (also shown in Fig. 6) considering inter-subject variability. The simulations, normalized to 300 W delivered power per channel, over-estimate the B₁⁺ compared to the measurements. However, this difference in simulated vs. measured efficiency can be mostly attributed to the fact that in

reality there is a significant amount of power lost due to reflections, as well as losses in the antenna components (conductors, lumped elements, substrate, and cables) which are not accounted for in simulation.

The TSE images (Fig. 7) show good quality and homogeneity over the prostate region. The prostate is clearly visible in all four subjects. Inversion bands occur at the boundaries of the body next to where the elements are located. Some subjects also show lower image intensity in the peripheral regions of the body due to lower B₁ in those areas; however the target ROI is not affected.

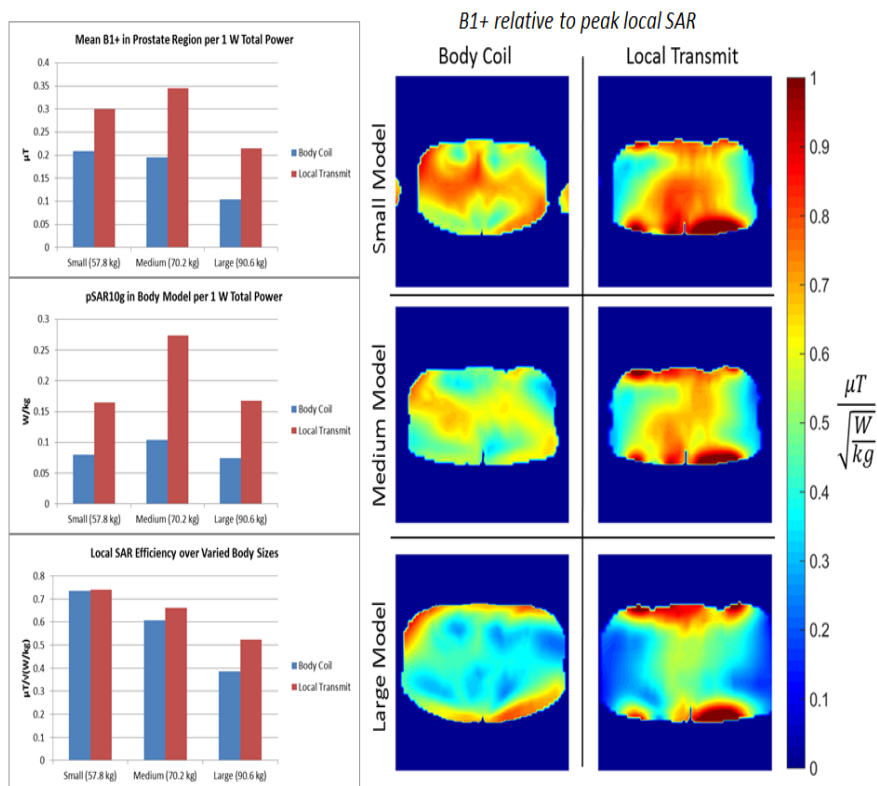


Figure 4: B₁⁺ and local SAR analysis for three differently sized body models. The bar graphs (left) show the simulated RF phase shimmed mean B₁⁺, pSAR10g and, local SAR efficiency for the different sized models. The main finding is that local SAR efficiency decreases with the size of the model. However, the decrease is less significant using the local transmit array, making it much more efficient than the body coil. This is also seen in the B₁⁺ maps normalized on peak local SAR (right). Higher B₁⁺ is achieved in the smaller model. However, the local array is still capable of producing reasonable B₁⁺ in the large model, while the body coil is not.

Advantages of an 8-ch Local Tx Array Compared to the Conventional Body Coil

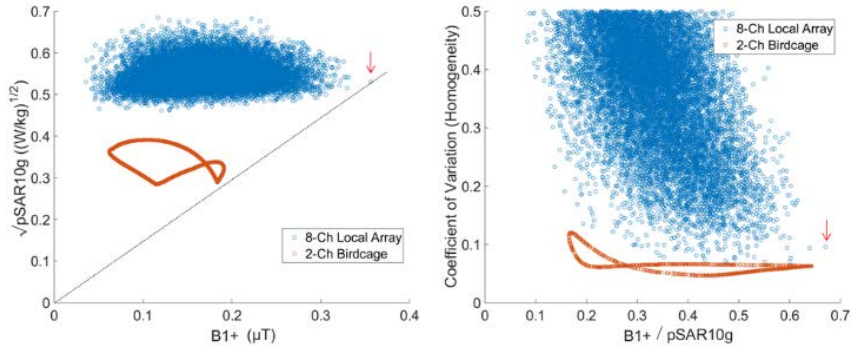


Figure 5: (Left) Simulated B_1^+ vs $\sqrt{pSAR10g}$ cloud shows the range of pSAR10g and average B_1^+ values that can be achieved by exploiting the degrees of freedom in Tx phase shimming of the 8-ch local transmit array compared to the 1 degree of freedom for the birdcage. Simulated pSAR10g and average B_1^+ in the central, prostate containing region of a human body model were calculated for over 15000 excitations with random relative tx phases and 1 W total power (.125 W per channel for the array and .5 W per channel for the birdcage). The best performing drive setting with respect to $\sqrt{pSAR10g} / B_1^+$ (slope of the dotted line) is also the optimal phase shim setting (i.e. constructive B_1^+ interference in the prostate) highlighted by the red arrow. (Right) Homogeneity, quantified by the coefficient of variation (standard deviation over mean), vs local SAR efficiency cloud shows that the birdcage produces mostly homogenous B_1^+ distributions in the prostate region while there is significantly more variance in homogeneity for the local array. However, the optimally phase shimmed B_1^+ (red arrow) produces a homogeneity comparable to the birdcage with a slightly higher local SAR efficiency.

Discussion

The goal of this study was to assess the feasibility and local SAR efficiency of a local transmit array designed for body imaging at 3T, with the intended outcome of improving transmit efficiency in comparison to the standard two-port birdcage body coil. We have shown that it is possible to obtain TSE images of the prostate using an 8-channel dipole array while remaining well below the IEC regulated pSAR10g limits. Additionally, simulations show that transmit efficiency (B_1^+ /total power) is significantly higher (+75%) for the local transmit array compared to the body coil. Although the local transmit array has its transmit elements directly on the body, the local array also performs better compared to the body coil with respect to local SAR efficiency in the phase shimmed case. Assuming the normal (medium) sized Duke model, the B_1^+ per square root of maximum local SAR is $.64 \mu T / (W/kg)^{1/2}$ in comparison to $.60 \mu T / (W/kg)^{1/2}$ for the body coil. However, given the IEC guidelines on different types of RF coils, the local array operating at the pSAR10g limit will result in lower allowed B_1^+ rms in the prostate region compared to the body coil operating at the wbSAR limit. The local transmit array can achieve an average B_1^+ rms intensity of 2.09 μT at the 10 W/kg pSAR10g limit with a 1% RF duty cycle, while the body coil is capable of 2.32 μT at the 2 W/kg wbSAR limit (a difference of -10%).

The different safety standard for local transmit compared to volume coils is clearly a limiting factor for the practical use of local transmit at 3T. However, it should be noted that volume coils can also produce high local SAR. Numerical simulations show that the pSAR10g limit that applies for local transmit coils (10 W/kg in the head/torso, 20 W/kg in extremities) is often greatly exceeded when operating at or near the wbSAR limit for a 3T body coil. Yeo et. al showed that for 4 models in different positions in a 3T birdcage body coil, the pSAR10g was 7.8 to 44.1 times higher than the wbSAR.³¹ Similarly, Murbach et. al. showed that pSAR10g can exceed 100 W/kg while operating at the first controlled mode wbSAR limit of the 3T body coil.³² The authors of that study also concluded, based on temperature simulations using Penne's bioheat equation, that such high local SAR levels do not lead to thermal tissue damage - assuming normal tissue perfusion and scan times less than 60 min. These results, combined with the extensive history of MR scanning within the body coil guidelines without adverse events, seem to imply that the pSAR10g limit for (local) multi-transmit arrays might be relaxed. In fact, there has been some recent investigation into moving towards a different set of RF safety guidelines that has a more direct relationship to tissue damage, which is thermal dose.³³ Thus, if in the future, a RF safety standard based on thermal dose is adopted and power limitations for volume type coils and local transmit arrays are defined on the same metric, it is likely that local transmit arrays can easily outperform the body coil. However, the local array is also capable of reaching far higher pSAR10g levels than the body coil. A robust quality assurance procedure with sufficient checks and balances will be required to assure that the requested phase/amplitude settings are truly reached at the ports of the elements and that the calculated pSAR10g value is truly not exceeded.

Under the current guidelines, there are still options to reduce the pSAR10g of the local transceive array. The peak local SAR can be decreased by spacing the array elements farther from the body. However, this may also lead to less B_1^+ efficiency and more inter-element coupling. Deniz et. al. have investigated optimal distance to the sample for a parallel transmit array of loop coils.³⁴ A similar investigation to maximize B_1^+ per $\sqrt{\text{pSAR10g}}$ for this array could be further investigated.

Local transmit could also be beneficial to improve the RF safety of imaging patients with implanted devices. Fig. 3 shows that the local SAR is completely confined to the area of the body between the longitudinal boundaries of the array. This signifies that a very low RF electric field is generated elsewhere in the body. This may provide safe conditions for imaging of patients with implants

that are reasonably far away from the imaging target, assuming that the electric field at the location of the implant is negligible such that it would not be influenced by the presence of a metallic structure. For example, a patient with a cardiac stent may not be at risk for implant related RF heating while using this local array centered on the prostate. In contrast, the body coil deposits energy throughout the entire torso, which could lead to an amplification of local SAR near metallic implants – regardless of the location of the imaging target.

The benefit of local transmit for very large subjects is clear from the results shown in Fig. 4. The body coil is very inefficient for large, heavily loading subjects. There are two effects that contribute to this. First, it is difficult for RF to penetrate deep into the very wide subject – however, this effect is also seen for the local transmit array. Secondly, the heavy loading subject affects the tuning of the birdcage so it may not be operating in the expected mode. The dipoles are also affected by loading, but variations in loading will only affect the amount of self-reflection and should not affect the operating mode. Note that the large patient here is not the same as an obese subject. An obese subject will have a much higher percentage of body fat which does not present a high load to the RF transmit system.

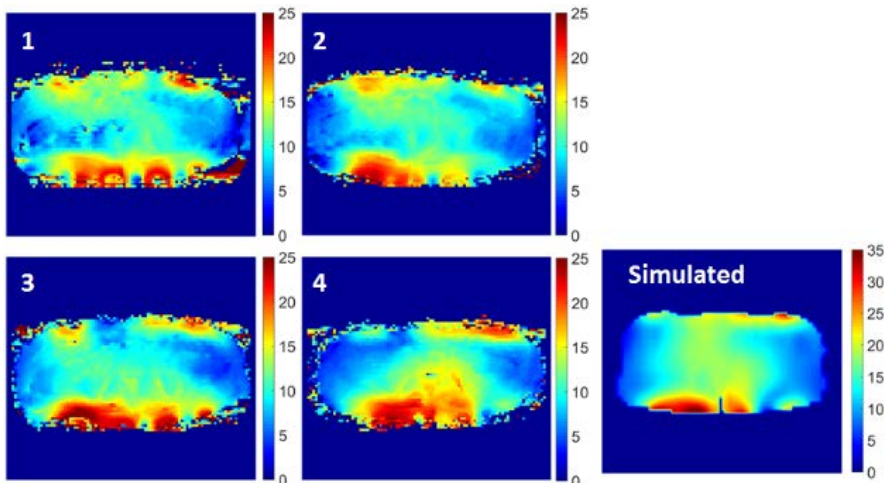


Figure 6: AFI B_1^+ maps (in μT) shimmed on the prostate measured in four subjects (1-4) and the simulated B_1^+ distribution using the Duke body model. The same incident power levels (300 W per channel) were used for the four measurements. The simulation was normalized to 300 W delivered power per channel (i.e. neglecting reflected and backwards coupled power).

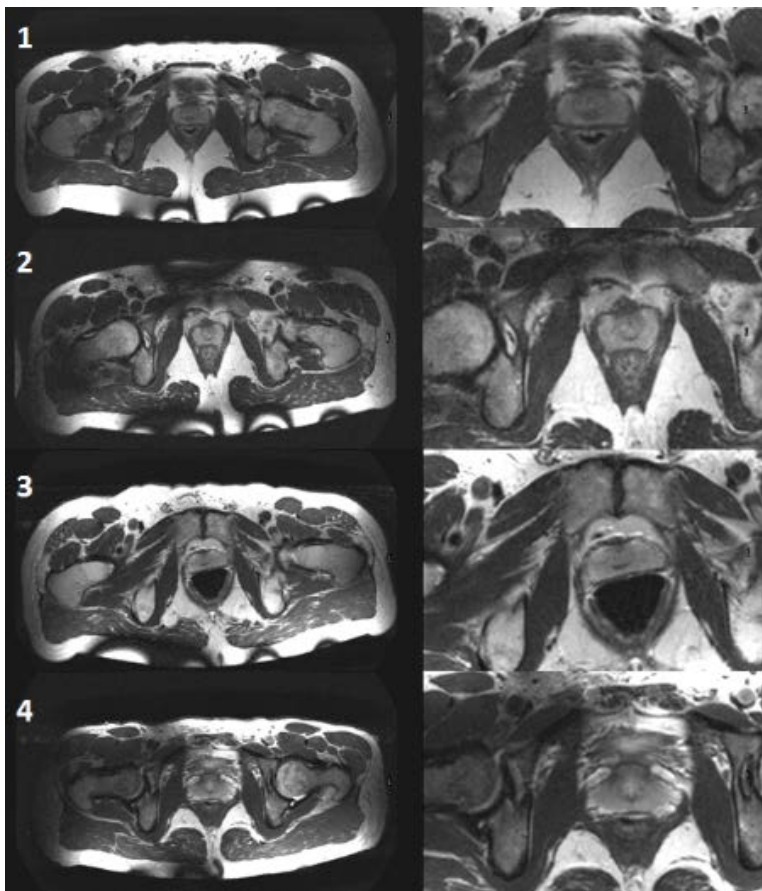


Figure 7: TSE images phase-shimmed on the prostate using the local 8-channel transceive array. Left column shows the full FOV. Right column shows the images zoomed on the prostate. Flip Angle = 90° , TE = 80 ms, TR = 5000 ms, TSE factor = 16, FOV = 250×422 , resolution = $1 \times 1 \times 3 \text{ mm}^3$.

There are other benefits from going to a local transmit array that are not fully explored in this work. Multi-transmit offers the possibility to exploit the additional degrees of freedom granted from the spatial sensitivity and independent control of each channel. For example, techniques such as SPINS¹⁴ or “spokes” pulses¹⁵ can be used to achieve homogeneity in a larger ROI compared to RF shimming. These degrees of freedom could additionally be used to reduce the pSAR_{10g}, by optimizing the transmit phase relationship that maximizes B_1^+ per $\sqrt{\text{pSAR}_{10g}}$. However, Fig. 5 shows that, for this particular array, the transmit phases determined from RF shimming also result in the optimal drive to produce the highest local SAR efficiency.

The 8-channel array used in this study was constructed to test the feasibility of local transceive array body imaging at 3T, but it is certainly not optimal yet. This study was focused solely on RF transmit, even though the elements were also used in reception for simplicity; ideally a separate receive array, with a much greater number of channels, would be used with any local transmit array for better SNR and acceleration performance. The dipole array would then have to be detuned in receive mode or the dipoles could receive with the receive array combined. The latter approach would impose strict geometrical positioning on the same axis of dipoles and loops.³⁵ The design of the array can also be further improved. Eight dipole elements is probably not the most efficient design. As noted previously, the performance can be improved by optimizing the element distance from the body. We could also investigate the shape of the elements, as well as the optimal number of transmit elements. Some work has been done demonstrating that a combination of loops and dipoles can likely achieve better B_1^+ and SAR performance.³⁶

Conclusion

An 8-channel local transceive array has been designed to investigate the feasibility of a local transmit approach for body imaging at 3T. The design consists of 8 meandering dipole antennas of 32 cm length and 20 mm spacing to the body. Both this array and a 3T birdcage body coil were simulated on 3 human models to investigate B_1^+ efficiency and local SAR performance. The local transceive array was 75% more power efficient than the body coil and showed an almost equivalent ratio of B_1^+ over $\sqrt{\text{pSAR}_{10\text{g}}}$ to that of the body coil. Given that both the local transceive array and the body coil produce approximately equal peak local SAR values per B_1^+ rms, local tissue heating is expected to be similar. However, for the transceive dipole array, global tissue heating is reduced considerably compared to the body coil due to the lower power requirements.

The 8-channel local transceive dipole array was built and tested for prostate imaging at 3T. B_1^+ maps showed that good B_1^+ intensity and homogeneity were achieved in the prostate of four different subjects. After RF phase shimming, 10-13 μT was realized using 8 x 300 W. This resulted in good quality TSE images, proving the feasibility of using local transceive arrays for prostate imaging at 3T.

References

1. Röschmann P. Radiofrequency penetration and absorption in the human body: limitations to high-field whole-body nuclear magnetic resonance imaging. *Medical physics*. 1987;14(6):922–31.
2. Ibrahim TS, Lee R, Abduljalil AM, Baertlein BA, Robitaille PM. Dielectric resonances and B(1) field inhomogeneity in UHFMRI: computational analysis and experimental findings. *Magnetic resonance imaging*. 2001;19(2):219–26.
3. Willinek WA, Gieseke J, Kukuk GM, Nelles M, König R, Morakkabati-Spitz N, Träber F, Thomas D, Kuhl CK, Schild HH. Dual-source parallel radiofrequency excitation body MR imaging compared with standard MR imaging at 3.0 T: initial clinical experience. *Radiology*. 2010;256(3):966–75.
4. Mueller A, Kouwenhoven M, Naehle CP, Gieseke J, Strach K, Willinek WA, Schild HH, Thomas D. Dual-source radiofrequency transmission with patient-adaptive local radiofrequency shimming for 3.0-T cardiac MR imaging: initial experience. *Radiology*. 2012;263(1):77–85.
5. Collins CM, Smith MB. Signal-to-noise ratio and absorbed power as functions of main magnetic field strength, and definition of “90 degrees ” RF pulse for the head in the birdcage coil. *Magnetic resonance in medicine*. 2001;45(4):684–91.
6. Kraff O, Bitz AK, Kruszona S, Orzada S, Schaefer LC, Theysohn JM, Maderwald S, Ladd ME, Quick HH. An eight-channel phased array RF coil for spine MR imaging at 7 T. *Investigative radiology*. 2009;44(11):734–40.
7. Thalhammer C, Renz W, Winter L, Hezel F, Rieger J, Pfeiffer H, Graessl A, Seifert F, Hoffmann W, von Knobelsdorff-Brenkenhoff F, et al. Two-dimensional sixteen channel transmit/receive coil array for cardiac MRI at 7.0 T: design, evaluation, and application. *Journal of magnetic resonance imaging : JMRI*. 2012;36(4):847–57.
8. Oezerdem C, Winter L, Graessl A, Paul K, Els A, Weinberger O, Rieger J, Kuehne A, Dieringer M, Hezel F, et al. 16-channel bow tie antenna transceiver array for cardiac MR at 7.0 tesla. *Magnetic resonance in medicine*. 2015 Jul 17 [accessed 2016 Mar 24].
9. Vaughan JT, Snyder CJ, DelaBarre LJ, Bolan PJ, Tian J, Bolinger L, Adriany G, Andersen P, Strupp J, Ugurbil K. Whole-body imaging at 7T: preliminary results. *Magnetic resonance in medicine*. 2009;61(1):244–8.
10. Metzger GJ, van de Moortele P-F, Akgun C, Snyder CJ, Moeller S, Strupp J, Andersen P, Shrivastava D, Vaughan T, Ugurbil K, et al. Performance of external and internal coil configurations for prostate investigations at 7 T. *Magnetic resonance in medicine*. 2010;64(6):1625–39.
11. Raaijmakers AJE, Italiaander M, Voogt IJ, Luijten PR, Hoogduin JM, Klomp DWJ, van den Berg CAT. The fractionated dipole antenna: A new antenna for body imaging at 7 Tesla. *Magnetic resonance in medicine*. 2016;75(3):1366–74.
12. Leussler C, Findekle C, Vernickel P, Nehrke K, Börmert P. Investigation of Flexible Transmit/Receive Coil Concepts on B1+ Performance at 3T. In: *Proc. Intl. Soc. Mag. Reson. Med.* 23. 2015. p. 1813.
13. Metzger GJ, Snyder C, Akgun C, Vaughan T, Ugurbil K, Van de Moortele P-F. Local B1+ shimming for prostate imaging with transceiver arrays at 7T based on subject-

Advantages of an 8-ch Local Tx Array Compared to the Conventional Body Coil

- dependent transmit phase measurements. *Magnetic resonance in medicine*. 2008;59(2):396–409.
14. Malik SJ, Keihaninejad S, Hammers A, Hajnal J V. Tailored excitation in 3D with spiral nonselective (SPINS) RF pulses. *Magnetic resonance in medicine*. 2012;67(5):1303–15.
 15. Zelinski AC, Wald LL, Setsompop K, Goyal VK, Adalsteinsson E. Sparsity-enforced slice-selective MRI RF excitation pulse design. *IEEE transactions on medical imaging*. 2008;27(9):1213–29.
 16. Katscher U, Börnert P, Leussler C, van den Brink JS. Transmit SENSE. *Magnetic resonance in medicine*. 2003;49(1):144–50.
 17. Sbrizzi A, Hoogduin H, Lagendijk JJ, Luijten P, Sleijpen GLG, van den Berg CAT. Time efficient design of multi dimensional RF pulses: application of a multi shift CGLS algorithm. *Magnetic resonance in medicine*. 2011;66(3):879–85.
 18. International T, Commission E, Iec T. IEC 60601-2-33 Safety Standard for MR Systems : Third Edition Hans Engels Philips Medical Systems , The Netherlands.
 19. Zhu Y, Alon L, Deniz CM, Brown R, Sodickson DK. System and SAR characterization in parallel RF transmission. *Magnetic resonance in medicine*. 2012;67(5):1367–78.
 20. Voigt T, Homann H, Katscher U, Doessel O. Patient-individual local SAR determination: In vivo measurements and numerical validation. *Magnetic Resonance in Medicine*. 2012;68:1117–1126.
 21. Christ A, Kainz W, Hahn EG, Honegger K, Zefferer M, Neufeld E, Rascher W, Janka R, Bautz W, Chen J, et al. The Virtual Family--development of surface-based anatomical models of two adults and two children for dosimetric simulations. *Physics in medicine and biology*. 2010;55(2):N23–38.
 22. Dimbylow PJ. Fine resolution calculations of SAR in the human body for frequencies up to 3 GHz. *Physics in medicine and biology*. 2002;47:2835–2846.
 23. Raaijmakers AJE, Luijten PR, van den Berg CAT. Dipole antennas for ultrahigh-field body imaging: a comparison with loop coils. *NMR in biomedicine*. 2015 Aug 17 [accessed 2016 Mar 24].
 24. Kim HW, Buckley DL, Peterson DM, Duensing GR, Caserta J, Fitzsimmons J, Blackband S. In Vivo Prostate Magnetic Resonance Imaging and Magnetic Resonance Spectroscopy at 3 Tesla Using a Transceive Pelvic Phased Array Coil. *Investigative Radiology*. 2003;38(7):443-51.
 25. Kaji Y, Wada A, Imaoka I, Matsuo M, Terachi T, Kobashi Y, Sugimura K, Fujii M, Maruyama K, Takizawa O. Proton two-dimensional chemical shift imaging for evaluation of prostate cancer: external surface coil vs. endorectal surface coil. *J Magn Reson Imaging* 2002;16:697–706.
 26. Weinberger O, Winter, L, Dieringer MA, Els A, Oezerdem C, Rieger J, Kuehne A, Cassara M, Pfeiffer H, Wetterling F, Niendorf T. Local Multi-Channel RF Surface Coil versus Body RF Coil Transmission for Cardiac Magnetic Resonance at 3 Tesla: Which Configuration Is Winning the Game? *PLOS One*. 2016;11(9):e0161863
 27. Haghnejad AA, Malik SJ, Padormo F, van den Berg CAT, Luijten PR, Klomp DWJ, Hajnal J V., Raaijmakers AJE. Transceive surface array of dipole antennas for multi-transmit imaging at 3T. In: *Proc. Intl. Soc. Mag. Reson. Med*. 24. 2016. p. 3174.

Advantages of an 8-ch Local Tx Array Compared to the Conventional Body Coil

28. Ipek O, Raaijmakers AJ, Lagendijk JJ, Luijten PR, van den Berg CAT. Intersubject local SAR variation for 7T prostate MR imaging with an eight-channel single-side adapted dipole antenna array. *Magnetic resonance in medicine*. 2014;71(4):1559–67.
29. Yarnykh VL. Actual flip-angle imaging in the pulsed steady state: a method for rapid three-dimensional mapping of the transmitted radiofrequency field. *Magnetic resonance in medicine*. 2007;57(1):192–200.
30. Padormo F, Beqiri A, Malik SJ, Hajnal J V. RF system calibration for global Q matrix determination. *Magnetic Resonance Imaging*. 2016;34(5):690–693.
31. Yeo DTB, Wang Z, Loew W, Vogel MW, Hancu I. Local specific absorption rate in high-pass birdcage and transverse electromagnetic body coils for multiple human body models in clinical landmark positions at 3T. *Journal of magnetic resonance imaging: JMRI*. 2011;33(5):1209–17.
32. Murbach M, Neufeld E, Cabot E, Zastrow E, Córcoles J, Kainz W, Kuster N. Virtual population-based assessment of the impact of 3 Tesla radiofrequency shimming and thermoregulation on safety and B1 + uniformity. *Magnetic resonance in medicine*. 2015 Sep 24 [accessed 2016 Feb 1]. <http://www.ncbi.nlm.nih.gov/pubmed/26400841>
33. van Rhoon GC, Samaras T, Yarmolenko PS, Dewhirst MW, Neufeld E, Kuster N. CEM43°C thermal dose thresholds: a potential guide for magnetic resonance radiofrequency exposure levels? *European Radiology*. 2013;23(8):2215–2227.
34. Deniz CM, Vaidya M V, Sodickson DK, Lattanzi R. Radiofrequency energy deposition and radiofrequency power requirements in parallel transmission with increasing distance from the coil to the sample. *Magnetic resonance in medicine*. 2016;75(1):423–32.
35. Voogt IJ, Klomp DWJ, Hoogduin H, Luttje MP, Luijten PR, Van Den Berg CAT, Raaijmakers AJE. Combined 8-channel transceiver fractionated dipole antenna array with a 16-channel loop coil receive array for body imaging at 7 Tesla. In: *Proc. Intl. Soc. Mag. Reson. Med.* 23. 2015. p. 0631.
36. Ertürk MA, Raaijmakers AJE, Adriany G, Uğurbil K, Metzger GJ. A 16-channel combined loop-dipole transceiver array for 7 Tesla body MRI. *Magnetic resonance in medicine*. 2016 Feb 17 [accessed 2016 Mar 9].

Chapter 6

Summary and Discussion

SAR safety continues to be limiting MRI experiments at all field strengths. However, it is particularly limiting at 7T because of the shift of importance from global to local SAR and the difficulties with actually being able to measure or predict local SAR accurately. Thus, local SAR predictions typically include an additional multiplication by a conservatively chosen safety tolerance factor. Parallel transmit (pTx) experiments are further limited by the unknown effects of inter-element interference. Such arrays are often limited to a small set of specific drive settings. Another common approach is to assume that the array is always producing the worst case peak local SAR, thus providing a conservative local SAR prediction that can be used for any drive setting.

Subject specific local SAR variability continues to be one of the most difficult factors in accurately determining local SAR. There have been lots of studies which look into how the peak local SAR value changes with subject size, shape, and position relative to the RF coil. In chapter 1, we assessed the effects of drastic but realistic changes in anatomy that could lead to significantly higher local SAR than we would otherwise predict using a normal, healthy body model. Given that tumors have significantly higher conductivity compared to standard body tissue, it could be expected that the local SAR would also be significantly higher inside a tumor. However, through a simulation study using computer generated models of real brain tumors and in-vivo measured conductivity values (using MR EPT¹), it was shown that the local SAR does not increase proportionally with brain tumor conductivity. In fact, the peak local SAR hotspot usually occurred outside the region of the head containing the tumor. In the worst case, we observed a 20% increase in peak 10g averaged local SAR cause by the presence of a tumor. This increase is not significant given that the chosen safety tolerance factor is typically around 100%. Thus we conclude that scanning brain tumor patients at 7T with the standard birdcage head coil does not pose an additional SAR safety risk.

The aim of Chapters 2 & 3 both was to more accurate in determining the local SAR resulting from a parallel transmit RF array. The challenge is that inter-element coupling results in unknown relative phase and amplitude changes at the end of the transmission line compared to what is requested by the scanner and delivered by the amplifiers. We proposed two possible solutions to this problem, both using directional couplers – hardware components that are already commonly integrated into parallel transmit systems.

In chapter 2, directional couplers are used to directly measure the inter-element coupling with the subject and RF array in position inside the bore. This allows

simulations to be specifically tailored to reflect the measured coupling, using a slightly adapted version of the Network Co-simulation technique for ideally tuning and matching of RF array elements as presented by Kozlov et. al.² This technique allows for the local SAR to be determined from simulations using forward power measurements for scaling. We have shown this method to be more accurate and less limiting compared to assuming worst case SAR interference. Also, this method does not require that the array be perfectly tuned and matched, which can be difficult to do in practice especially if the loading changes with subject and/or motion.

We present a different approach to the same problem in chapter 3. Here directional couplers are used to make estimations about the amplitude and relative phase of the electrical current on each of the transmit elements. This is accomplished through prior knowledge about the topology of the circuit used in the transmit element for tuning and matching. The benefit of using current to scale simulation results compared to forward power (as used in Chapter 2) is that coupling can be neglected in simulation – meaning that simulations can assume ideal decoupling among transmit elements, which is much easier to accomplish than simulating any particular coupled situation. It also means that the simulation results do not need to be re-computed when coupling changes, as would be necessary using the co-simulation technique presented in chapter 2. A similar method for current sensing already exists with using pickup probes instead of directional couplers.³ Pickup probes seem to work well when incorporated into a 3T body coil. At 7T, there is no body coil and coil arrays are typically local coils that are positioned on the patient or on the bed. The lack of a reproducible placement makes the calibration of pickup probes difficult. In addition, these calibrations are particularly sensitive to the coupling between the low power cables feeding the pickup probe signal back into the receiver and the very high power transmission line cables that (by necessity) run adjacently. Some groups have proposed using fiber optic cables for the pickup probes or wireless transmission of the pickup probe signals. However, a directional coupler solution would be preferred given that most parallel transmit systems already use directional couplers for power monitoring. The results shown in chapter 3 provide evidence that current sensing with directional couplers is possible. The limitation of this method is that some knowledge of the RF element circuit topology is required.

In chapter 4 we shift our focus from 7T to 3T in order to assess the local SAR produced by a local transmit array for 3T prostate imaging. The standard body coil at 3T is limited by global SAR by the IEC guidelines. This causes some 3T

scans to be very limited due to the fact that the body coil is inefficient with respect to power, particularly for larger subjects. A local transmit array is much more efficient with respect to power. However, local transmit (i.e. surface coils) must comply with the local SAR guidelines. We show that there is, as expected, a large benefit in terms of total power per excitation flip angle when using an 8-ch dipole array for prostate imaging compared to the standard 3T 2-ch body coil. The 8-ch dipole array also produces a lower peak local SAR for the same flip angle compared to the body coil. The problem is that the local SAR limits are more restrictive than the global SAR limits. Therefore, the body coil operating at the global SAR limit still performs slightly better than the 8-ch dipole array operating at the peak local SAR limit (10% more B1+rms in a normal sized human body model). A lot of challenges still remain related to using numerical simulations for local SAR prediction. Subject-specificity is a major problem given that numerical simulations are done with only a finite number of body models (usually only one).⁴ A solution might be to try to simulate a very large number of body models, scaled to different sizes, and placed in a wide range of positions relative to the RF array. Using virtual observation point domain reduction⁵, would make it feasible to calculate peak local SAR for hundreds of different simulated body models with a negligible computation time cost.

The difficulties of implementing these methods in practice is another technical challenge. RF array vendors may be hesitant to provide fully accurate coil models for simulation purposes. Any simulation model must additionally be validated with phantom scans before it can be trusted for safety determination. Finally, software is needed at the scanner that can monitor directional couplers and calculate local SAR based on simulated Q-matrices. Furthermore, implementing a local SAR monitoring system might place more responsibility on the MR vendor, coil supplier, or researcher responsible in case an accident ever occurred. As each party tries to shift this responsibility to others, the motivation to make less conservative RF safety predictions is inhibited.

There is a big push in the safety community to move away from SAR as the standard RF safety metric. The real risk to the patient from the RF field comes from heat generation. SAR is a relatively bad predictor of actual tissue heating, given that heating will depend on many tissue specific properties including the amount of perfusion (which is also temperature dependent). Thermal dose, which is a metric that accounts for the cumulative effect of elevated temperature over time, is a more accurate predictor of risk.⁶ The problem is that there are too many unknowns in the underlying physiological factors that regulate heat in the body to be able to accurately predict temperature over time. Future investigations into

this subject will be needed in order for better safety decisions to be made. For the current practice, it is necessary to stick with SAR as the standard safety metric. However, it is likely that these limits can be a bit more relaxed. Murbach et. al. showed that the body coil at 3T operating at the global SAR limit will actually produce local SAR levels that far exceed the local SAR limit for surface arrays.⁷ Given the long history of safe scanning at 3T, there is evidence that the local SAR limits can safely be relaxed. There should also be some motivation for relaxing the local SAR limits, given that as shown in chapter 4, the use of local transmit arrays at 3T would greatly reduce total required power relative to the body coil and would not cause any more risk to the patient.

It is also worth noting that there has never been a complication from an MR scan that was known to have been caused by (non-implant related) local SAR, aside from skin burns that have occurred related to direct contact with the metal conductors or skin-skin contact that enabled a loop current through the arms or legs. The total absence of local SAR related incidents, even although local SAR at clinical field strengths severely exceeds the recommended local SAR thresholds at 7T, is an indication that current local SAR limits might be too conservative. Many more complications in MRI have occurred from the main magnetic field when ferrous objects accidentally being brought in the scan room. However, local SAR has created problems for patients with metallic implanted devices. Parallel transmit may present new ways to scan patients with implants by allowing the electric field to be steered away from any metallic components.⁸ Thus, the methods presented in chapters 2 and 3 may be very useful for accurately predicting pTx field patterns in that application.

In summary, the operation of parallel transmit arrays is still very limited by unknown local SAR levels. In this thesis, we investigated how we can better assess local SAR to get more accurate predictions. We showed that the current safety tolerance factor is acceptable to accommodate for brain tumors, which cause a large deviation in anatomy compared to the standard body models. We also proposed methods to more accurately predict local SAR in parallel transmit experiments and even monitor local SAR in real-time using directional couplers. Hopefully, using knowledge gained from this thesis, the MR community will have a better insight into the actual local SAR levels being delivered to a subject. This should allow for faster scanning with higher flip angles compared to what was possible using the very conservative (typically worst case) local SAR approximations.

References

1. Lier A van. Electromagnetic and Thermal Aspects of Radiofrequency Field Propagation in. Universiteit Utrecht; 2012.
2. Kozlov M, Turner R. Fast MRI coil analysis based on 3-D electromagnetic and RF circuit co-simulation. *Journal of magnetic resonance* (San Diego, Calif. : 1997). 2009 [accessed 2015 Apr 17];200(1):147–52.
3. Vernickel P, Röschmann P, Findekle C, Lüdeke K-M, Leussler C, Overweg J, Katscher U, Grässlin I, Schünemann K. Eight-channel transmit/receive body MRI coil at 3T. *Magnetic Resonance in Medicine*. 2007 [accessed 2016 Aug 15];58(2):381–389.
4. Murbach M, Neufeld E, Cabot E, Zastrow E, Córcoles J, Kainz W, Kuster N. Virtual population-based assessment of the impact of 3 Tesla radiofrequency shimming and thermoregulation on safety and B1 + uniformity. *Magnetic resonance in medicine*. 2015 Sep 24 [accessed 2016 Feb 1].
5. Eichfelder G, Gebhardt M. Local specific absorption rate control for parallel transmission by virtual observation points. *Magnetic Resonance in Medicine*. 2011 [accessed 2014 Aug 25];66(5):1468–1476.
6. van Rhooen GC, Samaras T, Yarmolenko PS, Dewhirst MW, Neufeld E, Kuster N. CEM43°C thermal dose thresholds: a potential guide for magnetic resonance radiofrequency exposure levels? *European Radiology*. 2013 [accessed 2016 Mar 23];23(8):2215–2227.
7. Murbach M, Neufeld E, Kainz W, Pruessmann KP, Kuster N. Whole-body and local RF absorption in human models as a function of anatomy and position within 1.5T MR body coil. *Magnetic Resonance in Medicine*. 2014;71(2):839–845.
8. Overall WR, Pauly JM, Stang PP, Scott GC. Ensuring safety of implanted devices under MRI using reversed RF polarization. *Magnetic Resonance in Medicine*. 2010 [accessed 2016 Oct 23];64(3):823–833.

Chapter 7

Nederlandse Samenvatting

Radiofrequente (RF) energie die gedeponeerd wordt in een persoon die een 7T MRI scan ondergaat kan lokaal opwarming van weefsel veroorzaken. Het gebruik van parallelle transmissie bij een 7T MRI scan verhoogt de kans op lokale opwarming door interfererende effecten die ontstaan wanneer de kanalen simultaan RF stralen uitzenden. Het risico op RF opwarming wordt uitgedrukt door de lokale specifieke absorptie snelheid (SAR). Echter, noch kleine temperatuursveranderingen, noch SAR zijn makkelijk te meten in vivo met behulp van MRI. Daarom hangen RF veiligheidsbeslissingen voor lokale SAR af van numerieke simulaties van elektromagnetische velden welke afgeleid worden uit gedetailleerde computermodellen van de RF coil (of de parallelle transmissie opstelling) en een anatomisch accuraat model van de persoon. Verschillen tussen het simulatiemodel en een reële fysieke MRI opstelling kunnen leiden tot drastische verschillen in lokale SAR voorspellingen. Wetende dat de lokale SAR voorspelling onderhevig is aan zulke variabiliteit, wordt de veiligheid verzekerd door uit te gaan van het slechtste scenario aangaande kanaal interferentie (in het geval van parallelle transmissie) en wordt dit gemultipliseerd met een conservatieve veiligheidstolerantie factor. Dit zorgt in de praktijk vaak voor te restrictieve lokale SAR voorspellingen waardoor MRI gebruikers gedwongen worden de fliphoek of de RF pulsen in de sequentie te verminderen of de scantijd te verlengen. Het doel van deze thesis was om beter inzicht te verkrijgen in de verschillende bronnen van variabiliteit in lokale SAR voorspelling zowel als om de SAR voorspelling bij parallelle transmissie te verbeteren en de onzekerheid te verminderen.

Eén van de studies in deze thesis onderzocht de variabiliteit in lokale SAR veroorzaakt door de aanwezigheid van ernstige anatomische afwijkingen. Hiervoor keken we specifiek naar hersentumoren gebaseerd op de hypothese dat een verhoogde elektrische conductiviteit leidt tot het verhogen van lokale SAR. Onze resultaten toonden aan dat, ook al was de lokale SAR verhoogd in het gebied van de tumor, de lokale SAR waarde ter plaatse van de tumor niet hoger waren dan de maximale SAR waarde gevonden elders in het hoofd.

Twee andere studies richtten zich op het gedetailleerd simuleren van multi-kanaal interferentie langsheen parallelle transmissie elementen. Hiervoor werden “directional couplers” gebruikt die de hoeveelheid elektrische veromgen meten. We toonden aan dat de koppeling geïncorporeerd kan worden in de simulatie van multi-transmissie elementen en dat daarmee de accuraatheid van de lokale SAR voorspellingen verbeterd kan worden. Hier bovenop hebben we aangetoond dat het mogelijk is om elektrische stroom op transmissie elementen te meten met behulp van “directional couplers” lezingen. Beide methoden kunnen gebruikt

worden om lokale SAR beter te kunnen bestuderen zowel als om lokale SAR te monitoren op de scanner.

De laatste studie heeft het voordeel van multi-transmissie voor prostaat beeldvorming bestudeerd. We toonden aan dat de 3T lokale transmissie-elementen drastisch het vermogen reduceert; echter, de locale SAR limiet vertoont nog steeds restricties.

Doorheen dit werk hebben we inzicht verkregen in persoon-gerelateerde SAR berekeningen en hebben we de nauwkeurigheid van multi-transmissie SAR voorspellingen verbeterd. We hopen dat de kennis vergaard doorheen deze thesis zal leiden tot toegenomen vertrouwen in lokale SAR voorspellingen wat noodzakelijk is voor veilig scannen en om 7T MRI/parallele transmissie te accepteren als een klinisch diagnostische tool.

Chapter 8

Acknowledgments/Dankwoord

List of publications

Biography

Acknowledgements/Dankwoord

This thesis was made possible with the help of my co-promoters/advisors Hans Hoogduin, Alexander Raaijmakers, and Nico van den Berg. I would never have ended up in Utrecht if Hans and Nico didn't offer me a position as a PhD student based on a single skype conversation (plagued by a very poor connection). Hans and Nico, I am very thankful that you took a chance on me and I hope you are equally pleased with your decision to take me on as a student. Alexander, from the start of my PhD you were closely involved in my projects, even so much that you end up becoming my official supervisor. I enjoyed working with you and am very thankful for all your input/all the things you taught me.

Thanks to my paranymphs Stefano and Lennart. We all started as PhD students around the same time and have 'grown up' in the department together over the last few years. Stefano, you were always there for me. Probably because you were there everywhere I went. We shared the same office and lived in the same house for practically my entire PhD. When I moved to the U.S., I kind of expected you to follow me again. However, despite seeing each other way too much, we still had a lot of fun. Lennart, you were my first and my closest Dutch friend. Thanks for always helping me translate things, joining me to the gym, and helping me navigate music festivals.

Thanks to all the ITN fellows in Nottingham, Oxford, Nijmegen, Pisa, Magdeburg, Heidelberg, and Leipzig. It was great to reunite with you all every time we had a conference. The ITN program allowed me to travel and network way more than I otherwise would have, and was overall a very positive and beneficial experience. Special thanks to Vitaly and Nick who were in Utrecht with me. Vitaly, you always made sure I had booked my travel arrangements, had done my monthly reports on time, and was staying in the best German ski lodge. Nick, thanks for keeping me sane while Vitaly was driving me crazy doing all of the before mentioned.

Thanks to all the people at Zurich Med Tech who arranged for me to visit for 6 weeks and helped me out during my stay. My time there was critical to a lot of the work I did in my thesis. My daily coffee breaks with Pedro inspired many great ideas and helped me learn a lot of valuable programming skills.

Thanks to Ana, Saman, Marcus, Henry, and all the other friends I made while living at the Biltstraat house. It was difficult to move to another country without knowing anyone, but you all made it much easier. Many of you I stayed friends

with throughout my time in Utrecht and hope to continue to stay good friends with even though we live far away. Charlotte, Marielle and Kim, I met you three through my Biltstraat friends, thanks for all the wonderful moments we shared together.

Thanks to everyone on Q2. That hallway was such a special work environment. I can never imagine working with so many friendly, helpful people again. Thanks for the help, coffee breaks, beers in the Basket (and all around town), ImagO days, ISMRM conferences, and never ending WhatsApp messages.

Thanks mom, dad, Alison, Stephen, Rylan, and Caden. Mom and dad, at first you were surprised and sad when I told you I was thinking of moving to the Netherlands. However, when I finally decided that I was going to move, you told me that you thought it was the right choice and supported me the entire time. Your encouragement was important for me. Thanks Alison and Stephen for coming to visit me. I look forward to spending a lot of time with you all and the twins now that I live a lot closer.

Thanks Jill. You helped me so much. I honestly could not imagine having done any of this work without you. You inspired me to work hard, you consoled me when I was struggling, and you celebrated with me when I prevailed. Thanks for all the help, support, and love. Now that you moved to another continent with me, we're still there for each other and I think we really have a lot to look forward to in the future.

List of Publications:

- Restivo, M. C., van den Berg, C. A.T., van Lier, A. L.H.M.W., Polders, D. L., Raaijmakers, A. J.E., Luijten, P. R. and Hoogduin, H. (2016), Local specific absorption rate in brain tumors at 7 tesla. *Magn. Reson. Med.*, 75: 381–389. doi:10.1002/mrm.25653
- Restivo MC, Raaijmakers A, van den Berg CAT, Luijten P, Hoogduin JH. Improving Peak Local SAR Prediction in Parallel Transmit Using In-situ S-matrix Measurements. *Magn. Reson. Med.*, 2016; EPub ahead of print. doi: 10.1002/mrm.26261
- Matthew Restivo MC, Raaijmakers A, Findelee C, Mens G, Prins W, van den Berg CAT, Luijten PR, and Hoogduin JH. A Novel Approach to Real-time Local SAR Monitoring for Parallel Transmit MRI at 7T using Directional Couplers. (Submitted NMR in Biomed)
- Restivo MC, Hoogduin JH, Malik S, Beqiri A, Padormo F, Haghnejad AA, van den Berg CAT, Klomp D, Luijten PR, Hajnal J, and Raaijmakers A. Advantages of Local Transmit for Prostate Imaging at 3T using an 8-Channel Parallel Transmit Array of Meandering Dipoles Compared to the Conventional Body Coil. (Submitted NMR in Biomed)

Oral Presentations:

- Local SAR Estimation Using Lookup Tables for Two-Channel, Arbitrary RF Waveform Pulses. ISMRM MRI Safety Workshop 2014.
- Improving Peak Local SAR Prediction in Parallel Transmit Using In-situ S-matrix Measurements. ISMRM 2016 #0548 and ISMRM Benelux Chapter Meeting 2016.

Poster Presentations:

- The effect of Brain Tumors on Local SAR at 7T, ISMRM 2014; #4901
- Local SAR Estimation for Parallel RF Transmit at 7T Using Directional Couplers. ISMRM 2015; #3215

- SAR Validation on a Specially Designed Phantom with MR Thermometry and Temperature Probes Measurements. ISMRM 2015; #3219

Matthew Charles Restivo was born on March 24th 1988 in Poughkeepsie, NY. He grew up in Chapel Hill, NC and lived there until he went to study in at the University of Virginia (Charlottesville, Va) in 2006. He graduated form with a B.S. degree in Electrical Engineering in 2010 and a M.S. in Biomedical Engineering in 2012. His masters work focused on correction strategies for off-resonance blurring in spiral MRI. Afterwards he worked for a year as a contractor for the U.S. Navy, working on projects related to electromagnetic ship signitures. However, in 2013 he decided to continue working in the field of MRI and left to pursue a PhD at the University Medical Center Utrecht (Utrecht, Netherlands). Under the supervsion of J.M. Hoogduin, A.J Raaijmakers, C.A.T van Den Berg, and P.R. Luijten, Matthew worked towards advancing concepts in RF safety concerning 7T MRI. Upon completion of his PhD work, in 2016, he returned to the United States and began working as a post doctoral fellow at the National Blood, Heart, and Lung Institute of the National Institues of Health (NIH, Bethesda, MD). He works under the supervision of M.S. Hansen on projects related to fast cardiac and interventional imaging.

